Optimising Vibrojet® Performance for Offshore Installation

Using 2D Lab Tests and Particles Recognition Software

J.W. Kerkhof

TU Delft

Optimising Vibrojet® Performance for Offshore Installation

Using 2D Lab Tests and Particles Recognition Software

by

J.W. Kerkhof

Daily supervisor:	dr. ir. E. Kementzetzidis
Main supervisor:	dr. ir. J.S. Hoving
Supervisor:	prof. dr. A. Metrikine
GBM Works supervisor:	ir. C. van Verseveld
Project Duration:	May, 2023 - May 2024
Faculty:	TU Delft Faculty of Mechanical, Maritime and Materials Engineering
MSc:	Offshore & Dredging Engineering

TU Delft

Abstract

Offshore wind energy is a pivotal element in the renewable energy transition and achieving net-zero emissions by 2050. Most offshore wind turbines require the installation of a sturdy foundation called a monopile. The current method of installing monopiles offshore is known as piling, which involves driving large steel cylinders into the seabed with a hydraulic hammer. One of the major problems with this method is that it generates high levels of noise, which travel through the water and are harmful to marine life. Therefore, several European governments have introduced laws that regulate the amount of noise that may be emitted.

Multiple solutions have been developed to reduce the amount of noise that is generated but they are costly or negatively impact operational speed. Therefore, GBM Works, a startup in the offshore wind industry, is developing an innovative method for installing monopiles known as the Vibrojet®. The Vibrojet® combines both a Vibrohammer on top of the monopile with a jet at the bottom. The jet aims to fluidise the sand inside the monopile to reduce the friction on the inner shaft. This not only reduces the amount of noise emitted but also increases the installation speed of the monopile and may reduce the required pile dimensions.

This research aims to optimise the Vibrojet® performance during offshore installation by reducing shaft friction as much as possible while minimising jet flow. This approach maximises the installation speed of the monopile while reducing the capacity requirements for all parts of the Vibrojet® system. When installing a monopile while jetting, a soil skeleton forms (soil plug) in the middle of the pile while all sand particles near the inner shaft gets fluidised. The displacement of the surface of the soil plug has been assessed in this research to estimate the plug shape and optimise the performance of the Vibrojet®.

At Deltares a test setup of a soil container was constructed to imitated a 2D version of the inside of a monopile during Vibrojet® installation. The front of the container was made of see-though Perspex to enable analysis of the processes inside the pile. Inside the container holding 1,500 kg of sand, 0.3% of the particles were ultraviolet (UV) coated to enable tracking. Visual software was written to track these particles with a camera, allowing for the measurement of flow velocities and visualise the surface of the plug shape.

It was discovered that the equation for plug surface displacement overestimated the displacement observed in the laboratory tests. By analysing the results from various installation settings, discrepancies in the equation were identified. The following improvements were recommended to enhance the accuracy of the equation:

- Addition of a seepage force term to the equation
- Addition of separate term for sedimentation effect
- Factor for the return flow of particles
- Influence of the slope angle on flow erosion

A relationship was discovered indicating that the optimal flow rate for Vibrojet® installations can be determined by the total volume of sand that needs to be fluidised. A model was proposed to optimise the performance of the Vibrojet® by assessing the displacement of the plug and utilising this relationship to calculate the connection between the flow rate and the volume of the fluidised zone.

Preface

This thesis is submitted in fulfilment of the requirements for the degree of Offshore and Dredging Engineering at TU Delft. The thesis was conducted in collaboration with the TU Delft and GBM Works, a startup in the offshore industry that is developing a new method for monopile installation called the Vibrojet®. By choosing an offshore company that is working on reducing the impact of monopile installations a real contribution can be made.

I would like to express great gratitude to my supervisors, Evangelos Kementzetzidis, Jeroen Hoving, and Charlotte van Verseveld from GBM Works, for their invaluable guidance and feedback. Their insights and support allowed me to take ownership of my work and shape it into something truly my own. Additionally, I am immensely thankful to the entire GBM Works team for their contributions, resources, and the enjoyable atmosphere at the office. This project has taught me several valuable lessons, and I am grateful to have had such a supportive group of people around me.

Joost Kerkhof
Amsterdam, May 2024

The report was written with Oxford spelling.

Contents

List of Figures

List of Tables

Nomenclature

$\bar{u}$ [m/s]	Averaged flow velocity over the flow layer thickness
$\Delta\rho$ [-]	Relative difference between the particle density and the fluid density
Δn [-]	Relative change in porosity or volumetric strain
μ [Pa*s]	Dynamic viscosity
ν [m^2/s]	Kinematic viscosity
$\overline{c}$ [-]	Depth average concentration over flow layer thickness
$\overline{u}$ [m/s]	Depth average flow velocity over flow layer thickness
ϕ [°]	Internal friction angle of the soil
Φ_p [-]	Pick-up function
ρ_s [kg/m^3]	Density of particles
ρ_w [kg/m^3]	Density of fluid (water)
τ [Pa]	Shear stress within the soil plug
τ_b [N/m^2]	Bed-shear stress
$\tau_{b,cr}$ [N/ m^2]	Critical bed-shear stress
θ [-]	The Shields parameter or critical shear stress
θ_{cr} [-]	Critical Shields parameter
c [-]	Particle concentration of the mixture
D_* [-]	Dimensionless particle diameter
D_r [-]	Relative density of granular soil
D_{50} [m]	Median grain particle diameter
D_{pipe} [m]	Characteristic length of a pipe
e [-]	Current void ratio of soil
E [kg/(m^2s)]	Sediment pick-up rate perpendicular to the bed
e_{max} [-]	Maximum void ratio of soil
e_{min} [-]	Minimum void ratio of soil
f_0 [-]	Friction coefficient
g [m/s^2]	Gravitational acceleration
i [-]	Hydraulic gradient
k_0 [m/s]	Initial permeability of the sand bed
k_l [m/s]	Permeability of the loose sand bed

n_0 [-]	In-situ or initial porosity
n_l [-]	Loose volumetric porosity of the sand bed
p_p [Pa]	Pore water pressure
p_t [Pa]	Total pressure
Q_s [m^3/s]	Seepage flow rate
q_s [m/s]	Specific inflow of water into the plug
Re [-]	Reynolds number
Re_p [-]	Particle Reynolds number
S [kg/(m^{2}s)]	Sedimentation rate perpendicular to the bed
T [K]	Water temperature measured in the soil container
u [m/s]	Characteristic speed of the fluid
u_s [m/s]	Shields velocity
v_p (m/s)	Plug surface velocity
v_s [m/s]	Superficial flow velocity of water entering the bed
v_w [m/s]	Wall velocity in horizontal direction
v_{jet} [m/s]	Jet velocity
w_0 [m/s]	Unhindered particle sedimentation velocity
w_s [m/s]	Hindered particle sedimentation velocity
A[m^2]	Cross sectional areae
β [°]	Slope angle of the plug surface

1

Introduction to the Vibrojet®

1.1. Opportunities in the offshore wind market

Importance of offshore wind energy

Today, the global energy demand is still predominantly met by fossil fuels, accounting for approximately 80 percent of our consumption (iea, 2023). These high-carbon energy sources are significant contributors to not only local air and water pollution but also the broader issue of greenhouse effect. In response to this environmental challenge, sweeping initiatives such as the Paris Agreement and the European Green Deal have been enacted with the ambitious objective of achieving net-zero emissions by 2050 (EC, 2023). To realise this objective, countries must channel substantial investments into renewable energy sources.

Wind energy stands as a pivotal element in the renewable energy transition. It functions collaboratively with other renewable sources, such as solar, hydro, and geothermal energy, to create a diverse and resilient energy mix. The total installations of offshore wind power in Europe have increased from 86 MW to 25,000 MW in last 20 years, and by 2050 offshore and onshore wind power is expected to become the most important energy source and contribute to 35 percent of the world's electricity production Mehmet Bilgili and Ilhan, 2023. Furthermore, the cost required to be paid to obtain a unit amount of electrical energy (LCOE), has been reported to reduce from 0.156 USD/kWh to 0.096 USD/kWh in 10 years, which makes it a viable economic option ("Evolution of offshore wind resources in Northern Europe under climate change", 2023).

The diversification of renewable energy sources is crucial for reducing reliance on fossil fuels and ensuring a stable energy supply. This is because different sources can complement each other's variability: solar energy primarily generates power during the day, while wind energy can provide power at night and across various seasons.

Onshore wind farms often face opposition due to noise generation and visual impacts on the landscape, which are less significant for offshore windO'Sullivan, 2024. Offshore wind energy plays a pivotal role in the renewable energy transition. Over the next decade, it is projected that an additional 380 GW of offshore wind capacity will be installed Bath, 2023, as illustrated in Figure 1.1. Despite this significant expansion, the pace of development might not meet the targets set by the Paris Agreement. Key challenges hindering faster growth include permitting processes, grid infrastructure development, material sourcing, and the optimisation of installation methods.

Challenges in the monopile installation industry

To install an offshore wind turbine, a sturdy foundation is required to withstand the challenging offshore climate of wind and waves. Monopiles, which are large, hollow steel piles Vázquez et al., 2022, are the most common type of foundations, comprising about 80 percent of the support structures used for offshore wind turbines. The largest installed monopile to date has a diameter of up to 9.5 meters and a length of 110 meters, and their dimensions are expected to continue increasing Hill, 2022. The current method of installing a monopile offshore is known as piling, which involves driving large steel cylinders into the seabed. This method not only faces challenges from the harsh conditions of waves and wind, but also presents significant downsides:

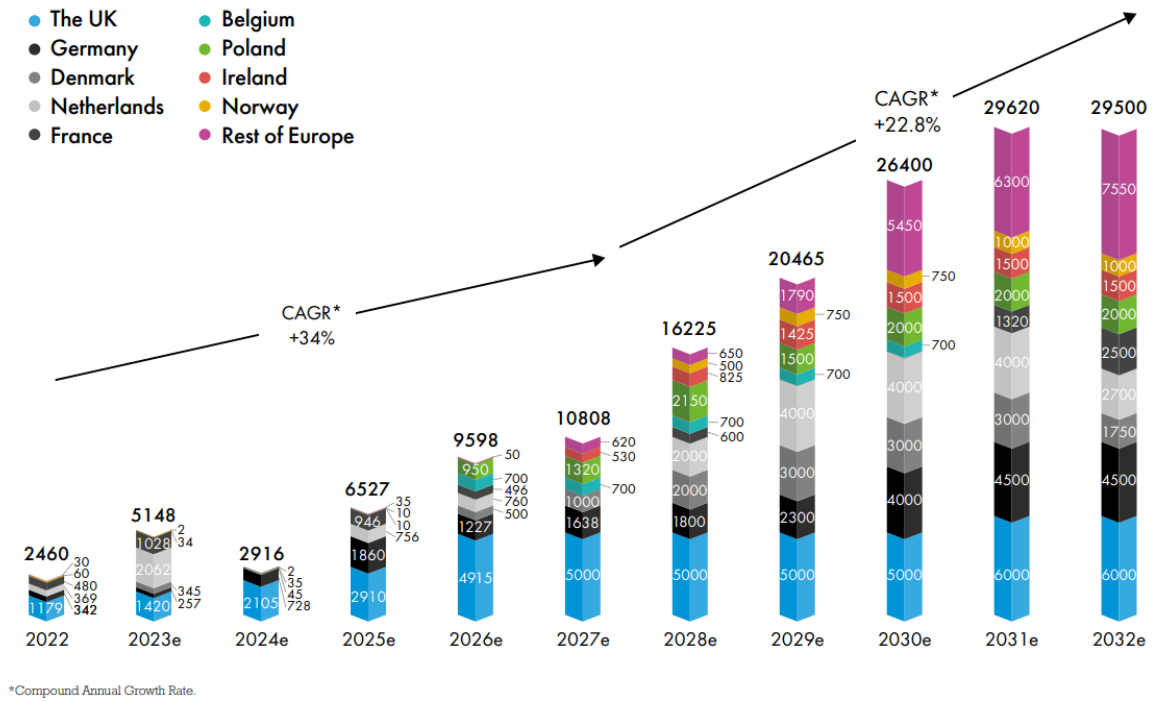

Figure 1.1: Europe offshore wind expected new installations in MW (GWEC, 2023)

1. Noise pollution during piling operations is primarily caused by the use of a hydraulic hammer that strikes the steel pile, generating high noise levels. This intense noise results from the impact of steel on steel and the subsequent vibrations along the pile, which resonate through the water and are harmful to marine life. Several European governments have introduced regulations including the dutch governments 'Kader Ecologie en Cumulatie' (KEC 4.0) which is already mentioning the 160 dB limit as a possible future regulation for the Netherlands (Noordzeeloket, 2023).
2. Fatigue Damage: The impact of the hydraulic hammer during piling operations can cause fatigue damage to the monopile. This potential damage may necessitate over-designed, heavier, and more expensive monopiles to ensure structural integrity.
3. Costs: The support structure and its installation account for approximately 20 percent of the total capital expenditure (CapEx) of offshore wind farms. This cost factor highlights the significance of optimising installation processes and technologies to reduce overall project expenses. In March 2024, Eneco, a Dutch energy company, dropped out of a tender for a 4 gigawatt (GW) wind farm spread over two locations 60 km (37 miles) off the Dutch coast. The reason for this are rising costs and the risks of delay (Reuters, 2024).

Current solutions

Current noise mitigation measures, such as the bubble curtain, involve complex setups that are both costly and time-consuming. This system functions by encircling the pile with a curtain of bubbles, which are produced by air being pumped through hoses, illustrated in Figure 1.2. The air inside these bubbles acts as an acoustic barrier, significantly reducing the transmission of sound through the water. Depending on the specific environmental conditions, two layers of bubbles may be necessary to ensure effective noise reduction. This setup not only requires additional equipment onboard but also demands a separate vessel to manage the pumps and hoses, further escalating costs. Moreover, the installation and adjustment of the bubble curtain extend the overall project timeline due to the need for precise positioning and monitoring.

Another approach to noise mitigation is the NMS-T-10000, a double-wall steel screen with an air-filled annulus between the inner and outer screens, equipped with a multi-level and multi-size bubble injection system (Blankers, 2024). While this method effectively reduces noise by creating multiple barriers to sound propagation, it is prohibitively expensive. The screen requires substantial deck space for storage and handling, and the need for additional crane operations significantly slows down the

installation process. These factors make the NMS-T-10000 a less attractive option for projects where cost and installation speed are critical considerations.

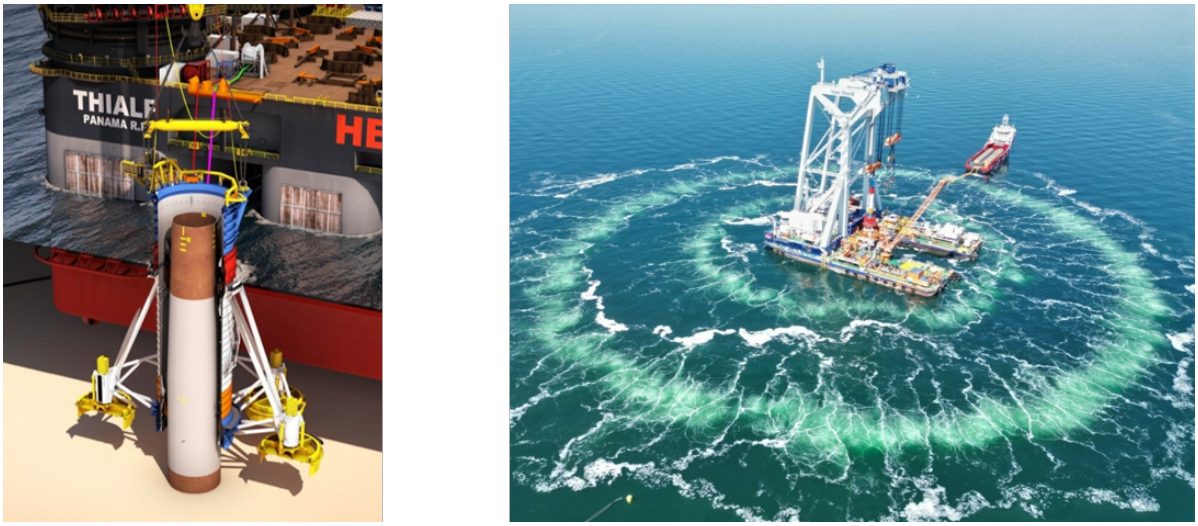

Figure 1.2: The NMS-T-10000 (left) and the bubble curtain (right), the current noise mitigation measures (Blankers, 2024)

The third approach to noise mitigation in offshore pile driving is the use of a vibratory hammer, known as the Vibrohammer, which applies a vibratory force to the top of the monopile instead of delivering large blows. It operates at a frequency of about 23 times per second (Eijkens, 2023). This method generates significantly less noise because the continuous vibratory action is less disruptive than the intermittent high-impact blows of traditional pile-driving hammers. The vibratory technique smooths the energy distribution over time, resulting in lower peak sound levels which are less likely to harm marine life. The downside of using the Vibrohammer is that it lacks certainty in achieving desired installation depths, as it may not overcome the friction resistance when the monopile penetrates deeper into the soil. Multiple factors such as soil characteristics, pile features and installation conditions have an impact on the frictional forces (Zhang et al., 2023. The left part of Figure 1.3 shows the frictional forces acting on the monopile during the current installation method.

A better way of monopile installation

To solve the problems on current installation techniques, an offshore engineering company called GBM Works, is developing a system for installing the monopiles called the Vibrojet®. The Vibrojet® technique is a combination of a Vibrohammer and a jet on the inside of the pile used to install monopiles in the sea bed. The jet is a ring with nozzles that is welded inside a monopile near the bottom while pipelines on the inside of the pile transport water to the ring. During installation offshore, the monopile experiences tip resistance, inside shaft friction and outside shaft friction. The jet fluidises the sand on the inside of the monopile reducing the inner shaft friction. The overall objective of the Vibrojet® technique is: “to enhance the ease of installation of any diameter monopile by fluidising (part of) the soil inside the pile, while not effecting the pile behaviour negatively, in order to reduce noise and increase installation depth and speed”. Figure 1.3 illustrates the contrasting installation techniques for monopiles. On the left, the traditional method using an impact hammer is depicted, which contends with significant inner shaft friction. On the right, the figure shows the innovative Vibrojet® technique, which utilises a jet ring positioned inside the monopile to mitigate the inner shaft friction effectively.

The Vibrojet® technique aims to solve several problems associated with the current installation methods. Firstly, it reduces noise levels and eliminates the need for additional noise mitigation measures, as discussed in the Vibrohammer section 1.1. It is expected that the Vibrohammer will eliminate the need to over-dimension piles because the stresses in the monopile due to the Vibrohammer would be less than those due to an impact hammer, primarily due to reduced total shaft friction. Additionally, the reduced internal friction inside the pile increases the penetration velocity of the pile, thus reducing the total installation time. This enhancement not only enables higher installation capacity but also reduces the overall costs of wind farm installation, which helps archiving the net zero goal of 2050.

Though, the Vibrojet® technique is still in developing phase and therefore studies on performance of the Vibrojet® still need to be done.

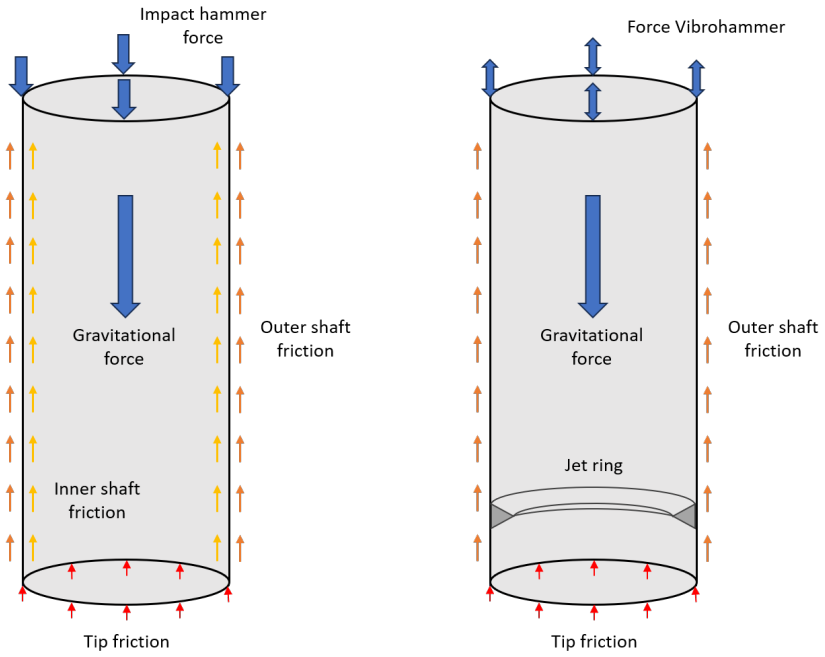

Figure 1.3: Forces acting on the monopile during piling or Vibrohammer installation

1.2. Research objective

Performance of the Vibrojet® technique

GBM Works already researched multiple aspects of the Vibrojet®, including fluidisation tests and an onshore campaign on the increase of pile penetration velocity using a 1.22 meter diameter pile equipped with Vibrojet® (GBMWorks, 2020). Now, GBM Works is collaborating with a consortium of companies to install three wind turbines using the Vibrojet® technique in 2025. To facilitate this installation, the Vibrojet® technique must undergo certification, addressing both its operational and post installation functionality. To ensure the Vibrojet® functions effectively during operations, GBM Works needs to know how it should control the flow rate of the jet.

The performance of the Vibrojet® is based on three main principles:

1. The inner shaft friction must be reduced/eliminated as much as possible.
2. The flow rate in the jet must be as low as possible.
3. There must be no impact on the lateral capacity of the monopile.

The Vibrojet® technique is used on the inside of the pile during installation to temporarily reduce/eliminate the inner shaft friction. To maximise the effectiveness of this technique, it is crucial to keep the sand adjacent to the inner shaft fluidised throughout the installation process, this is the sand-water-mixture (SW-mixture) in Figure 1.4. This ensures that particles from the surface of the soil plug are entrained in the upward flow of the jet and remain within the fluidised zone. As long as the soil plug remains stable and there are no structural failures, the non-fluidised sand will not come into contact with the inner shaft. Maintaining a low flow rate is preferable as it allows for the scaling down of all components, including the jet ring, hoses, connections, and pump. This reduction in size leads to lower operational and investment costs. Additionally, the smaller components require less deck space, which is beneficial as it could increase the number of monopiles a ship can carry in one trip. Finally, excessively high flow rates may result in water flowing around the underside and exterior of the pile, called seepage flow, impacting its lateral capacity. Even though this a vital part of the performance of the Vibrojet®, the effect of seepage on the lateral capacity of the pile is out of the scope of this research.

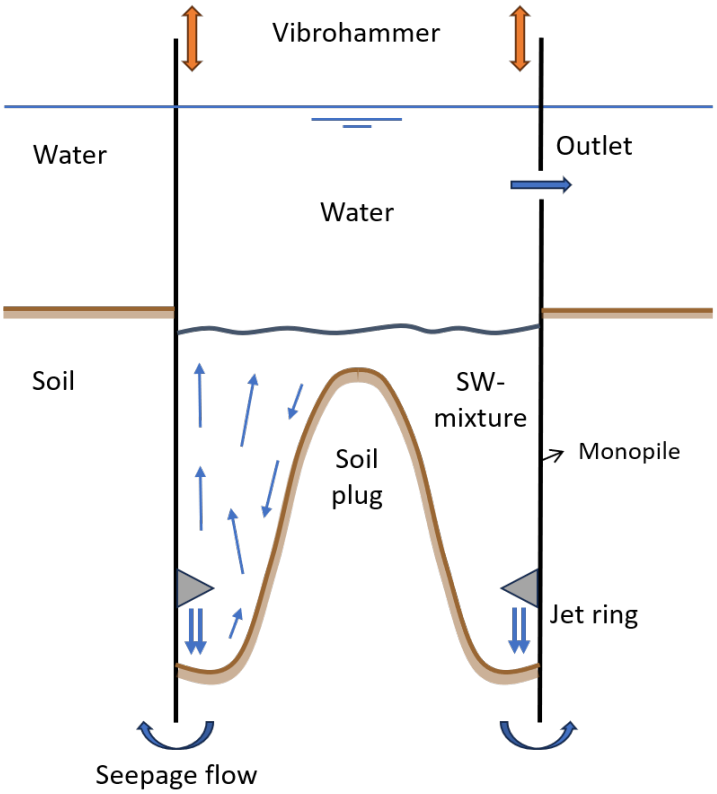

Figure 1.4: Illustration of the Vibrojet® mechanism, including the jet ring and Vibrohammer

Objective

The objective of this research is to optimise the performance of the Vibrojet® during offshore installation. The first two principles for achieving optimal performance are to reduce inner shaft friction and maintain the lowest possible flow rate. To achieve these objectives, it is necessary to link the jet flow and installation settings like monopile penetration velocity, relative density of the soil and seepage flow to the soil plug formation process and its stability within the monopile. This can be done by understanding all fundamental processes and mechanisms within the monopile that influence the formation and stability of the soil plug.

The formation of the soil plug is expected to depend on multiple parameters, including soil type, flow rate, penetration velocity of the pile, relative density of the soil, seepage flow to the outside of the pile, the size of the monopile, and the installation depth of the monopile. By understanding how these parameters influence the displacement of the soil plug during installation, this research aims to establish a relationship between the flow rate of the jet and the resulting soil plug shape. Achieving an optimal plug shape ensures that the flow rate is not excessively high but maintains plug stability, and thus effectively reduces inner shaft friction.

Scope

This study is dedicated to examining the Vibrojet® technique, a novel method for installing monopiles in offshore wind turbine constructions. It focuses on unravelling the fundamental processes behind the formation of the soil plug, which critically influence the Vibrojet® installation procedure. By doing so, the study excludes the calculation of the resulting inner shaft resistance due to fluidisation, as well as the impact on the soil surrounding the pile on lateral capacity. Additionally, the vibratory effects due to the Vibrohammer are not taken into account.

An important boundary of this study is its exclusion of the monopile rounding effects. It adheres strictly to the parameters and conditions defined within the lab setup, concentrating on the soil plug formation rather than on the jetting depth and jet erosion when the jet moves downwards; the latter will be investigated in a separate study on jet erosion by GBM Works.

Additionally, this study will not consider the variability inherent to offshore environments, such as

differing seabed compositions and the presence of materials like clay or rock. While recognising the significance of these factors, the scope is deliberately limited to ensure a focused investigation under specified conditions.

Moreover, while acknowledging the importance of environmental considerations, this study will not explore the potential impacts on marine life or the environmental advantages of the Vibrojet® technique. The intent is to concentrate solely on the technical aspects of plug shape during monopile installation, ensuring a thorough and specialised exploration within the defined scope.

1.3. Research questions

In this section the main research question was stated along the sub questions which have been stated per chapter.

Main research question:

- How to optimise the performance of the Vibrojet® during offshore installation?

Sub-questions:

State of the art theory on Vibrojet® installation

- Which equation most accurately describes plug surface displacement?
- What primary mechanisms ensure the stability of the soil plug when employing the Vibrojet®?

Imitating Vibrojet® installation with lab tests

- How can a Vibrojet® installation be imitated in a lab most effectively?
- Which tests provide the most value for identifying Vibrojet® performance?

Visualisation of lab test results: from measurements to data

- Which methods can be used to measure the needed parameters during the lab tests?
- How can the accuracy of the measurements be optimised?

Results & discussion on the Vibrojet® performance

- What is the effect of the installation settings on the formation of the soil plug?
- How can the equation be updated to accurately predict the velocity of the plug surface?

1.4. Methodology

The objective of this research is to optimise the performance of the Vibrojet® during offshore installation, by linking the jet flow rate and operational settings like monopile penetration velocity, relative density of the soil and seepage flow to the soil plug formation and stability. This can be done by understanding all fundamental processes and mechanisms within the monopile that influence the formation and stability of the soil plug.

Lab tests at Deltares research institute

To address the performance of the Vibrojet® in offshore installations, a lab testing setup was constructed at Deltares. The lab testing setup consists of a rectangular soil container with at Perplex plate in front which simulates a cut through of the monopile, as Figure 1.5 shows. The soil container is partly filled with sand to mimic the seabed environment, and a jet moves down to simulate the penetration velocity of the monopile during installation.

The overall goal of these tests is to validate three numerical models which are all interconnected. These models include a jet erosion model that predicts the behaviour of the jet stream on the sand bed during monopile installation, a flow model that assesses the movement of water and fluidised sand, and a plug surface displacement model that evaluates the displacement and shape of the plug surface between the solid and fluidised sand within the monopile. The integration of these models is designed to simulate all internal processes of a monopile during jetting, with the ultimate goal of regulating the jet flow rate. This enables the optimisation of installation settings, thereby ensuring the operational efficiency of the Vibrojet® technique and providing substantial data to support the certification process.

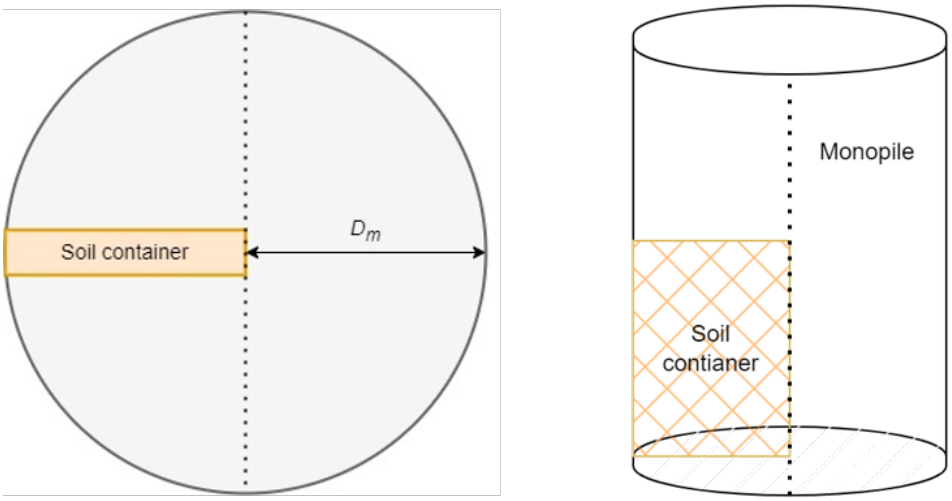

Figure 1.5: Cut through of a monopile showing the soil container inside, the left side shows the top view and right shows the front view

To analyse the displacement of the soil plug, a test matrix was developed that includes all executed tests, which varied parameters such as jet flow rate, jet penetration speed, relative density, and seepage flow. Figure 1.6 illustrates the progression of slope generation within the soil plug during the laboratory tests, detailing the measurement periods utilised in this study. Initially, the jet is positioned above the soil bed; it then descends to its lowest operational point. Once at this position, the measuring period starts and the jet maintains its location to allow the soil plug to stabilise into its final shape. It is important to mention that the failure of the plug, where multiple layers of the plug slide down as a whole, was not encountered during the lap tests.

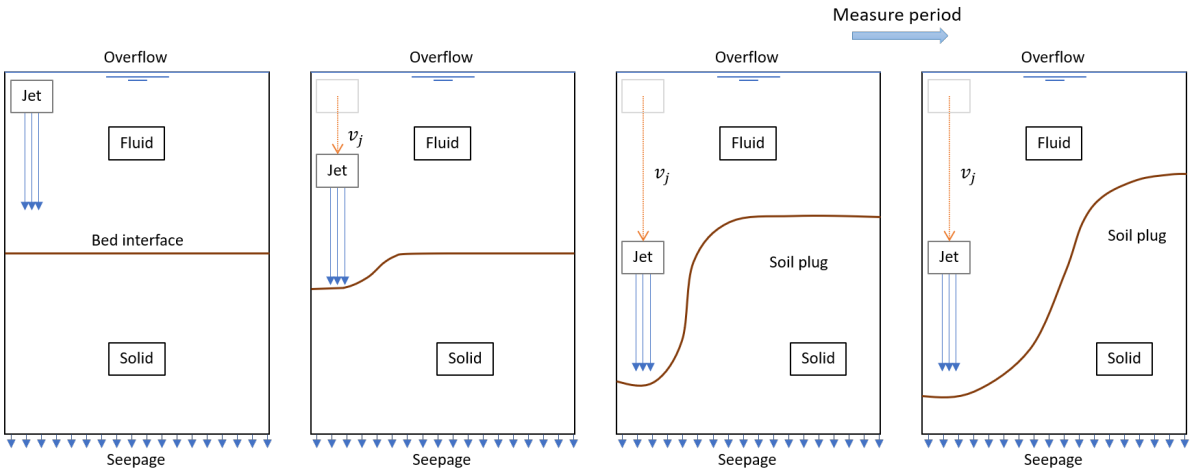

Figure 1.6: Visualisation of the slope generation during lab tests

Visual software for particle recognition

During the test phase, part of the sand particles were displaced with UV particles and the soil container was filmed with an 8k camera. This was done to allow the creation of visual software that is able to track the particles and extracted parameters like particle velocity, slope angles and plug surface displacement. These parameters were needed for the validation of the plug surface velocity model. The processes and validation of the software are mentioned in the Chapter 4.

Vibrojet® performance
In the literature review, various state-of-the-art equations for calculating the plug surface displacement are evaluated, and the most suitable one is selected for analysis in this study. The calculated plug surface velocities are compared to the tested velocities to identify the parts of the equation that need to be updated. Then the impact of installation parameters from the test matrix on the plug formation are analysed. The differences between the model and the lab results are used to explain the plug surface displacement while using the Vibrojet®. This analysis is essential for identifying the discrepancies in plug displacement equation and to discover how the Vibrojet® performance can be optimised.

1.5. Structure

The structure of this research will be as follows:

- State of the art theory on Vibrojet® installation: Reviewing existing literature on fluidisation processes, jetting in sand, and related soil mechanics to provide a theoretical framework for understanding and explaining the lab test results.
- Imitating Vibrojet® installation with lab tests: Preparing and conducting lab tests at Deltares, making design decisions and choosing which tests are most important.
- Visualisation of lab test results: from measurements to data: Gathering experimental data from Deltares by using own visual software. This software is able to detect the soil particles and can thereby automatically determine the parameters for analysis.
- Results & discussion on the Vibrojet® performance: Showcasing both the tested and calculated values of the plug surface velocity and the equation and estimating other effects not included in the model. Visualising data and pointing out key trends and findings. Utilising the results to comparing findings and discussing the implications of these results.
- Conclusion & recommendation on Vibrojet® performance: Summarising the key findings of this study, highlighting how it advances the understanding of the Vibrojet® technique, particularly in relation to the plug surface displacement and stability during monopile installation. This section will also address potential limitations of the study and suggest areas for further research.

2

State of the art theory on Vibrojet® installation

This chapter forms the foundation of this research by analysing work previously conducted in the fields of dynamics and soil mechanics, specifically focusing on their impact Vibrojet® installation dynamics and plug surface displacement and stability.

To illustrate the expected areas of interest, a sketch of the inside of the monopile during jetting has been created, as depicted in Figure 2.1. This image provides a cross-section of the monopile, with the shaft on the left and a dotted line marking the middle of the monopile. As the monopile penetrates the soil, the jet fluidises the sand above it, creating a SW-mixture near the shaft, also called the trench. This happens while the soil near the axis of the monopile remains undisturbed, forming the soil plug. The blue, green, and orange arrows indicate the expected flow directions of the fluids, corresponding respectively to the SW-mixture flow, the water inflow, and the gravity flow.

Along the whole plug surface several erosion and sedimentation processes take place. Erosion processes are grain-by-grain erosion at small scale and wedge erosion. This erosion comes in two forms, called erosion due to flow and breaching. During erosion due to flow the particles get picked up due to the shear stresses induced by the flow on the particles. During breaching the slope angle of the plug is higher than the angle of repose of the soil itself, causing the slope surface to be unstable and particles falling down. In a perfectly homogeneous soil, the grain-by-grain and wedge erosion would occur everywhere around the pile wall and would thus result in an axis-symmetric soil plug. However, due to in-homogeneity of the soil this will slightly vary from place to place.

The red line, whose shape is illustrative and may vary in size and position, represents the part of the plug that could slide down when the slope is high and/or steep enough causing a slope failure. A large sand mass is then sliding over a sliding surface, collapsing into the fluidised zone and against the pile wall. This may hinder the fluidisation process and cause inner wall friction to increase.

To ensure a structured approach, three sub-questions have been formulated:

1. Which equation most accurately describes plug surface displacement?
2. What primary mechanisms ensure the stability of the soil plug when employing the Vibrojet®?

The chapter is divided into four sections to thoroughly address these questions:

- Background theory on bed and sediment displacement (Section 2.1). The Background Theory section provides foundational information on the main principles of fluid dynamics and soil mechanics impacting underwater surface erosion and wall velocity, ultimately affecting plug surface displacement. It also considers previous work by GBM Works.
- Effects on the plug formation process (Section 2.2). The State of the Art section reviews the most recent studies on the erosion of soil surfaces in different environments. Also, it proposes the equation that will be used to determine the plug surface displacement and evaluates its potential shortcomings, in Figure 2.1 this would be the gravity flow part.

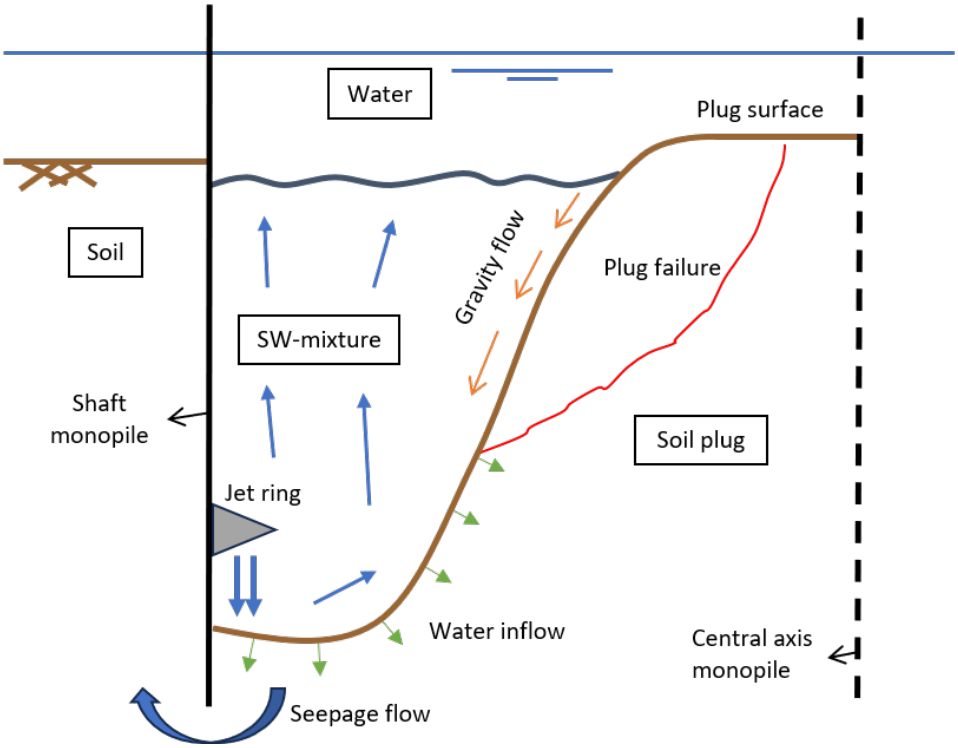

Figure 2.1: Mechanisms inside the cut through monopile while jetting

- Shear strength inside the soil plug (Section 2.3). This section explores the shear strength properties within the soil plug, which are critical for maintaining the stability of the plug during the installation process. Figure 2.1 shows an example of what could happen during shear strength plug failure.
- Literature Gaps and limitations (Section 2.4). This section examines the limitations present in the existing literature, aiming to identify areas that require further research to deepen the understanding of soil plug formation and stability. Additionally, it summarises the assumptions underlying the current theoretical and experimental frameworks.

2.1. Background theory on bed and sediment displacement

This section provides fundamental theory for understanding the dynamics within the monopile by delving into the interaction of particles in fluid, viscosity, turbulence, particle Reynolds number and the mechanics of sedimentation. It then progresses to cover essential principles such as the relative density and permeability of a sand bed, both of which are crucial parameters for evaluating the plug surface displacement. Following this, it explains the background theory of soil erosion caused by fluid flow, which is governed by the Shields parameter and leads to the calculation of the pick-up function. This theoretical framework is needed for understanding how fluid movement affects soil stability and erosion, ultimately influencing the behaviour of the plug surface under the expected conditions.

Bed interface

The bed interface is the border between fluid state and the solid state of a sand bed. The speed at which a bed interface of sand moves up and down is dependent on the bed erosion rate (E) (or sediment pick-up rate) and sedimentation rate (S) which are the processes of particles wearing away from a surface and settling out of a fluid flow. The downward movement of the interface is called the erosion velocity (v_e) and the upward movement is the sedimentation velocity (v_{sed}). The general equation for the velocities is given by Bisschop, 2018 (2.1). All parameters are visualised in Figure 2.2.

$$v_{\text{e}} = \frac{E - S}{\rho_s \left(1 - n_0 - c\right)} \qquad v_{\text{sed}} = \frac{S - E}{\rho_s \left(1 - n_0 - c\right)} \tag{2.1}$$

- E [kg/(m^{2}s)] - the sediment pick-up rate in mass per unit area perpendicular to the bed
- S [kg/(m^{2}s)] - the sedimentation rate in mass per unit area perpendicular to the bed
- ρ_s [kg/m^3] - the density of soil particles
- n_0 [-] - the in-situ or initial porosity
- c [-] - the concentration

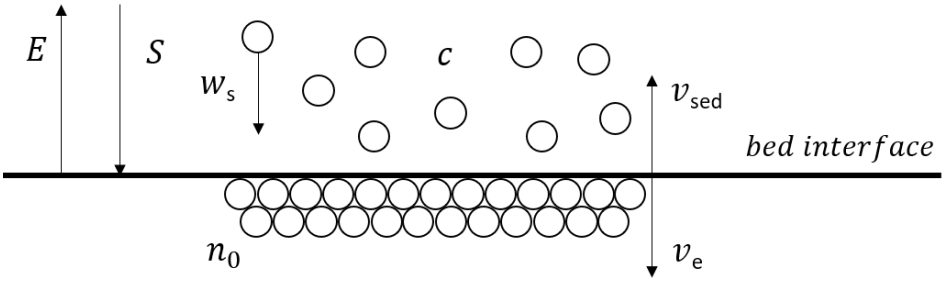

Figure 2.2: Erosion and sedimentation directions and critical parameters at a bed interface

When the bed interface is tilted by an angle of β degrees, the inclination impacts the sedimentation rate. Multiplying the original sedimentation rate equation by the cosine of the angle β accounts for the effect of gravity on the sedimentation process at an angle, which is less direct than in the vertical orientation. The revised equation is given in equation 2.2.

$$S = \rho_s w_s c \cos\beta \tag{2.2}$$

- w_s [m/s] - hindered sedimentation velocity

Viscosity

Viscosity is a measure of a fluid's resistance to flow and deformation by shear or tensile stress. The International Association for the Properties of Water and Steam (IAPWS) in 2008 provided an empirical equation that relates the viscosity of a fluid to its temperature. The equation given by IAPWS allows the calculation of dynamic viscosity (μ) using temperature-dependent empirical constants (A, B, C) and the temperature (T) itself. These constants are determined through experiments and are specific to water. The use of this equation enables the prediction of how water viscosity changes with temperature in the soil container, which has been used to calculate the significance of the viscosity change during the testing sequence.

$$\mu = K \times 10^{L/(T-M)} \tag{2.3}$$

- μ [Pa*s] - the dynamic viscosity
- K, L, M - the empirical constants ($2.424 * 10^{-}5, 247.8K, 140K$)
- T [K] - the water temperature measured in the soil container

Turbulence

The different flow regimes play a pivotal role in fluid dynamics and in predicting the way particles behave in a flow. Laminar flow is characterised by smooth, parallel layers of fluid moving in a consistent direction without cross currents or eddies. It's typically observed at low velocities and is governed by viscous forces, ensuring orderly and streamlined fluid motion. Turbulence is characterised by flow velocities that vary in every direction. This turbulence manifests distinct flow patterns that impact both the flow velocity and the normal stress applied by the flow to a particle or a bed interface. The transition regime between laminar, transition and turbulent regime is relatively: <10, 10-20,000 and >20,000. Figure 2.3 visualises the different flow regimes.

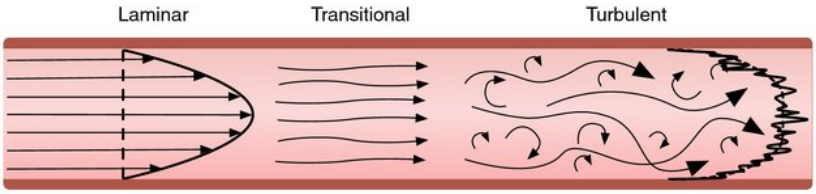

Figure 2.3: Flow regime illustration of laminar, transitional and turbulent flow (McGurk et al., 2020)

To predict the onset of turbulence in fluid flows in a tube the dimensionless Reynolds number Re was used. It is defined as the ratio of inertial forces to viscous forces and describes the relative importance of these two types of forces for given flow conditions. When the Reynolds number exceeds a certain value, the flow transitions from laminar to the transition regime where the flow can be described as laminar with intermittent bursts of turbulence. This critical value depends on the specific geometry and conditions of the flow, shown in Equation 2.4 (Rott, 1990).

$$Re = \frac{\rho_w u D}{\mu} = \frac{\nu D_{pipe}}{v} \tag{2.4}$$

- ρ_w [kg/m^3] - the density of the fluid (water)
- u [m/s] - the characteristic speed of the fluid
- D_{pipe} [m] - the characteristic length of a pipe
- ν [m^2/s] - the kinematic viscosity

Particle Reynolds number

In the context of particles in a fluid, the particle Reynolds number Re_p [-] becomes particularly relevant, as it captures the flow dynamics around individual particles and helps predict their behaviour in various flow regimes. Contrary to the traditional definition of the Reynolds number, which uses the fluid velocity scale, the particle Reynolds number is tailored specifically for particles suspended in a fluid (Brownlie, 1981). Is is also used as a function of the drag coefficient C_d. Equation 2.5 shows the calculation of the particle Reynolds number. This particle Reynolds number is based for only one particle and does not take into account the concentration of the fluid, it is not dependent on the concentration in terms of its definition. It is expected that at higher concentrations, the interactions of particles can become significant since nearby particles would influence the flow conditions of other particles.

$$Re_p = \frac{D_{50}\sqrt{\Delta \rho g D_{50}}}{v} \tag{2.5}$$

- $\Delta\rho = (\rho_s - \rho_w)/\rho_w$ [-] - the relative difference between the particle density and the fluid density
- g [m/s^2] - the gravitational acceleration
- D_{50} [m] - the median grain particle diameter

Sedimentation velocity

Now the characteristics of the bed interface, viscosity and turbulence have been covered, the sedimentation velocity can be computed. The sedimentation velocity of a symmetric single particle in horizontal laminar flow is based on three forces: the drag and buoyant forces working up and the gravitational forces working down.

In turbulent flow conditions, the motion of particles is chaotic, leading to frequent collisions and interactions. Furthermore, the irregular flow causes variations in drag on the particle which affects the settling velocity (w_0) . The calculation of the settling velocity for spherical particles in laminar flow is relatively straightforward, as shown in equation 2.6.

$$w_0 = \sqrt{\frac{\Delta \rho g D_{50}}{18 v}} \tag{2.6}$$

The following equation from Ferguson and Church, 2004 is able to calculate the unhindered settling velocity over the whole range of particle Reynolds number and for different particle shapes (roundness value). Where the value for $C_1 = 18$ and $C_2 = 1$ for natural sands and $C_2 = 0.44$ for spheres 2.7.

$$w_0 = \frac{\Delta \rho g D_{50}^2}{C_1 \nu + \sqrt{0.75 C_2 \Delta \rho g D_{50}^3}} \tag{2.7}$$

The sedimentation velocity can also be hindered by a large number of particles present in the set space. This high concentration will cause an upside flow through the mixture increasing the drag force acting on the particles. A higher the concentration in the mixture will cause a higher drag force following Richardson and Zaki, 1954 equation, resulting in the following hindered sedimentation velocity w_s , see equation 2.8.

$$w_s = w_0 (1 - c)^n \tag{2.8}$$

The exponent n is determined by the particle's Reynolds number, given in equation 2.5. It ranges from 2.4 for coarse particles to 4.65 for fine particles. The most effective way to calculate n is the method proposed by Rowe, 1987 shown in equation 2.9. Figure 2.4 shows the relative settling velocity as a function of the concentration.

$$n = \frac{4.7 + 0.41 Re_p^{0.75}}{1 + 0.175 Re_p^{0.75}} \tag{2.9}$$

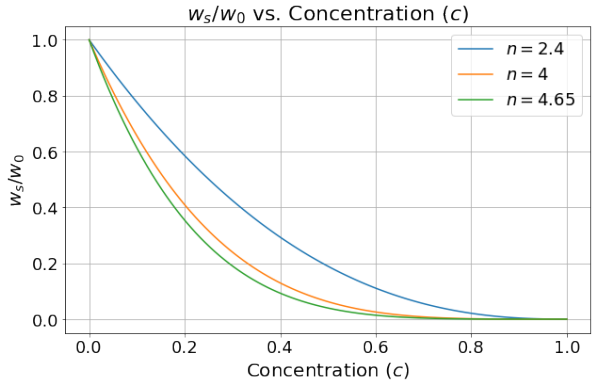

Figure 2.4: Relative settling velocity with respect to hindered as a function of concentration

Relative density

The relative density (or density index) D_r of granular soil, such as sand, is related to its void ratio through empirical relationships that compare the in-situ void ratio with the void ratios at the loosest and densest states. The relative density is a measure of the degree of compaction of non-cohesive soil. In other words, the difference in void ration between its loosest state and existing natural state to the difference between its void ratio in the loosest and densest states (Equation 2.10). The relative density is used to calculate the height of the soil in the soil container during lab tests. A vibratory hammer is used before the tests to compact the soil and get the right relative density.

$$D_r = \frac{e_{max} - e}{e_{max} - e_{min}} \tag{2.10}$$

- e [-] - the current void ratio of soil
- e_{max} [-] - the maximum void ratio of soil (the loosest state)
- e_{min} [-] - the minimum void ratio of soil (the densest state)

The calculation of the relative density can be done from the minimum and maximum dry air density of the sand. In the appendix are the values that have been used for this study, see Figure A.9. Then the initial and loose sand (maximum) porosity can be calculated using Equation 2.11.

$$n = 1 - \frac{\rho_{d,min/max}}{\rho_s} \tag{2.11}$$

Permeability

Permeability is a characteristic of materials that reflects their capacity to allow fluids or gases to pass through them. In the context of a soil container, as discussed in section 2.2, this property is crucial for two key components:

1. Sand Permeability: The permeability of the sand within the container significantly influences the rate of soil pick-up. The initial permeability of the sand, denoted as k_0, is calculated based on the Van Rhee and Bezuijen (1998) equation. This equation incorporates factors such as gravitational acceleration, particle size, fluid viscosity, and soil porosity.
2. Geotextile Permeability: The geotextile layers located at the top and bottom of the container play a dual role. They allow water to filter through while preventing the passage of sand particles, thus ensuring the integrity and functionality of the container's filtration system.

Additionally, permeability changes in response to alterations in soil porosity. For a loose sand bed, where the porosity is denoted by k_l, adjusts according to the changes in porosity. This relationship underscores the dynamic nature of permeability in response to environmental and material conditions within the soil container.

$$k_o = \frac{gD_{15}}{160v} \frac{n_0^3}{(1-n_0)^2} \tag{2.12}$$

Shields parameter

The subsequent sections of the background theory delve further into soil erosion, focusing on the dynamics of fluid forces acting upon soil particles. It examines how these forces initiate particle movement, causing them to get integrated into the flow.

The Shields parameter θ , part of the Shields diagram, was constructed by Albert Shields in 1936 (Shields, 1936). It is a graphical representation which shows the prediction of particle movement by fluid flow.

It relates the Shields parameter, also the dimensionless shear stress, to the particle Reynolds number. When the instantaneous fluid force on a particle exceeds the instantaneous resisting force associated with the weight of the submerged particle and the friction coefficient, particle movement will result. Shields calculation for the Shields parameter is given by Equation 2.13.

$$\theta = \frac{\tau_b}{(\rho_s - \rho_w) g D_{50}} \tag{2.13}$$

- τ_b [N/m^2] - the bed-shear stress

Another way to calculate the Shields parameter is using the averaged flow velocity over the flow layer thickness above the bed $\bar{u}$ [m/s] (van Rhee, 2010). The equation is dependent on the Darcy-Weisbach friction coefficient which describes the roughness height and the flow depth. This coefficient normally gets calculated for river beds or pipe flow and no studies for steep angles could be found Brownlie, 1983. Therefore the estimated value of f_0 = 0.01 was used in Mastbergen and Berg, 2003 will be used.

$$\theta = \frac{f_0}{8}(1 + \Delta\rho\bar{c}) \frac{\bar{u}^2}{\Delta\rho g D} \tag{2.14}$$

- $\overline{u}$ [m/s] - the depth average flow velocity over flow layer thickness
- f_0 [-] - the friction coefficient
- $\bar{c}$ [-] - the depth average concentration over flow layer thickness

It is important to understand that the Shields diagram is limited under three conditions: the sediments sizes are uniformly distributed, the bed slope is horizontal or near horizontal and the flow is unidirectional, which means that the flow has one direction without back-flow (Shields, 1936).

Critical Shields parameter

The critical Shields parameter, often denoted as θ_{cr} , is a threshold value of the Shields parameter. When the actual Shields parameter exceeds this critical value, sediment particles are likely to be initiated into motion, leading to erosion or transport. The critical Shields parameter is primarily a function of the Reynolds number and varies with sediment properties and flow conditions. It serves as a boundary delineating the transition from stationary to mobile sediment phases. There are many ways to calculate the critical Shields parameter, one of them is shown in Equation 2.15 (Brownlie, 1981). The given equation is applicable exclusively to horizontal slopes and particle by particle erosion. Alternative formulations for the critical Shields parameter will be discussed in Section 2.2.

$$\theta_{cr} = 0.22R_p^{-0.6} + 0.06 \exp\left(-17.77R_p^{-0.6}\right) \tag{2.15}$$

The equation from Brownlie, 1981 is restricted by the following conditions:

- Sand only ($0.062 < D_{50} < 2.0$)
- Minimum concentration of 10 percent
- Minimum Relative roughness ($R/D_{50} > 100$)
- Width to depth ratio ($w/d > 4$) - lab setup does not comply with the reduced sidewall effects

Equation 2.16 is associated with Shields criterion and is relatable to the equation for the Shields parameter (2.13). The equation was formulated based on the equilibrium between the drag/lift forces exerted by the fluid and the opposing forces proportional to the submerged weight.

$$\theta_{cr} = \frac{\tau_{b,cr}}{(\rho_s - \rho_w)gD} \tag{2.16}$$

- $\tau_{b,cr}$ = [N/ m^2] - the critical bed-shear stress

Pick-up function

Underwater sediment erosion, or sediment transport, is driven by the flow of water and is a critical process in soil mechanics. To calculate the erosion velocity the pick-up function is used. The pick-up function (Φ_p) is a non-dimensional parameter which relates the fundamental principles of fluid dynamics and soil mechanics, how fluid flow influences the detachment and entertainment of soil particles. I.e. it allows the calculation of the sediment pick-up (erosion rate) relative to the Shields parameter. Several pick-up functions can be found in literature, and mostly it is an empirical function derived from experimental results. The Equation 2.17 for the sediment pick-up was firstly mentioned by Einstein, 1950.

$$\Phi_p = \frac{E}{\rho_s\sqrt{\Delta\rho g D_{50}}} \tag{2.17}$$

The right hand side of the equation, based on Shields parameter, is empirically determined in several studies (Winterwerp et al., 1992, Mastbergen and Berg, 2003, and van Rhee, 2010). It is essential to understand that there are multiple processes which influence the erosion velocity. Every pick-up function includes one or more of these processes as precisely as possible but different situations alter the resulting erosion. Therefore, there is no single pick-up function which includes all scenarios of sediment pick-up. To accurately represent surface erosion on the interior of a pile during the application of the Vibrojet® technique, a range of pick-up functions will be assessed. These functions, which model the rate of sediment erosion, will be evaluated in detail to identify the one that most precisely captures the erosion dynamics in this specific context. This process will ensure a more accurate and reliable understanding of the sediment transport phenomena occurring within the pile during the Vibrojet® operation.

2.1.1. Previous research GBM Works

The inner shaft friction is reduced through the fluidization of sand within the shaft. Fluidization occurs when the upward flow, combined with buoyancy force, exceeds the weight of the particles, causing them to separate and move, thereby expanding the bed. This transition from a solid to a fluid state is termed fluidization. As a result of this state change, the effective stress between the particles is reduced to zero (Niven and Khalili, 1998).

Before this study, GBM Works conducted several investigations on the Vibrojet® (GBMWorks, 2020), including the SIMPLE I test setup featuring three models, the largest being a 4-meter-high pile with a 60 cm diameter, shown in Figure 2.5. This study aimed to assess the impact of grain size, porosity, and flow rate on penetration velocity and the required flow for fluidisation per grain size.

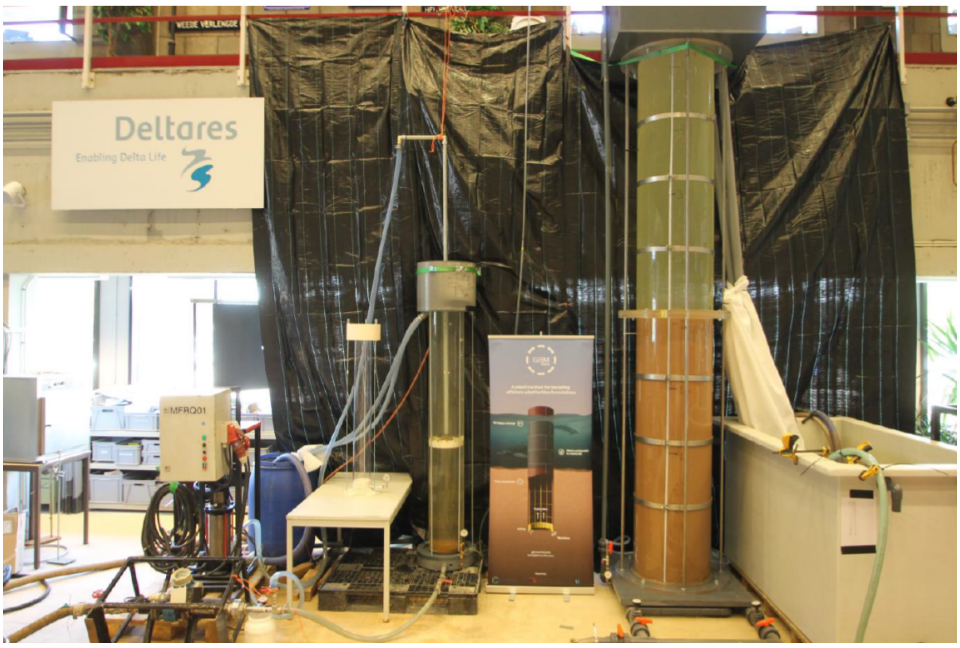

Figure 2.5: SIMPLE I laboratory test setup at the Deltares research institute

The fluidisation tests show that only a low amount of water displacement in an upper trajectory is needed for the fluidisation of sand. The bigger the grain size, the larger the flow needed for this fluidisation. This indicates that a flow through a fluidised soil will arrange the sand to larger grains sizes at the bottom and to smaller grain sizes at the top of the column. The difference in fluidisation on different scales is not yet fully calculated, although it is clear that a larger system or soil volume takes longer to settle on a specific porosity, when a flow is introduced. Figure 2.6 illustrates fluidisation tests for sand particles with a $D50$ of 250 micrometers, closely aligning with the grain size selected for this study. For grain sizes from 150 to 500 microns the porosity was 50 to 70 percent and thus the volumetric concentration of sand in the mixture was 30 to 50 percent.

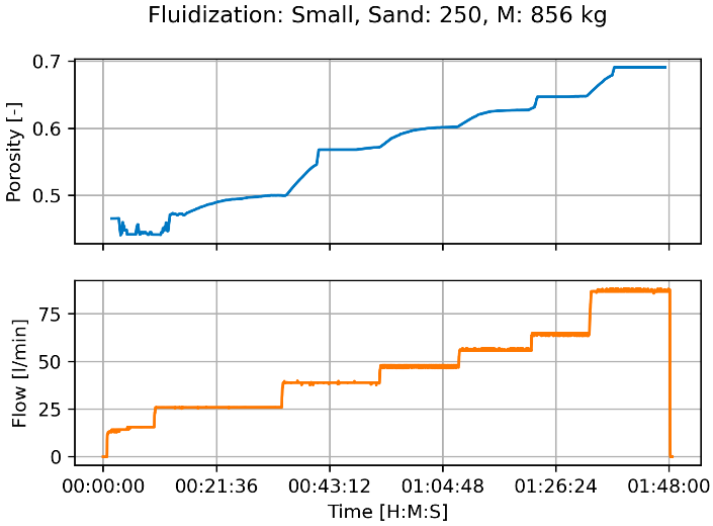

Figure 2.6: Small fluidisation test with sand particles with D50 of 250 micrometers

The penetration tests show that that an increase in porosity correlates with a faster penetration speeds, and thus higher flow velocities also lead to higher penetration velocity. However, changes in grain size were found to have no significant effect on penetration velocity of the monopile.

2.2. Effects on the plug formation process

This section focuses on the processes of erosion and sedimentation within the soil container, focusing on the displacement of the soil plug surface. By building upon the background theory section and taking into account the previous research by GBM Works, the expected conditions in the soil container are estimated. From there, state of the art studies in mostly dredging and coastal engineering that can describe the plug surface displacement are explained and compared. An equation to estimate the plug surface displacement was chosen in order to identify which parameters and processes have the most impact on the plug surface. Finally, the differences between the boundary conditions of the equation and the monopile

2.2.1. Soil container conditions

In the Introduction, Figure 1.6 illustrates the formation of the soil plug during laboratory tests. The picture reveals that the slope of the soil plug is quite steep, ranging between 45 and 90 degrees. This steepness exceeds the angle of repose of the soil, the measure of the inherent resistance of granular materials to sliding or flowing relative to the force of gravity, contributing to the instability of the soil plug. Previous tests by GBM Works have noted a high concentration within the trench due to fluidisation, with fluidised sand remaining at a concentration of 0.3 to 0.5. Although flow velocity is high near the jet at the trench's bottom, velocities at the top of the plug are unknown.

Figure 2.7 shows a 2D schematic of the plug surface process within the soil container, highlighting all the parameters used in the equations in this chapter. The colour coding of the parameters indicates their origin. Input parameters are those provided by suppliers or considered general knowledge. Measured parameters have been obtained from tests in the soil container using flow meters, sensors, and a camera. Finally, derived parameters are calculated using the equations presented in this Chapter.

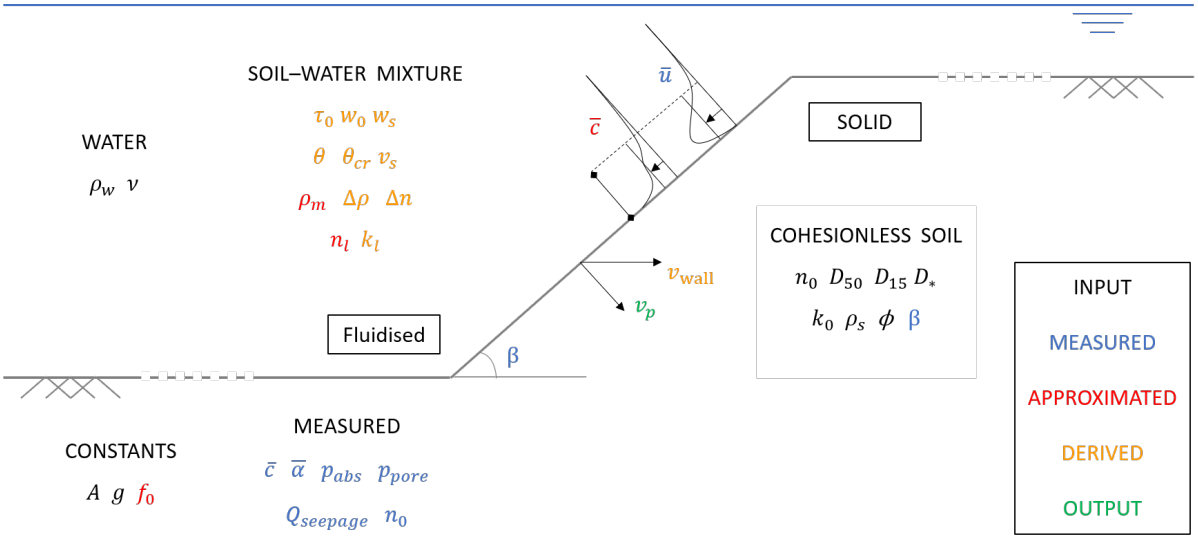

Figure 2.7: Schematic of slope erosion with all parameters

2.2.2. Single particle pick-up

The pick-up function's dependency on soil properties, flow velocity, and slope angle is highlighted, with Van Rijn's experiments offering valuable insights (van Rijn, 1986). His tests, covering flow velocities of 0.5 to 1.5 m/s and particle sizes from 130 to 1,500 micrometers, led to the development of an empirical pick-up function for estimating the pick-up rate of horizontal beds. This function, represented in the provided Equation 2.18, demonstrates the relationship between dimensionless particle diameter, flow conditions, and erosion mechanisms, specifically focusing on single particle pick-up dynamics. With D_* [-] the dimensionless particle diameter, which is given in Equation 2.19.

$$\Phi_p = 0.00033 D_*^{0.3} (\frac{\theta - \theta_c}{\theta_c})^{1.5} \tag{2.18}$$

$$D_* = \left[\frac{\Delta \rho g}{v^2} \right]^{1/3} D_{50} \tag{2.19}$$

The effect of sedimentation was included in the total erosion by Van Rijn. This results into Equation 2.20 for the erosion velocity and Equation 2.21 for the erosion rate.

$$v_e = \frac{E}{\rho_s (1 - n_0)} \tag{2.20}$$

$$E = 0.00033 \rho_s (\Delta \rho g D)^{0.5} D_*^{0.3} (\frac{\theta - \theta_c}{\theta_c})^{1.5} \tag{2.21}$$

2.2.3. High flow velocity erosion

As mentioned in the previous section the processes defining the pick-up function can differ when parameters are changed. Especially during different flow velocities sediment erosion process changes from grain by grain pick-up to high flow erosion, the latter will be discussed in this paragraph. van Rhee, 2010 studied the influence of high flow erosion and discovered that the conventional pick-up functions overestimated erosion at a high flow velocity. The reason is that, at higher velocities, sediment is eroded in layers. By taking dilatancy and the slope angle into account, the erosion rate can be estimated more precise.

Dilatancy and superficial flow

As mentioned, when the flow velocity and thus the erosion velocity increases, the erosion will shift from particle by particle pick-up to layer pick-up. Due to the high shear forces on the sediment bed, the assembly of particles will experience a change in volume, as illustrated in Figure 2.8. (van Rhee, 2010). On the left side the grain are compacted and after sheared the volume increases causing the grains to dilate. Consequently, the shortest way for the water to flow is perpendicular to the bed into the sheared area. The increase causes a negative pore water pressures (PWP) which in turn increases the effective stress, significantly decelerating the erosion process.

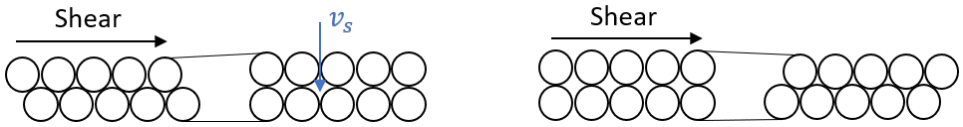

Figure 2.8: The dilatancy (left) and contractancy (right) by shear force on sediment bed, increasing and decreasing pore volumes

This increase in volume is shown in Figure 2.9. The volume that the particles use must be constant with both initial height h_0 and the upper layer height h_l, and therefore the porosity of the soil changes. Just like in the conservation of mass equation, the conservation of sediment can be written in Equation 2.22. The amount of extra volume must be filled with water and this is where the superficial flow velocity v_s comes at hand: $\Delta V = v_s \delta t$, which is the flow velocity of the water to the ins. Darcy's law states that the superficial flow velocity is equal to permeability times the hydraulic gradient i , given in Equation 2.24. The hydraulic gradient is a dimensionless parameter and shows the change in hydraulic head per unit distance between two points. When combining the effect of dilation with Darcy's law, it leads to the hydraulic gradient during high flow erosion, highlighted in Equation 2.25.

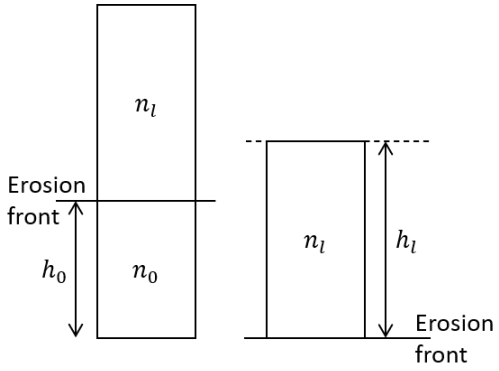

Figure 2.9: The increase of sediment zone volume relation

$$(1 - n_0)h_0 = (1 - n_l)h_l \tag{2.22}$$

$$\Delta V = n_l h_l - n_0 h_0 = h_0 \frac{n_l - n_0}{1 - n_l} \tag{2.23}$$

$$v_s = -k \cdot i \tag{2.24}$$

$$i = -\frac{v_e}{k_l} \cdot \frac{n_l - n_0}{1 - n_l} \tag{2.25}$$

Internal friction angle

The internal friction angle for soil ϕ is a measure of the soil's shear strength and is defined as the angle at which soil particles can sustain the maximum amount of shear stress without undergoing continuous deformation. The internal angle of friction is derived from the Mohr-Coulomb failure criterion, which describes the relationship between shear and normal stresses at failure, though this will be highlighted later in this chapter. The angle of repose is closely related to the internal angle of friction and represents the steepest angle of descent relative to the horizontal plane to which a granular material can be piled without being unstable. At this angle, the material on the slope face is on the verge of sliding down.

Adapted Shields parameter

As mentioned, the Shields parameter represents the ratio of the fluid force exerted on a particle to the gravitational force acting on the particle. The original Shields parameter is only viable for low velocities ($\bar{u}$ < 1) and did not account for slope angles of the soil bed. To enhance the Shields parameter, the influence of higher flow velocities and the slope angle are accounted for in the adapted Shields parameter:

Figure 2.10 illustrates particle stability, incorporating the forces due to the hydraulic gradient (F_i), gravity (G), and flowing water (F_s) (2.28). The calculations for G and F_i are provided by Equations 2.26 and 2.27, respectively. van Rhee, 2010 employs the relationship $F_s = G \tan \phi$ to establish the stability criterion for a horizontal bed in the absence of a hydraulic gradient.

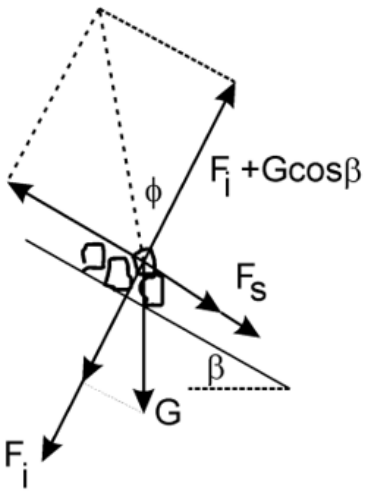

Figure 2.10: Particle stability including the influence of the hydraulic gradient

$$\text{Single particle pick-up: } G = 1/6\pi d^3 \left(\rho_s - \rho_w\right) g, F_i = 1/8\pi d^3 \rho_w g i \tag{2.26}$$

$$\text{Layer pick-up: } G = \left(1 - n_0\right) \left(\rho_s - \rho_w\right) g, F_i = \rho_w g i \tag{2.27}$$

$$\frac{F_s}{G} = \tan\phi \left(\frac{\sin(\phi - \beta)}{\sin\phi} + \frac{F_i}{G} \right) \tag{2.28}$$

When the hydraulic gradient and slope angle are accounted for, the result is Equation 2.29. The parameter A is set to $3/4$ for single particles and $A = 1/\left(1 - n_0\right)$ for a continuum, with the latter approach being utilised.

$$\theta > \theta_{cr} \left(\frac{\sin(\phi - \beta)}{\sin\phi} + A \frac{i}{\Delta\rho} \right) = \theta_{cr}^1 \tag{2.29}$$

Substitution of Equation 2.25 into the equation above results into the equation for the adapted critical shields parameter (θ_{cr}^1).

$$\theta_{cr}^1 = \theta_{cr} \left(\frac{\sin(\phi - \beta)}{\sin\phi} + \frac{v_e}{k_l} \frac{n_l - n_0}{1 - n_l} \frac{A}{\Delta\rho} \right) \tag{2.30}$$

It is important to note that this adapted Shields parameter can be incorporated into any pick-up function to account for the effects of dilation and slope angle. Integrating this equation into the pick-up function described by van Rhee, 2015 yields the following equation 2.31. Note that $R_c = \frac{1 - n_0 - c}{1 - n_0}$.

$$v_p = \frac{0.000616 u_s \frac{\theta R_c}{\theta_{cr}^1} - w_s c \cos\beta}{1 - n_0 - c} \tag{2.31}$$

2.2.4. Breaching

Jet movement and breaching

In the operation of a suction dredger, sediment is extracted from the bed interface, leading to the formation of a pit or cavity on the seabed. This extraction process results in the creation of a unstable under-water internal friction angle. As a consequence, a mixture of sand and water flows down the slope. This process of slope failure is called breaching.

Breaching is a gradual retrogressive erosion process of an underwater slope, steeper than the angle of repose. It takes place in medium dense to dense sands which show dilative behaviour upon shearing. The dilation causes an increase of the pore volume, creating negative excess pore pressures (suction), and thus increases locally the effective stress of the sand. This retards the erosion speed significantly, and therefore breaching is a (relatively) slow process. The inward hydraulic gradient due to the suction,

forces the water next to the erosion surface to flow into the pores. This happens until the negative excess pore pressures are dissipated and hydrostatic pressure is restored. The particles at the soil surface are destabilised and fall off the slope grain by grain.

The lab tests could result in a similar process. Initially, the soil surface inside the monopile is level. As the jet moves down, the elevated water velocity induces erosion, subsequently establishing an under water slope. When the jet reaches a critical depth, the slope surface becomes unstable, causing a slope failure, called breaching. It is noteworthy that while a suction hopper dredger moves horizontally, the jet moves vertically. The computation of the jet velocity (v_{jet}) is a straightforward geometric analysis.

$$v_{jet} = \frac{v_p}{cos\beta} \tag{2.32}$$

The wall velocity is a result of the breaching process[-] and can be compute using Equation 2.33 (Winterwerp et al., 1992). Parameter Δn represents the relative change in porosity from the initial porosity to the loose porosity, see Equation 2.34. Notice that this equation is also the product of Equation 2.30 when the adapted critical Shields parameter is set to zero.

$$v_{wall} = \frac{\sin(\phi - \beta)}{\sin\phi} \frac{\Delta\rho(1 - n_0)k_l}{\Delta n} \tag{2.33}$$

$$\Delta n = \frac{n_l - n_0}{1 - n_l} \tag{2.34}$$

Turbidity and density currents

Turbidity currents are a sub-type of density currents, they are highly concentrated currents which are induced by gravity (Parker et al., 1986. The flows are created by the breaching process where particle on an unstable slope roll down one by one. Due to the higher density of the mixture compared to the surrounding water the mixture turns into a higher velocity flow, shown in Figure 2.11. Turbidity currents can create a shear stress on the sediment and therefore erode additional sediment of the bed interface (Akiyama and Stefan, 1985). Although, at a more gentle slope the force of gravity is less effective and the velocity of the current smaller, resulting in sedimentation.

Alhaddad et al., 2020 studied the steepness and propagation velocity of the underwater sand slope. The execution of large-scale model tests showed that the angle of the slope is not only dependent on sand characteristics but also the height of the breach and the effect of density currents, which will be discussed in the next paragraph.

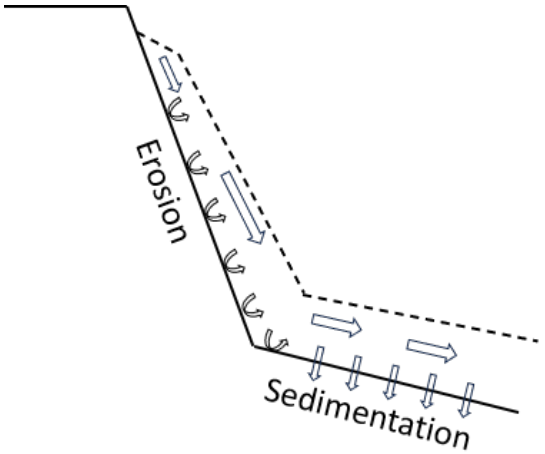

Figure 2.11: Processes during turbidity currents

Breaching and the emerging turbidity currents can cause movement of the bed interface by the shear forces that are directed on the sand bed. Mastbergen and Berg, 2003 derived an analytical equation for this effect which can compute gradual retrogressive failure of a steep slope in non-cohesive sands. The equation originates from a pick-up function which incorporates the slope angle of the bed interface was used, as shown in Equation 2.35 (Winterwerp et al., 1992).

$$\Phi \left\{ 1 - \frac{\tan(\beta)}{\tan(\varphi)} \right\} = A \left(\theta - \theta_{cr}\right)^m D_*^n \tag{2.35}$$

This equation was rewritten to account for the dilation effect given in Paragraph 2.2.3. By combining Equation 2.15, 2.33, and 2.19. For the Shields parameter a different equation is used than in Van Rhee's study, namely the averaged flow volumetric concentration over flow layer thickness ($\bar{c}$) was added to account for the influence concentration of particles in the flow. The resulting total plug surface velocity is stated in Equation 2.37, which describes the velocity perpendicular to the plug surface. The Shields velocity is used to purely for simplicity of notation, which contains: $u_s = \sqrt{\Delta D_{50} \rho}$. The full derivation and explanation of this equation was added to appendix A.1.

$$\theta = \frac{f_0}{8} \frac{\bar{u}^2}{\Delta \rho g D} \tag{2.36}$$

$$v_p = u_s \left(\frac{v_{wall}}{2u_s} + \sqrt{\left(\frac{v_{wall}}{2u_s} \right)^2 + 0.018 \left(\theta - \theta_{cr}\right)^{1.5} D_*^{0.3} \frac{\Delta \rho k_l}{\Delta n u_s}} \right) \tag{2.37}$$

It is important to note that when the critical Shields parameter is less than or equal to the Shields parameter ($\theta_{cr} \leq \theta$), erosion due to water flow is absent, and the plug surface velocity matches the wall velocity. In the application of the derived equation, the following considerations must be acknowledged:

- The equation is most accurate for concentration levels ranging between 5 and 40 percent.
- The equations are tailored for channels with a height up to 5 meters.
- The derived equations assume that the flow is parallel to the slope.
- The equation accounts for both low and high flow rates, aligning with the findings of van Rhee, 2010.

2.2.5. Plug surface velocity equation

The previous part of the literature mentions two main equations that could be used to estimate the plug surface velocity. Now the strengths and weaknesses of both theories will be compared to make sure the most accurate equation was chosen.

Van Rhee's theory (Equation 2.31) was validated using data from previously conducted lab tests, for example from Roberts et al., 1998. These tests are horizontal tests and aim to validate the high flow velocity mechanism but no effects of pure breaching. They were performed in fume with a broad range of particle sizes and different relative densities. Although, the results were not perfect, the plug surface velocity was still overestimated in several tests.

Mastbergen's theory (Equation 2.37 was validated based on data of van Rijn, 1984 and Winterwerp et al., 1992 which are also flume experiments. Though these studies do include tests with slope angles. In Alhaddad et al., 2020 large scale experiments on breaching flow slides were in the water lab of Delft University of Technology. Appendix A.1 shows a picture of the lab setup which reached initial slope angles between 50 and 80 degrees. The soil container was 4 meter long, 0.22 meter wide and 2 meter height, which is close to the 0.3 meter width of the soil container in this study. A study by Alhaddad et al., 2021 compared both Van Rhee's and Mastbergen's equation and concluded that the latter was in good agreement with the data and outperformed Van Rhee. Van Rhee's estimation of the plug surface velocity was twice as high as it should have been. There are two main differences between the conditions in the large scale experiments and the conditions inside the monopile during jetting.

- The surrounding water next to the soil is clear vs. a high concentration SW-mixture during jetting
- There is no seepage happening because there is no outlet beneath the soil vs. an open bottom of the monopile for potential seepage flow
- There is no added water inside the soil container vs. a jet ring which jets water on the bottom of the fluidised area

2.2.6. Added effects during monopile installation

As mentioned above there are multiple effects which are have not been incorporated in the equation by Van Mastbergen. In this paragraph the impact of these added effects will be discussed.

Influence high concentrations

During fluidisation, high concentrations of sand in the fluidised mixture will be met. Based on previous research of GBM Works the volumetric concentration in fluidisation could go from 30 to 50 percent. In the case of a density current the percentage might even be more than 50 percent.

The study by van Rhee and Talmon, 2010 explored the impact of sediment concentration on particle pick-up within a closed-loop horizontal cylinder, where a sand and water mixture of high concentration was circulated and the displacement of the particle interface was monitored. The researchers proposed that, due to the principle of continuity, an eddy transporting a volume of water and sediment away from the bed necessitates the return of an equivalent volume of water to the bed surface. At lower sediment concentrations, this returning flow (backflow) carries fewer particles. Conversely, with an increase in the near-bed sediment concentration, the backflow is more likely to transport particles back to the bed. In scenarios where the concentration near the bed closely matches the bed's own sediment concentration, the study found that there would be no net sediment transport away from the bed by turbulent eddies, indicating a balance between the sediment lifted by the flow and that returned by backflow.

The high concentration also impacts the pressure difference inside the monopile. Because the sand is fluidised, which means concentration c = 0.3 - 0.5, the density of this mixture is higher than the density of the water. Therefore, the increase in pressure can be predicted by Equation 2.38. This increased pressure has an influence on the seepage inside the monopile, which will be explained in the next paragraph.

$$\Delta p = (\rho_m - \rho_w)gh \tag{2.38}$$

Influence of seepage

A discrepancy of the equation by Van Mastbergen is that the erosion velocity is not always positive. Under certain conditions, even gentle slopes are stable and do not experience erosion. Furthermore, very steep slopes can accumulate sediment, depending on the dynamics involved. Consider the phenomenon of plastering on borehole walls: if the water flow toward these walls is sufficiently strong, it can transport particles to the wall. Once there, these particles may be held in place by the groundwater pressure gradient, effectively creating a sediment-plastered surface despite the steepness or inclination of the wall (He et al., 2019).

During the offshore installation of monopiles using the Vibrojet® technique, an excess pressure is generated by the jetting action at the bottom of the pile and the increased SW-mixture density. This excess pressure may induce a water flow beneath the pile rather than inside it. This phenomenon, referred to as seepage in this study, can influence the installation performance and the pile's stability by altering the soil conditions around and beneath the pile.

A study by van Rhee and Bezuijen, 1992 showed the influence of seepage of an underwater slope without initial fluid fluid velocity along the slope. Due to the difference in water height between two areas, a flow is generated between these areas. The hydraulic gradient is the head difference divided by the distance of two areas. Figure 2.12 shows both stable and unstable slope angles with a certain hydraulic gradient and two modes, single particle and continuum mode. In single particle mode the single grains are analysed and counted unstable when the grains start rolling. Consequently, in continuum mode a slice of particles perpendicular to the slope is analysed assuming that the forces acting on the whole slice are equal.

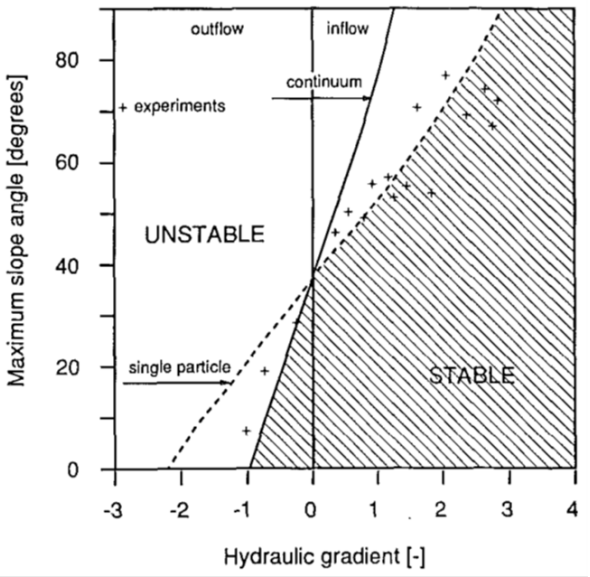

Figure 2.12: Influence of seepage on slope stability

Furthermore, Paragraph 2.2.3 mentions Equation 2.27, which gives the computation of force of the hydraulic gradient F_i or seepage force (van Rhee, 2010). In this equation v_s represents the superficial velocity of the water into the soil plug. The seepage flow rate would work against the effect of dilation since the water would literally flow further away into the soil and through the underside of the monopile. Equation 2.39 shows the relation between the seepage flow rate and the superficial velocity.

$$v_s = \frac{Q_s}{A} \tag{2.39}$$

- A[m^2] - the cross sectional area

2.3. Shear strength inside the soil plug

The formation of the soil plug results in increased gravitational forces on a given layer within the plug, escalating with the height of the soil plug. This section examines the shear strength within the soil container, specifically addressing the impact of soil plug formation on the plug's stability. Terzaghi, 1943 gives insight in this part.

The axial stress is the stress acting along the vertical axis of the soil element. In the case of a pile or a column of sand, this would be the stress due to the weight of the sand above any given point, acting downward, illustrated in Figure 2.13.

The radial stress is the stress acting horizontally and perpendicular to the axial stress. In a laboratory test environment, where a soil cylinder is enclosed, radial stress specifically refers to the confining pressure applied horizontally onto the sample. This pressure, acting inwardly and perpendicular to the vertical axial stress, simulates underground soil confinement conditions. For a freestanding pile of sand, the radial stresses on the sample are zero because there is no confinement pressure. Without confinement, sand does not exert radial stress and the steepest slope matches the angle of repose for non-cohesive soils.

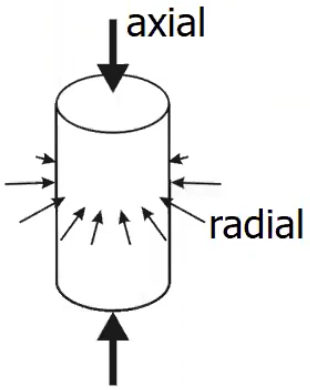

Figure 2.13: Axial and radial stresses on a soil plug

A triggering mechanism for slope failure occurs when the down-slope oriented shear stress (driving shear stress) exceeds the shear strength (resisting stress) of the material forming the slope, as expressed by the well known Mohr–Coulomb failure criterion, given in Figure 2.14. It is a model used in geotechnical engineering to describe the response of materials such as soils, rocks, and concretes under shearing stresses.

The Mohr-Coulomb failure criterion is defined by an envelope that intersects the Mohr's Circle at the critical condition of material failure. This failure envelope is characterised by the angle of internal friction, ϕ, which is a linear representation of the relationship between shear and normal stresses. When the Mohr's Circle intersects this envelope, the soil reaches a failure state, characterised by the loss of shear strength and the inability to support further loads. This condition initiates particle displacement along potential failure planes, manifesting as deformation and ultimately leading to slope failure within the soil plug.

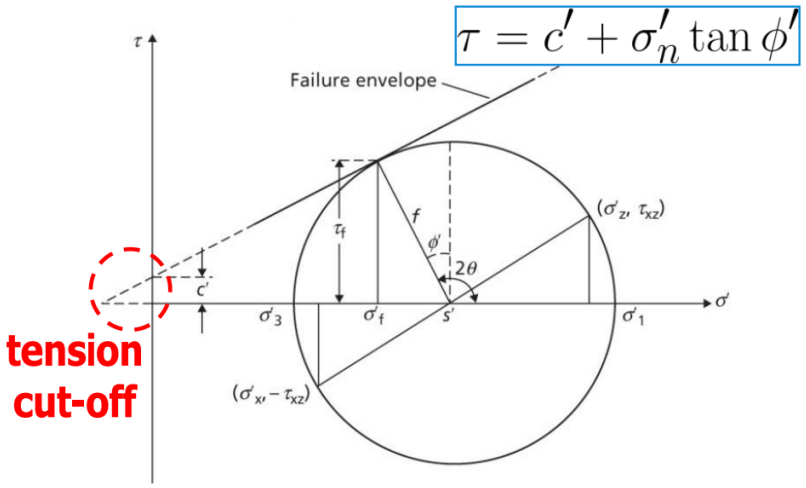

Figure 2.14: Mohr-Coulomb failure criterion

- τ [Pa] - the vertical axis represents the shear stress within the soil plug.
- c' [Pa] - This is the effective cohesion of the material, indicating the portion of the shear strength that is independent of the applied normal stress. It's the intercept of the failure envelope with the shear stress axis.
- σ_n' [Pa] - the effective normal stress. It's the axial stress applied along the length of the cylinder, which is induces by the weight of the soil plug pressing down. The effective stress is the stress

in the soil sample, excluding the pore pressures: σ' = σ - u (u is the pore water pressure).

- σ_3' [Pa] - the effective minor principal stress, also known as the confining pressure. In the soil container, this stress is applied radially and is equal in all directions perpendicular to σ_n.

In the case of Vibrojet® installation, there will be slope failure if parts of the soil plug have insufficient support, those parts could fail under their own weight and slide down. As the monopile penetrates deeper into the seabed, the height of the soil plug within the monopile increases. This height increase results in gravitational stresses exerted by the soil mass on the lower sections of the plug. Gravitational stress, acting vertically downward, contributes significantly to the vertical normal stress component within the soil matrix. Dependent on the internal angle of friction, the effective cohesion, and the PWP inside the plug this normal stress enhances the shear stresses in the lower sections of the plug. The PWP inside the plug is dependent on the inward flow from the fluidised area.

When the soil plug gets taller, the PWP inside the fluidised zone at the lower sections of the plug gets higher. This induces inward flow to the inside of the soil plug, increasing the PWP pressure inside the soil plug. Subsequently, a higher PWP opposes the effective normal stress inside the plug which leads to a lower effective stress. Lower effective stress means that the soil particles are less tightly pressed together, reducing frictional resistance among particles and thus weakening the soil structure. Though, seepage flow underneath the monopile could reduce the PWP because it draws away the water from the inside of the plug. This decrease in PWP increases the stability of the soil plug.

The actual presence of these phenomena inside the monopile have to be measured, but it is clear that the PWP and seepage could have a significant impact on the stability of the soil plug. This stability is essential for the performance of the Vibrojet®, because if a slope failure occurs, a slide may hinder the fluidisation process and cause unwanted inner shaft friction during monopile installation.

2.4. Literature gaps and limitations

To summarise, the displacement of the soil plug during tests, when exceeding the internal angle of friction of the sand particles, is influenced by soil pick-up, pure breaching, sedimentation processes and added seepage. Numerous studies have sought to encapsulate these dynamics into equations capable of estimating the plug surface velocity. Among these, the equation referenced as 2.37 aligns most closely with the test conditions anticipated in this research and will thus be employed for the evaluation of laboratory tests. However, it is important to note that there are differences such as a SW-mixture environment, potential seepage flow and jet flow.

Firstly, there appears to be a consensus in the literature that there are two erosion regimes, namely low and high flow velocity (van Rijn, 1986, van Rhee, 2010, Mastbergen and Berg, 2003). The latter takes into account the dilatancy effect, which significantly reduces the total erosion velocity. Nevertheless, there seems to be no study that has experimented with tests above 6 m/s flow velocity above the bed (van Rhee, 2010, Bisschop, 2018). Subsequently, the influence of an inward hydraulic gradient was calculated by van Rhee, 2010 and van Rhee and Bezuijen, 1992 as a function of permeability and plug surface displacement. However, only the effect of dilatancy and no additional seepage was considered in the current plug surface displacement models. The effect of seepage has been incorporated in several lab tests. Additionally, there has been research on high-concentration erosion and sedimentation, but these numbers only go up to 40 percent. In the case of the soil container, the concentration of the sand-water mixture will probably reach 50 percent volumetric concentration, and maybe even higher. The equations shown in the literature review have not been evaluated for these concentrations. Finally, the pressure in the soil container due to the SW-mixture will be higher than the hydrostatic pressure of only water. The influence of this pressure is uncertain but will be measured during lab tests.

In the context of Vibrojet® installation, the shear strength within the soil plug is critical for maintaining stability and preventing slope failures. This strength is influenced by the effective stress, which is reduced by increased pore pressures during intense jetting activities. The phenomena within the monopile, such as jet flow, increased pressure due to suspended particles, and seepage flow, could significantly influence the triggering of slope failure. A slope failure could induce inner shaft friction, which is potentially fatal for the performance of the Vibrojet®.

The assumptions made in this chapter could impact the final results concerning the soil plug and the accuracy of the lab simulations. These assumptions are explicitly stated to guide the analyses in the next chapters.

- The soil is assumed to be homogeneous, although it is acknowledged that real soil conditions may vary.
- The soil plug is assumed to be axis-symmetric around the pile wall, which simplifies the modelling but does not account for irregularities in actual conditions.
- The sediment layers are consistent and continuous, which may not be the case with layered geological formations.
- Darcy Weisbach friction factor is assumed to be 0.01, this has significant impact on the erosion due to flow and may need to be updated.
- Flow conditions are assumed to be uniform across the soil plug, simplifying the analysis of fluid-induced forces.
- Assumes a uniform distribution of particle sizes and types within the soil, which influences the initiation of turbidity currents.
- Laboratory scale effects are often not representative of field conditions; however, this assumption is necessary for experimental validation. Assumes that laboratory or field environments can be controlled or approximated well enough to validate theoretical models.

3

Imitating Vibrojet® installation with lab tests

This chapter outlines the design of the experimental setup, how it imitates a real offshore installation using the Vibrojet® and what its limits are. It covers all hardware used in the lab, such as the soil container, the sand, the sensors, the jet, the pump, and the camera setup. Then, it elaborates on all the flow processes used to consistently conduct all tests, which is critical when the final results are compared. Then, it continues on the lab tests that have been executed, and why these particular tests have been chosen.

The chapter aims to answer two main questions:

1. How can a Vibrojet® installation be imitated in a lab most effectively?
2. Which tests provide the most value for identifying Vibrojet® performance?

To answer these questions the chapter is divided into three main sections. The first two sections answer the first research question by delving into the design of the lab tests in 'Lab Setup at Deltares Institute' and explain the way tests are executed to maintain consistent results in section 'Flow Processes during the Testing Phase'. In the final section, 'The Test Matrix: Selection of Installation Settings', all possible installation settings will be evaluated based on their added value and time consumption, in order to identify those that yield the best results.

3.1. Basis of design: the lab test setup

This section delves into the basis of the design of the laboratory test setup used to research the optimal performance settings of the Vibrojet®. Figure 3.1 provides a comprehensive view of the lab setup at Deltares, where the entire construction was built and tests were carried out over a period of six months. Furthermore, the general design of the test setup is elaborated upon, followed by a discussion of all components used in the lab tests alongside the limitations of the setup.

As mentioned in the introduction, the objective of these tests is to optimise the performance of the Vibrojet® during offshore installation by analysing the impact of the installation settings on the plug formation inside the monopile. To measure the formation of the plug, it is necessary to have a view of the cut-through of the monopile during installation; therefore, the choice was made to create a 2D setup that replicates the interior of the monopile. The front of the soil container was made of Perspex, which allows the camera to capture the plug formation during the tests.

When designing the lab test setup, several design requirements need to be met to ensure the validity and effectiveness of the experiments. Those requirements are:

- Effectiveness: the ability of the setup to mimic the real installation environment of the Vibrojet®
- Functionality: allow two people to monitor and control tests
- Total costs: develop a budget-conscious laboratory setup
- Safety: adhere to all safety standards, minimising the risks of accidents

Figure 3.1: The lab test setup at Deltares Institute

List of components of the lab test setup:

[1] Soil container - enclosure of the testing en
[2] Linear guide - enables vertical jet displacement during testing
[3] Water pump - creates the water pressure for fluidisation or jet loop
[4] Water reservoir - 2x 1000 litre water reservoirs hold enough water for several tests
[5] Controller - data acquisition system for taking measurements, camera switch and jet control
[6] Camera & anti reflection screen - record the lab tests and block reflections from the soil container front

Figure 3.2 illustrates the lab components in a schematic way, the blue stripes depict the directions of the water, the full arrows dimensions of the inner container and the dotted stripes adjustable heights. Water is pumped from both reservoirs to the movable jets, via which the water enters the soil container. This way the soil sample is jetted away underneath the jet, leading to an plug surface over the length of the soil container. The water flows out at the top over the of the soil container at the front into a drain. The bottom of the soil container contains a water compartment, which is separated from the soil sample via a filter system. This water compartment is connected to a second compartment, which is used to control the hydraulic head Δh in the water compartment and thus the hydraulic gradient over the soil sample.

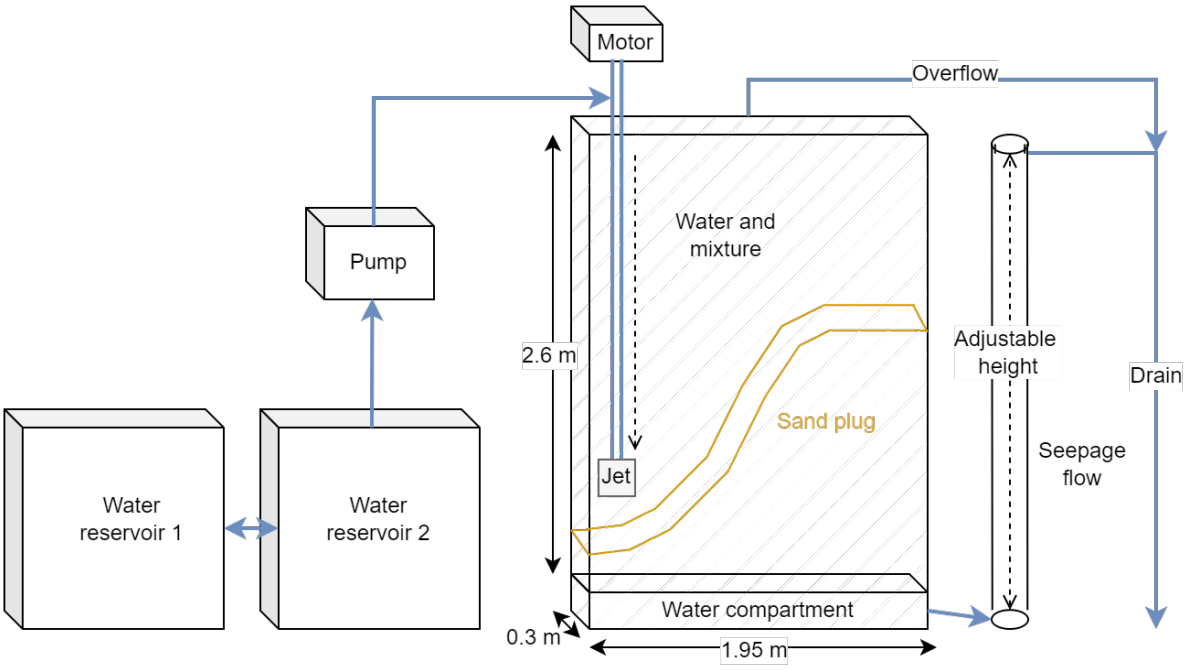

Figure 3.2: Drawing of the of lab test setup

Soil container

The test setup consists of a soil container, which represents a strip of the soil inside the pile from the pile wall to the centre of the pile. It is a 'flat' soil container, which is slim in comparison to the length and height in order to perform a plain-strain test, but not too slim, in order to avoid significant wall effects on local jetting and sediment transport mechanisms. The soil container is 1950 mm long, 2600 mm high and 300 mm wide inner dimensions. A approximately 2 meter long soil container can represent a 4 meter diameter pile. The height of 2.6 meter can support a 1.5 meter high soil sample with an expansion of 50 percent, a buffer with clean water, and the overflow height. The width of 0.3 meter of the container is both for practical and hydrodynamic reasons. A standard shovel can fit into the soil container and 300 mm is more than 300 times the lager than the D90 of the sand particles, which is deemed enough for the hydrodynamic and soil surface processes to be investigated accurately. In Alhaddad et al., 2020, a 220 mm wide container was used to conduct breaching experiments, and supported the data for the plug surface displacement equation. Since the monopile is round, a perfect representation of the monopile would be a 'pizza slice' shape, though this is not totally true. When scaling the cut through to higher monopile diameters this 'pizza slice' gets a more rectangular shape. Additionally, this would complicate the design of the soil container and influence the flow at the narrower side of the soil container. Therefore, the choice was made to use a rectangular size shape soil container.

The back and sides of the soil container are made of steel which are able to resist the loads that will be put on the container when lifted from the ground and support the Perplex plate. Which brings us to the front of the container is made of a see-through Perplex plate which enables the recording of the tests. The yield strength of the Perplex is much lower than the steel and needed to be 10 mm thick to withstand the pressure during fluidisation. With FEM calculation the thickness of both materials were calculated and the maximum strain of the Perspex was accounted for. The size of the soil container was mainly based on the dimensions of the Perspex which would become both costly and unmovable.

The frame around the soil container was designed with multiple purposes in mind: it enhances the stability of the soil container, facilitates the use of the linear guide, and provides connection points for coupling hoses to the jet.

Sensors

Figure 3.3 presents a visual depiction of the soil container's front and side, highlighting potential locations for pressure sensors. For these experiments, three types of pressure sensors are employed: pore pressure, total pressure, and absolute pressure sensors. Due to the Data Acquisition (DAQ) system's limitation of handling only eighteen pressure sensors, a selection process was necessary. Figure

3.3 illustrates all potential sensor locations, with stars indicating pore pressure sensors and hexagons representing total pressure sensors. Furthermore, the Appendix A.2 provides a detailed overview of the precise locations of these sensors.

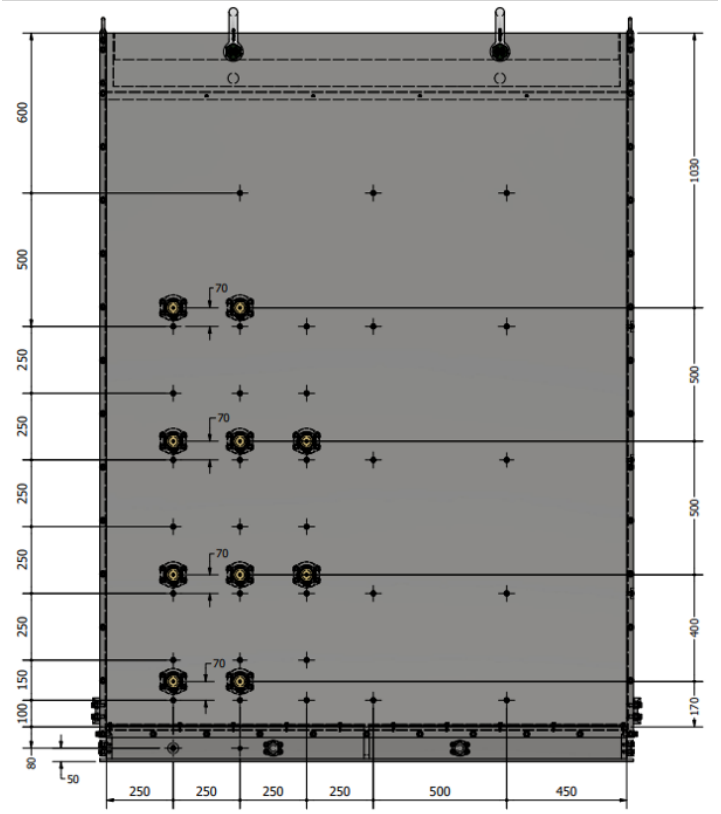

Figure 3.3: Potential sensor locations on the front of the soil container

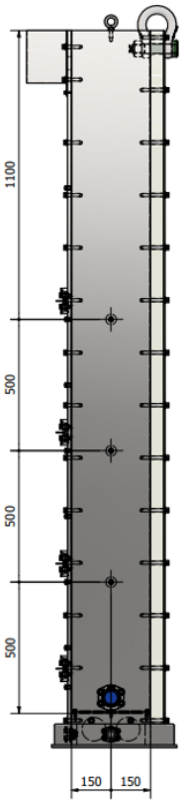

Figure 3.4: Potential sensor locations on the side of the soil container

The three sensor types are chosen because it enables cross-validation and a more comprehensive analysis can be done. The calibration and validation of the sensor data was done in Chapter 4. The pore pressure sensors measure the pressure of the water within the pores of the soil, i.e. pore water pressure p_p. This is useful for understanding how water pressure within the soil matrix changes under different conditions. Total pressure sensors measure the combined pressure exerted by both the soil solids and the water within the pores, i.e. total pressure p_t. It gives an overall stress state of the soil and can be used to analyse the load-bearing capacity of the soil. Finally, absolute pressure sensors measure the pressure relative to a perfect vacuum. It includes the atmospheric pressure as a baseline and can therefore be used calibrate the other sensor when there are atmospheric variations.

Jet and pump

The jet is one of the most crucial components of the lab setup, as it simulates the downward movement of the monopile by moving downward in the soil container. This downward movement is facilitated by its attachment to a linear guide, which moves up and down during tests and can be regulated with the controller integrated into the DAQ system. In every test the jet start at the same position at the top of the soil container underwater. Then it moves to the same lower position with the selected jet penetration velocity till it reaches the position of H = 1400 which is near the bottom of the soil container. It stays there till the soil plug shape is stable and move back up again to initial position.

The jet comprises a manifold, a milled piece of steel that divides the water flow from the inlet into four nozzles. These nozzles feature a threaded connection, allowing for the replacement of different nozzle types. During calibration tests, several nozzle types were tested and the most effective nozzle type was determined through measuring the distance between jet and the bottom of the trench. The nozzles had three different diameters, namely 2.36 mm, 3.97 mm and 5.16 mm. The nozzle that performed the best

is the FS-NF40-90, which is a round nozzle that has a diameter of 3.97 mm. The manifold consists of 6 nozzles next to each other.

The generate pressure in the jet the pump is connected to a hose, which leads to the inlet of the manifold. The pump type is a Ebara EVMS 20 12/15 Vertical Multistage Pump which is an centrifugal pump. As its blades start accelerating, the fluid moves to the outer edge of the pump, subsequently creating pressure due to the conversion of the fluid's kinetic energy into potential energy, resulting in an increased pressure head that enables the fluid to be efficiently transported through the pump's discharge outlet. The pump's operation is controlled by frequency, and during the calibration tests, this frequency was linked to the flow rate of the jet to ensure a consistent flow rate. Flow rates between 80 to 120 L/min were selected based on the functionality of the jet. Flow rates below 80 L/min prevented the jet from moving downward, which was necessary for the consistency of the tests. The maximum flow rate was chosen to align with the capacity of the two water reservoirs, allowing the setup to perform consistently throughout a 15-minute test.

The pump capacity is depicted by two parameters: the pressure and the flow rate it can produce. This needed capacity comes down to respectively 26 bar and 500 l/min.

- The maximum flow rate is dependent on the mass of the sand since it needs to be fluidised. Using previous studies by GBM Works, for full fluidisation the flow rate needs to be at least 200 l/min to fluidise half of the sand mass (GBMWorks, 2020). As a safety factor a 500 l/min was chosen.
- The maximum pressure is a combination of the pressure loss in the hoses, valves and the nozzles. Whereas the nozzles are the leading factor. The pressure loss over the nozzles was calculated by using Bernoulli's Equation 3.1 and the maximum flow velocity inside the smallest nozzles, which is dependent on the nozzle diameter.

$$p_1 + \frac{1}{2}\rho v_1^2 + \rho g h_1 = p_2 + \frac{1}{2}\rho v_2^2 + \rho g h_2 \tag{3.1}$$

$$p = 0.5 * \rho_w * v_{nozzle}^2 = 23 \text{ bar} \tag{3.2}$$

Compared to the actual jet ring that will be utilised during installation, there are several notable differences. As depicted in Figure 3.5, the protective casing around the jet, present in real-world scenarios, is absent during lab tests. This omission could slightly impact the fluidised stream, allowing it to bypass the left side of the jet. Additionally, the jets in real-world tests are angled at 45 degrees to improve the fluidisation process. Such conditions are impossible to replicate in 2D setup of the lab, leading to differences between the laboratory environment and real-world installation scenarios.

Figure 3.5: HKW jet ring in $2.3m$ diameter monopile

Sand types

Three sand types were used during the lab tests which are similar to the soil types in the North Sea. The sand types are characterised by fine, medium and coarse sand and their characteristics can be found in table 3.1.

Sand types	**Fine**	**Medium**	**Coarse**
Code	S90	M31	DS0
D_{50} [μm]	153	337	620
Density [kg/m^3]	2662	2650	2650
Internal friction angle [°]	-	34.54	35.28
Minimum porosity [-]	0.42	0.37	0.4
Maximum porosity [-]	0.48	0.47	0.5

Table 3.1: Sand properties

Sandy sediments are prevalent in the North Sea, especially in shallower areas and along coastlines. The weight of the overlying sand layers causes the underlying sediments to compact, affecting their relative density, which consequently can vary with depth. This variability is particularly evident in zones of significant sediment accumulation. For example, in regions with strong currents, sediments tend to be coarser and less compacted due to the constant agitation, whereas in areas with calmer conditions, sediments are typically finer and more compacted due to less disturbance.

A total mass of $m_{total} = 1500$ kg ('normal' sand + UV sand) was inserted into the soil container. It is important to account for the observed overflow losses, that comprises of the soil water mixture that flow out of the top of the container. The value of m_{total} is not expected to deviate by many kilograms; nonetheless, it is mentioned here for completeness. For medium sand, the estimated loss is approximately 10 kg over 30 tests.

Using a vibratory hammer, the sand is compacted to the correct relative density at the beginning of each test. To achieve the desired relative density, the target height is calculated and listed in Table 3.2, utilising Equation 2.10. During the tests, the Perspex bowed in the middle of the container, leading to an increase in the sand volume based on height. This effect was accounted for in the adjustments. The equations for the calculation of this height can be found in Chapter 2.

Density	Relative density [%]	Height in Soil Container [cm]
1642	50	151
1709	75	144
1776	100	139

Table 3.2: Relative density medium sand compared to the height in the soil container

Camera and UV lighting

In order to process the vast number of tests conducted with this lab setup, UV particle tracking is utilised to measure the movement of particles within the soil container. These UV particles are coated, allowing them to illuminate when exposed to UV light with a wavelength of 320 to 400 nanometre. All tests are recorded using an 8K camera (*Canon EOS R5* with a resolution of 7680 x 4320 pixels) and analysed using visual software specifically developed for this study, which will be further discussed in section 4.2. This software enables the recognition, analysis, and processing of the moving particles to calculate the flow velocities and plug shape.

To ensure optimal saturation, several preliminary tests were conducted with small amounts of sand under UV light. These tests determined that an optimal saturation is achieved when precisely 0.3 percent of the total sand mass consists of UV particles. Additionally, to prevent any bright reflections from interfering with the delicate process of particle recognition, a light screen was installed in the lab, and lights were turned off during the tests.

Limitations and considerations

Given the disparities between the laboratory test setup and actual offshore installations, it is important to acknowledge a set of limitations and considerations. These considerations are crucial to understanding the extent to which laboratory results can be extrapolated to real-world scenarios:

- The processes inside the pile are assumed to be axially symmetrical, leading to a circular sector or "pizza slice" shape. However, the soil container is shaped as a strip to conduct a plane-strain test, causing the mechanisms inside the soil container to exhibit 2D behaviour instead of the 3D

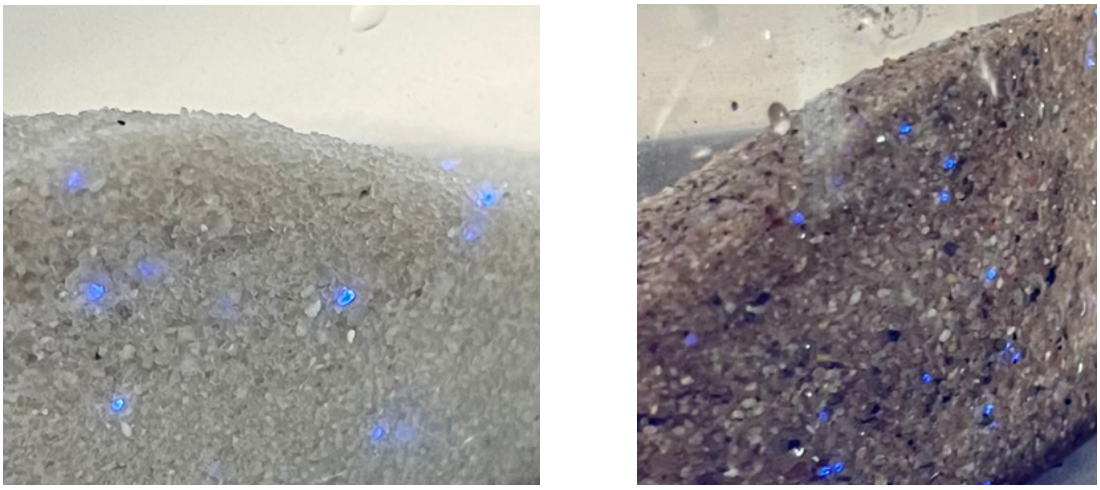

Figure 3.6: UV response tracer sand samples

behaviour observed inside an actual pile. Nonetheless, the validity of the plane-strain assumption improves with the increasing dimensions of the pile to be installed. The dimensions of the soil container also influence flow processes and stresses acting on the soil plug. Although the size of the soil container is bigger than previously performed tests, scaling to offshore monopile installation could lead to higher flow rates and plug displacement.

- The range of interest for installation depth extends up to 40 meters into the soil. However, the test setup accommodates only approximately 1.5 meters of sand sample, thereby replicating only the uppermost part of the installation. Despite this limitation, the setup provides valuable insights into the behaviour of fluidization around the jet and plug surface displacement processes along the slope, which can be extrapolated to greater heights. Nevertheless, as highlighted in the literature review of this study, greater depths could lead to an increased axial stress component, potentially affecting plug stability.
- Vortex flow is not included in this test setup. In the jet ring design, the jets are jetting under a 45 degree angle in tangential direction, which generates circular flow (vortex) around the pile wall. This vortex is expected to increase the homogeneity of the fluidisation around the pile decreasing the likelihood of generating preferential flow paths. Because of the circular speed direction, the vortex will lead to less erosion opposed to having the same flow speed without vortex. Therefore, excluding the vortex in the laboratory tests is expected to lead to larger erosion profiles at equal flow rates.
- Vibrations will also play a role in the pile, because they influence the pore pressures, and could influence the plug displacement and stability. On the bottom of the North Sea, there are layers of sand, rocks and other kinds of debris which could influence the Vibrojet® performance. However, these effects are not included in the scope of this research.

3.2. Operational phase: consistency during lab tests

This subsection outlines all flow processes within the soil container necessary for conducting multiple tests, including the piping and instrumentation required for both preparation and the testing phases. Consistency is achieved through standardised procedures that are rigorously followed for each test, ensuring that all experiments are conducted under uniform conditions. This standardisation is essential for the reproducibility of results and for enabling valid comparisons between different test scenarios.

Initially, the sand must be prepared and evenly distributed within the soil container, ensuring uniform particle sizes without any layering, achieved through sediment fluidisation. Subsequently, water is directed to both the jet and the underside of the soil container to facilitate the jetting and fluidisation loop. Additionally, to accommodate water discharge during the tests, the system incorporates an overflow at the top of the soil container and a seepage system at the bottom of the soil container. Figure 3.7 provides a detailed view of the piping and instrumentation arrangement, with numbered pipes indicating the flow processes in sequence according to the flow direction.

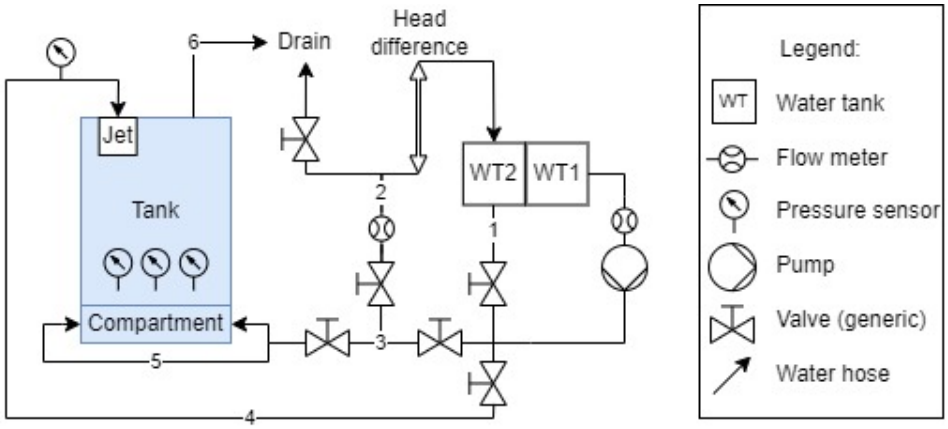

Figure 3.7: Piping and instrumentation diagram

- Bypass loop [1]
- fluidisation loop [3-5]
- Jet loop [4]
- Overflow [6]
- Seepage [5-3-2]

Bypass loop

The bypass loop is the system's shortest loop and redirects the water directly back into the water compartment. It plays a crucial role in establishing a steady flow velocity and ensuring no excess air is present in the pump before testing begins. Additionally, the pump should never operate without an open flow path, as this could damage the pump and other system components. The bypass loop also serves an essential safety function during testing; it can quickly relieve all pressure in other loops if issues arise, such as an overflow in the soil container due to a blocked overflow or an empty water compartment.

Fluidisation loop

Every time a new test begins, ensuring that the sand is evenly distributed within the soil container is crucial. This uniformity means that the sand's characteristics, like grain size, shape, and composition, remain consistent across the container. Such consistency is vital for the sand to demonstrate uniform physical behaviour, which is key for obtaining accurate experimental results.

To achieve an even sand distribution, the procedure involves fluidising the sand twice to ensure a uniform fluid flow throughout it. The pump exerts hydraulic pressure from the bottom of the soil container (compartment) to start the fluidisation. The water flows evenly through the geotextile filter on the bottom of the container, which is fine enough to block the sand particles on top but lets the water go through.

However, it's important to acknowledge that once fluidisation ceases and the fluid flow diminishes or stops, the sand particles will settle. This settling can influence the ultimate sand distribution, potentially causing some segregation, particularly with varied particle sizes. Before starting of the test phase, calibration was done with different pump frequencies to ensure optimised fluidisation in between test, resulting in more efficient testing.

Jet loop

The jet loop serves as the primary component of the testing system, supplying water to the manifold. It is outfitted with both a pressure meter and a flow meter. The flow rate is critical for conducting various tests and ensuring there is a steady flow. The pressure meter is crucial for detecting any leaks around the the manifold. Before the start of the test phase all flow rates were compared to the pump frequencies, guaranteeing the right flow rate for the three different setting of the flow rate, namely 80, 100 and 120 L/min.

Overflow

At the top of the soil container, an overflow system was designed to expel excess water during jetting and fluidisation. This system comprises a lowered side at the container's top, equipped with three tubes that channel the water back into the water reservoir or drainage. Before the water enters these tubes, it passes through the geotextile filter capable of trapping soil particles while allowing water to flow through. This setup ensures no loss of soil particles during testing, maintaining the sand mass within the soil container consistent across multiple experiments. To prevent sand accumulation and maintain permeability, the geotextile at the top of the container was cleaned after every test.

The geotextile should be permeable enough to let the 500 l/min flow rate go through it without the soil container overflowing. For geotextile, the permittivity is the rate at which the water can pass through the material, which is dependent on the area of the geotextile and the hydraulic head. With a permittivity of around 1 s^{-1}, a height of the geotextile of 0.3 m, and a width of 2 m, this comes up to around 1000 to 2000 m^3 l/min, depending on the distance to the top that is used.

$$\psi = \frac{\text{Flow rate (Q)}}{\text{Area}_{geotextile}(A) \cdot \text{Hydraulic head}(\Delta h)} \tag{3.3}$$

Seepage

To regulate the hydraulic gradient across the outlet of the water compartment, simulating the level of seepage influenced by the increased pressure in the soil column outside the monopile, a Seepage Control System is implemented. This system comprises simple and standard modular PVC-pipe plug-in segments, equipped with an overflow that leads to either a buffer soil container or a disposal gutter. By doing so, the hydraulic back-pressure can be controlled in increments of ΔH_s=0.25 m, with a total range of H_s within 0.0 to 2.5 m. When the range is at 2.5 m there will only be seepage due to the extra pressure generated by the jet. When the seepage flow is at its lowest setting the head difference will be 2.5 meters which will cause constant seepage through the permeable soil. The seepage flow rate (Q_s) was measured using a flow meter in the seepage loop, shown in Figure 3.7.

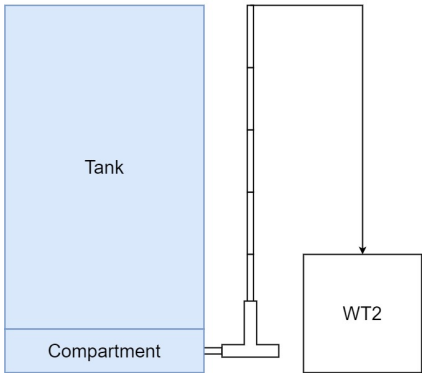

Figure 3.8: Seepage Control System for controlling the hydraulic head

3.3. The test matrix: selection of installation settings

This study aims to provide a comprehensive analysis of the parameters affecting the displacement of the soil plug during jetting operations. Ideally, conducting a wide array of tests would yield the most complete dataset. However, the time required for both test execution and subsequent data processing is uncertain. Consequently, a test matrix has been constructed to delineate the various testing options. Table 3.3 comprises three columns: 'Optimal' enumerates all potential testing options; 'Moderate' details the settings actually employed in the tests; and 'Minimal' describes the least number of tests necessary to ensure a robust study of plug displacement. The importance of different installation settings is evaluated, with a justification for the selection of those settings that are anticipated to yield the most significant insights.

- Sand type: In the North Sea, there are multiple soil types and particle sizes. To replicate these conditions, three different sand types with varying D_{50} values have been selected for the tests.

Particle size influences every aspect of the plug surface velocity, namely erosion, breaching, and sedimentation processes. This is due to several parameters that depend on particle size, including the particle Reynolds number, sedimentation velocity, and porosity.

- Penetration rate: The penetration rate measures the installation speed when installing a monopile and is replicated in the soil container as the vertical downward velocity of the jet. During Vibrohammer installations average penetration velocities are 10 mm/s and onshore tests by GBM Works resulted in a maximum of 4x faster penetration velocity (GBMWorks, 2020). This resulted in the selection of penetration velocities from 10 to 40 mm/s. It is expected that the penetration rate influences the slope angle of the soil plug because the soil plug has less time to reach a stable slope.
- Flow rate: This is the volume of water ejected from the jet when using the Vibrojet®. It depends on the required fluidisation to reduce the internal friction between the sand and the monopile. Previous research by GBM has shown that the flow rate affects the flow velocities and concentrations inside the soil container, as well as the size of the fluidised area. The influence of flow velocity on the plug surface should be apparent.
- Relative density: In the North Sea, soil relative density varies by location and depth but reaches from medium dense to very dense soil. (Biryaltseva et al., 2016). To simulate these variations, the sand is vibrated with a vibratory hammer, increasing its relative density over time. The relative density has a complex influence on the behaviour of processes inside the monopile. A higher relative density corresponds to a lower initial porosity, which decreases permeability and thus the plug displacement according to the theory. Though, it also decreases the seepage flow which should increase the stability of the soil plug.
- Head difference: Excess pressure inside the pile during offshore jetting installations can cause water to flow around the pile's underside. This excess pressure gets higher and higher when the monopile penetrates deeper into the soil, due to the increased density of the SW-mixture. To imitate this increased pressure, the head difference is changed to simulate a stronger flow. It is worth noting that such seepage can enhance superficial flow velocity, which could stabilise the plug, as discussed in section 2.2.6.

Installation settings	**Optimal**	**Moderate**	**Minimal**
Sand type: 153, 337, 620 [μm]	Fine, medium, coarse	Medium	Medium
Flow rate [m^3/s]	80 - 100 - 120	80 - 100 - 120	80 - 100 - 120
Relative density [-]	50 - 75 - 100	50 - 75 - 100	50 - 75 - 100
Penetration rate [mm/s]	10 - 20 - 40	10 - 20 - 40	10
Head difference [m]	0 - 1.49 - 2.50	0 - 1.49 - 2.50	2.50

Table 3.3: Test matrix of optimal, moderate and minimal test settings

The 'Optimal' column contains all tests that could be executed with the current lab test setup. It also contains changing the sand type which is a very time consuming step, because the whole soil container should be pumped empty and vacuumed till no sand is left. Then the new sand needs to be measured and put into the soil container. The 'Moderate' column includes all tests with only the medium sand type. This could be done with a minimum of ten tests because multiple tests overlap. With this configuration the most important aspects of the sensitivity analysis can be validated and the effect of seepage and penetration rate was added. The last setting 'Minimal' includes only the change in flow rate and relative density. With this configuration the most important aspects of the sensitivity analysis can be validated since the slope angles, flow velocity, concentration porosity, and pressure will still change. Although, this limits the research on the seepage effect and different penetration rates. Eventually, the 'Moderate' was chosen because it gives a comprehensive analysis and it could be done in the during the period of this research.

4

Visualisation of lab test results: from measurements to data

This chapter discusses how to measure the needed parameters accurately during lab tests. It explains the process of calibrating and validating sensors inside a soil container, which is essential for reliable results. Furthermore, the visual software is described for measuring the plug surface displacement and particle velocities, which are key for improving prediction models. This part highlights the importance of accurate measurements to better understand how the system behaves and to make models more accurate. This chapter answers the following research questions for both the sensors and the visual software:

- Which methods can be used to measure the needed parameters during the lab tests?
- How can the accuracy of the measurements be optimised?

4.1. Sensors: calibration and validation

In this section the calibration of the sensors used in the soil container is explained, which are mentioned in Paragraph 3.1. Each pore pressure and total pressure sensor is checked hydrostatically to ensure their correct functioning. Between each changeover of sand type in the test program, all calibrations are checked to ensure that calibrations have not drifted and the sensors have not been damaged or clogged during the previous round of testing.

Pressure sensors

Calibration of the pressure sensors was done by measuring the pressure of the sensors and then applying the subsequent Equation 4.1.

$$\text{Pressure [kPa]} = \text{Measured value} * 10^6\text{[-]} * \text{Calibration Coefficient [kPa /}1 * 10^6] \tag{4.1}$$

The accuracy of the sensors was first validated by using the measurements of the absolute and PWP sensors in the water compartment beneath the soil container. The value of both sensors should be the same for every test but it seems that the sensors have an offset that is different every test, as depicted in Figure 4.1. Although, both sensors independently track the same changes in pressure with a high degree of accuracy, which is illustrated in 4.2.

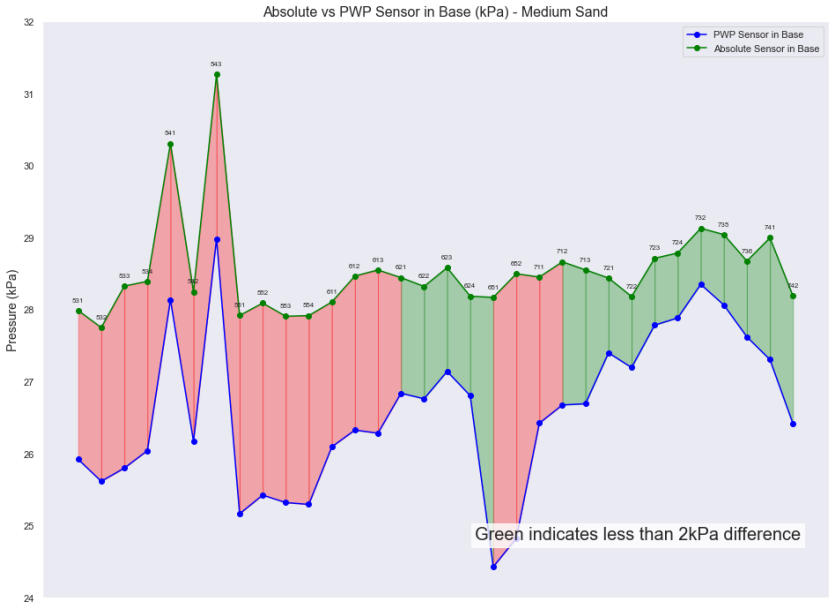

Figure 4.1: Absolute vs. pore water pressure sensors average in test sequence

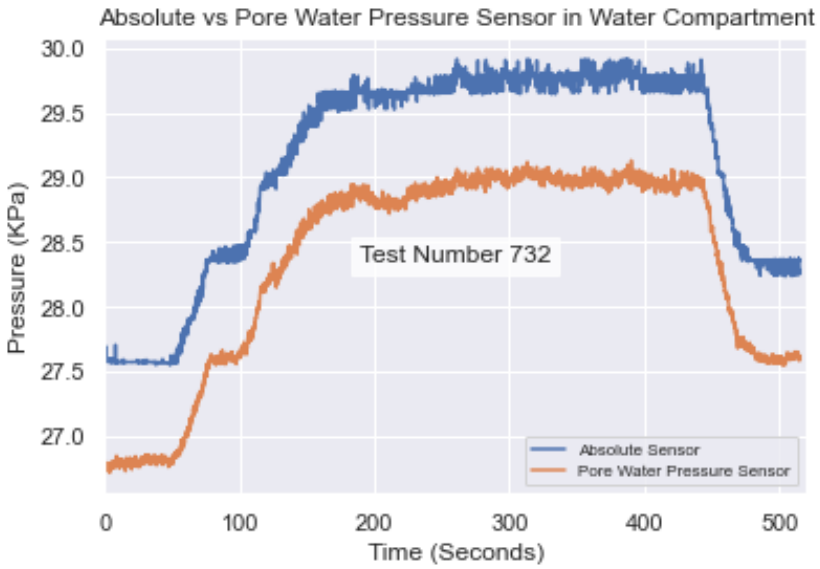

Figure 4.2: Comparison of the absolute and PWP sensor during full test (test 732)

Therefore, the relative pressure for each sensor was calculated by subtracting the initial (hydrostatic) value from all subsequent values, as illustrated in Figure 4.3, to enhance visualisation and analysis. This approach ensured that the pressures presented were the measured over-pressures.

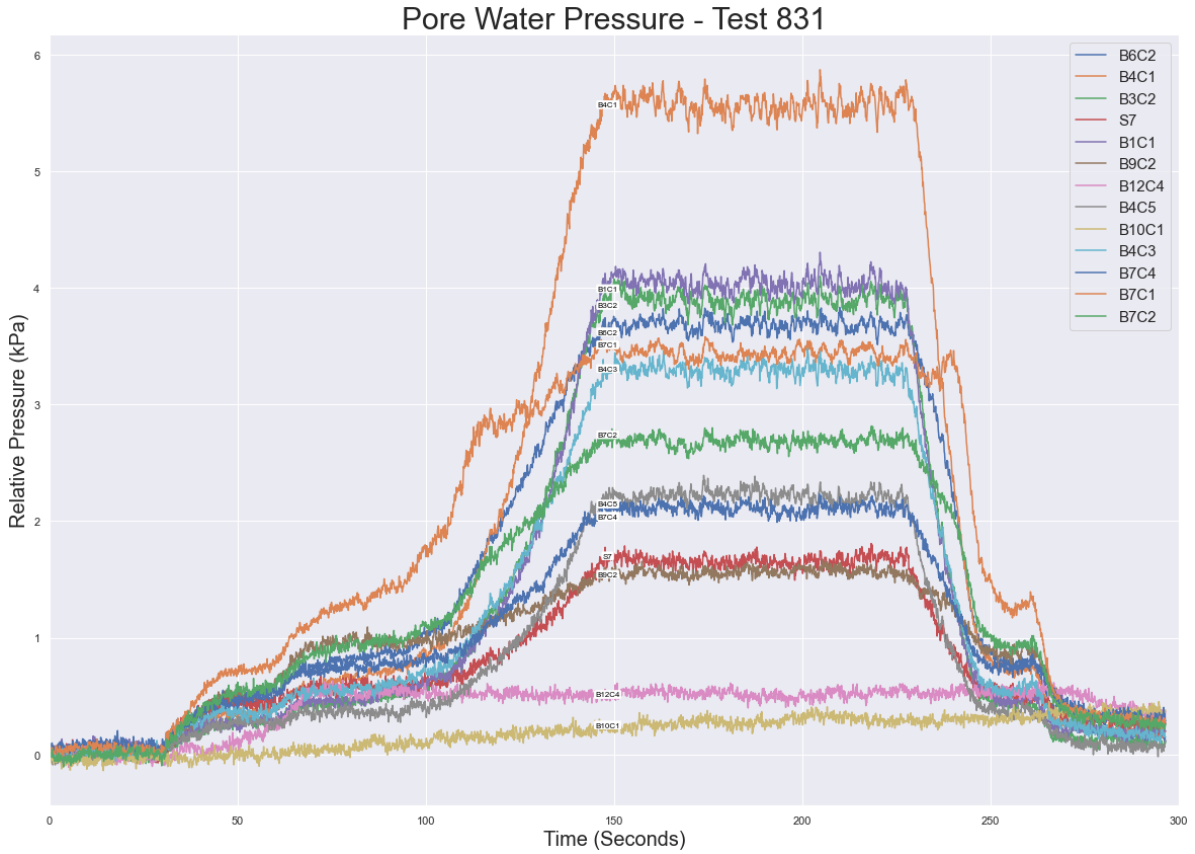

Figure 4.3: PWP sensors alongside jet position (test 831)

The smoothing technique employed for the pressure sensors was the Exponential Moving Average (EMA). EMA was chosen because it assigns more weight to recent data points which makes it faster then other signal processing methods according to a comparison study by Lotysh et al., 2023. Therefore, it is particularly valuable for applications where timely updates are crucial, such as the sensors data in this study. The span for calculating the EMA was specified and experimented with to identify the optimal fit for the dataset. Special attention was given to avoid over-smoothing the data, as this could introduce lag and shift measurements ahead in time. The impact of applying EMA to smooth the raw data is demonstrated in Appendix A.2, where the span was adjusted to 10 and 100 for comparison, showcasing the technique's effect on data representation. A span of 100 was chosen for this study.

The PWP sensors allow for calculation of the concentration in the soil container in the fluidised zone, by using the Bernoulli Equation 3.1. At the beginning of each test the PWP sensors are only subjected to hydrostatic pressure from the water above. When the jet starts fluidising the sand the density of the mixture that exerts the force on the pressure The velocity elements in the equation can be neglected due to the relatively low flow velocity in the soil container, which influence the final concentration by less than one percent. Using the relative values of two pore pressure sensors on different heights, depicted in 4.4, the concentration can be estimated. The relative pressure is the value of the PWP sensor subtracted by the starting pressure at the beginning of a test and is represented by δp_1 and δp_2 in Equation 4.2 and 4.3.

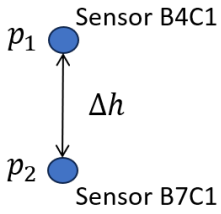

Figure 4.4: Pressure difference and height between the two sensors used for calculating the average concentration

$$\rho_m = \frac{(\delta p_2 - \delta p_1) + \rho_w g \Delta h}{\rho_w \Delta h} \tag{4.2}$$

$$c = \frac{\rho_m - \rho_w}{\rho_s - \rho_w} \tag{4.3}$$

The final concentrations, which will be presented in the next chapter, remained consistent across all tests after achieving complete fluidisation at both sensor locations. This consistency serves as validation for the accuracy of the method employed.

Temperature sensor

Temperature monitoring throughout the test series is conducted using a temperature probe within the soil container. Initially, the temperature is assessed during each test to determine if the pump activity causes any significant heating of the water, which could result in decreased water viscosity and thereby affect flow processes. Additionally, the water temperature in the soil container is monitored over the entire series of tests to make sure the lab conditions did not have significant influence.

Regarding the initial point of investigation, no noticeable temperature increases were observed in the soil container during the tests. Examples of temperature readings throughout the tests are illustrated in Figure 4.5. The temperature of the water in the soil container throughout the entire test sequence ranges between 14 and 16 degrees Celsius. These temperature variations have a negligible impact on the test program as they have only a minor effect on water density and viscosity. Temperatures for the whole test sequence are depicted in Appendix A.7.

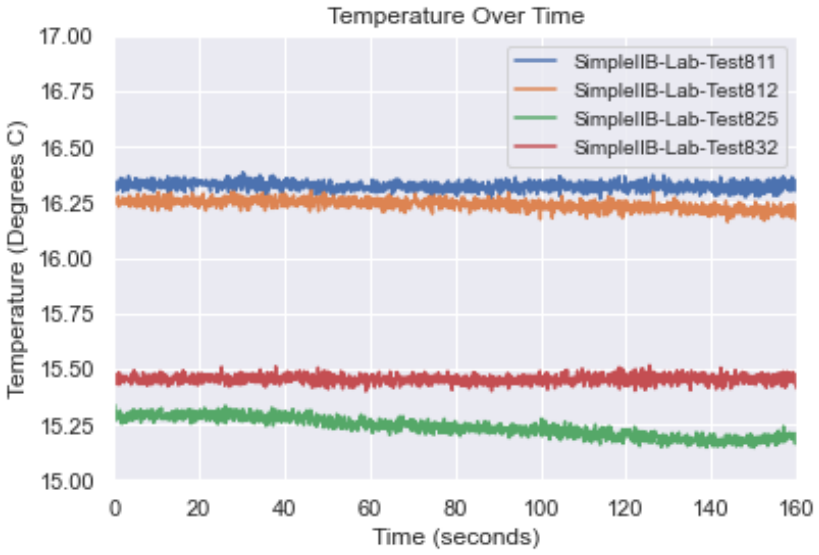

Figure 4.5: Temperature sensor during different tests

4.2. Visual software: from videos to data

In the laboratory tests, tracking the interfaces between fluidised and solid zones, along with the velocities of particles moving within the soil container, proves to be excessively laborious. Furthermore, the

visibility of the jet manifold is significantly reduced during tests due to the high concentrations of sand in the fluidised zone. In order to use the test information for a sensibility analysis the transformation from camera images and sensor information to workable data was needed.

Therefore, a software algorithm was developed to identify UV particles using visual techniques. This software is used to compute the necessary parameters during the lab tests: the average flow velocity over the flow layer thickness, the shape of the soil plug, the angle of the slope, and the plug surface velocity. Also, additional parameters such as absolute pressure and pore pressure will be extracted to review their influence on the plug surface velocity. These parameters are illustrated in Chapter 2 in Figure 2.7.

To determine these parameters, multiple methodologies will be explored, and the justification for choosing the final approach will be provided. Selection among various methods will be based on the precision of the results and the speed of computation. Achieving highly accurate results is essential for the success of the sensitivity analysis. Additionally, GBM Works plans to perform close to a hundred tests, further emphasising the importance of code efficiency. This need is underscored by the fact that camera images generate 4 gigabytes of data per minute.

The script predominantly uses standard Python utility modules such as pandas, numpy, os, matplotlib, and sys, which will not be extensively described in the software documentation. The focus will instead be on elaborating other imported modules that are essential for the analysis, to ensure a clear understanding of their functionality within the software.

4.2.1. General processes

The transition from laboratory tests to results is illustrated in Figure 4.6. The process begins with the Inbox phase, incorporating all test videos and sensor data. Following this, the data processing stage involves adjustments to make the data amenable for image analysis. These adjustments include converting images to accurate positions and displacements and refining the images by eliminating reflections and adjusting brightness levels. Once these modifications are complete, the images undergo analysis, which entails identifying particles, monitoring their movements, and converting these observations into precise plug surface positions and velocities. The last step of this process is the transformation of these findings into comma-separated values (CSV) files and graphs, which are essential for the sensitivity analysis and constituting the final results.

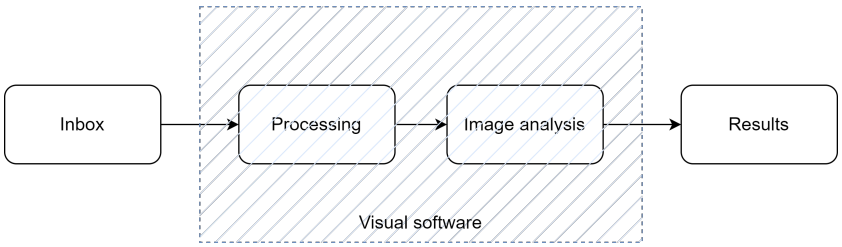

Figure 4.6: General processes visual software

4.2.2. Image processing

Before the particles can be tracked, the frames of the video have to be processed in such a way that they are suitable to perform the particle tracking (see next section on image analysis). To read and process the frames, there has been made use of the video analysis python module 'Open CV – cv2 – version 4.8.0'. The steps that have been performed on each of the frames are illustrated in Figure 4.7.

These steps start with creating undistortion matrix for the camera to correct the curved video. This is important because the lens of the camera is convex. Then, the image had been turned into grey-scale, warped, re-scaled and rotated based on the found markers in the image. All of this was done to accurately link the distances in the image to real world distances in the soil container. Then, the image was filtered based on intensity thresholds and the reflections were masked out. This process was done every image to finally create all frames for the image analysis.

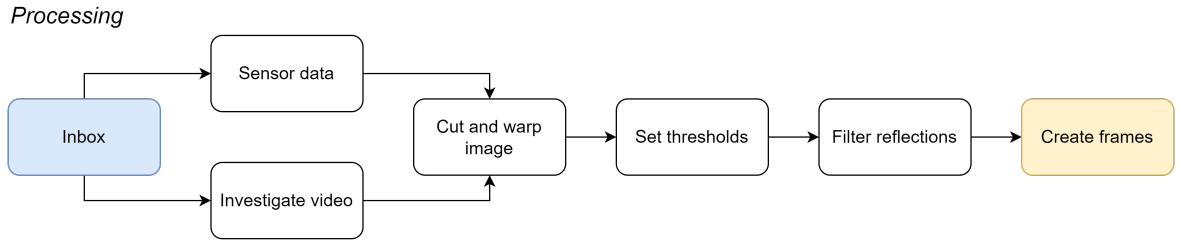

Figure 4.7: Step-by-step processing

Correction of the camera convex

Because a lens of a camera is convex, physical straight objects will appear slightly curved on video. If very apparent this is called the 'fish eye effect'. To account for this a camera calibration has been performed, where several short movies were shot in which a chequerboard was held behind and against the Plexiglas wall of the soil container. Of each of these short movies, a single frame was selected. In total 9 chequerboard positions were used to calibrate the camera, one is shown in Figure 4.8. On the 9 images in the figure the rainbow coloured lines represent the found chequerboard corners, for which is known the corners should be exactly straight. Based on this information an undistortion matrix was created using the OpenCV module in python. This was done only once and then applied to all video's, and therefore the position of the camera may not be moved afterwards.

Because the soil container was higher than it was wide, the camera was filming in a laying position. The figures in this section are displayed as they appear during processing, which means they are shown in landscape orientation before any rotation and in portrait orientation if rotation was applied during processing. All images are resized here for reporting purposes, so there is loss of detail with respect to the actual images.

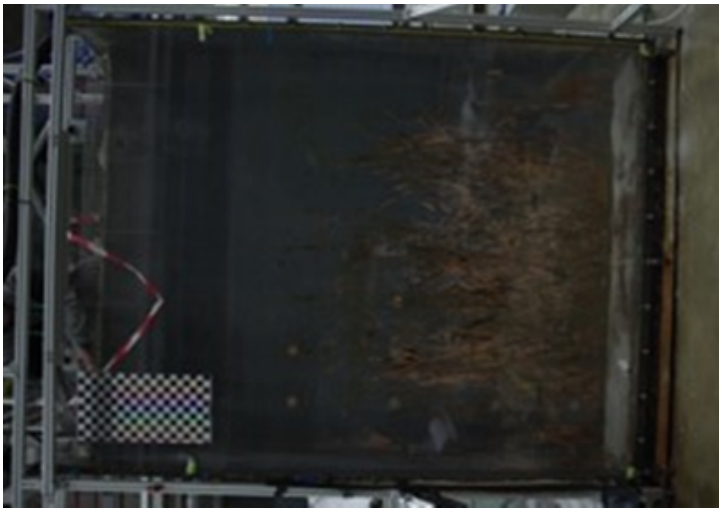

Figure 4.8: Chequerboard behind Plexiglas for computing the distortion matrix

An example is shown in Figure 4.9 on a single frame of one of the calibration movies. The steel side of the soil container is physically straight. In the raw image (top) you can see however, that the side of the soil container curves and deviates from the straight red line ('fish eye effect'). In the undistorted Figure 4.10, the side of the soil container is perfectly parallel to the straight red line. This means that physical straight lines are now also straight in the image and thus the undistortion works.

Figure 4.9: Original image of the side of the soil container

Figure 4.10: Undistorted image of the side of the soil container

Find markers to cut out the relevant frame

On the soil container four UV reflecting yellow markers were placed to mark the area of interest for the test. The undistorted tenth frame of each of the video's is used for finding the markers. Based on light intensity the image was scanned and all spots found that are larger than 100 pixels, i.e. far larger than the sand particles, are marked with green boxes. Based on yellow colour and size, the four markers are selected and marked with (small) red boxes. The position of the outer corners of the markers was used to cut out the relevant frames for the test. Also, it reduced the computing time used for processing. Appendix A.2 shows a picture of the frame with recognised sensors.

Set thresholds to filter intensity

In Figure 4.3 you cannot see the UV coated sand particles reflecting the UV light. This has to do with the intensity of the reflection, which is fairly low because the particles are really small (<1 mm) compared to the video area (over 3x2m2 on 8K frames). Therefore, the area of interest within the video for the frame of the latest lowest position of the manifold, is filtered based on intensity of the reflection, where everything above a certain intensity threshold is made white and the rest of the image is made black. This makes the particles "pop-out", an example is shown in Figure 4.12. Because the UV lights are not spreading an even amount of light over the soil container, the image is split into four sections by three Height sliders with which the heights of these divisions can be set manually. Then for each of these four sections the intensity threshold (Threshold 1 to 4) can be set to show more or less particles, as depicted in Figure 4.11.

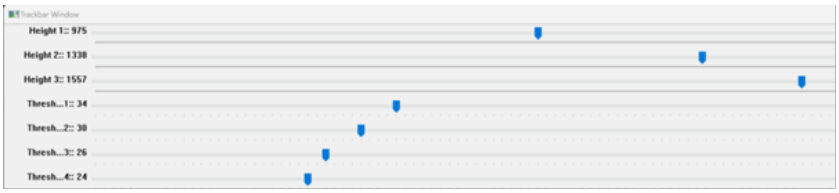

Figure 4.11: Threshold sliders for adapting the right settings

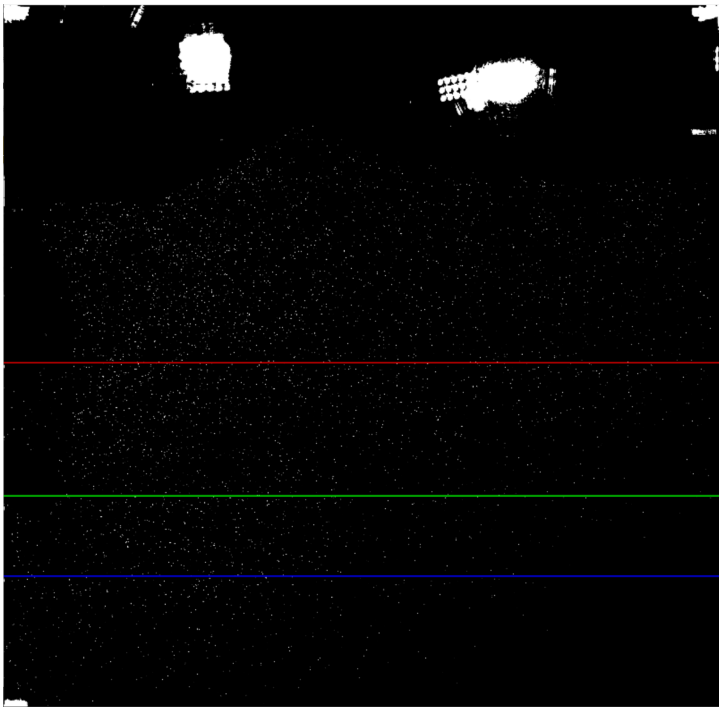

Figure 4.12: Image of the threshold heights to filter on intensity

Process images

Undistortion is applied as very first step to the raw image in order to take into account the camera distortion ('fish eye effect') and the refraction of the Plexiglas wall. After undistortion, straight lines appear straight in the image and black curves are found on the edge of the image to fill up the image. Next, the original frame was changed to a grey scale image in order to apply the filtering on light intensity in a later step. Then, the images were cut and resized so that the pixels are equal to one millimetre in reality and everything outside the markers in not shown anymore. The images are also rotated so that they are back in their real orientation.

If a video is shot with low amount of light, the resulting frames have a lot of noise. To mute this noise a very small Gaussian blur with a standard deviation of 1 was applied to the image. This is very hard to see on the large pixel image by naked eye, therefore the result looks the same as Figure 4.12 and is therefore not shown here in the report.

Next, the image was filtered based on the thresholds that were selected earlier, making everything above the threshold pure white and below the threshold pure black. Now, the UV coated particles are showing in the image, which can be seen in Figure 4.13.

Finally, the markers, UV lights and in some tests some big reflections of sunlight are still showing white in the image. Since they should not be recognised as particles while particle tracking, a mask was created to filter them out. This was done based on size, so that everything larger than larger than a sand grain (5x5 pixels) was recognised as reflection. The result can be found in Figure 4.14 and shows the fully processed image, ready for particle tracking analysis.

Figure 4.13: Resulting frame before filtering reflections

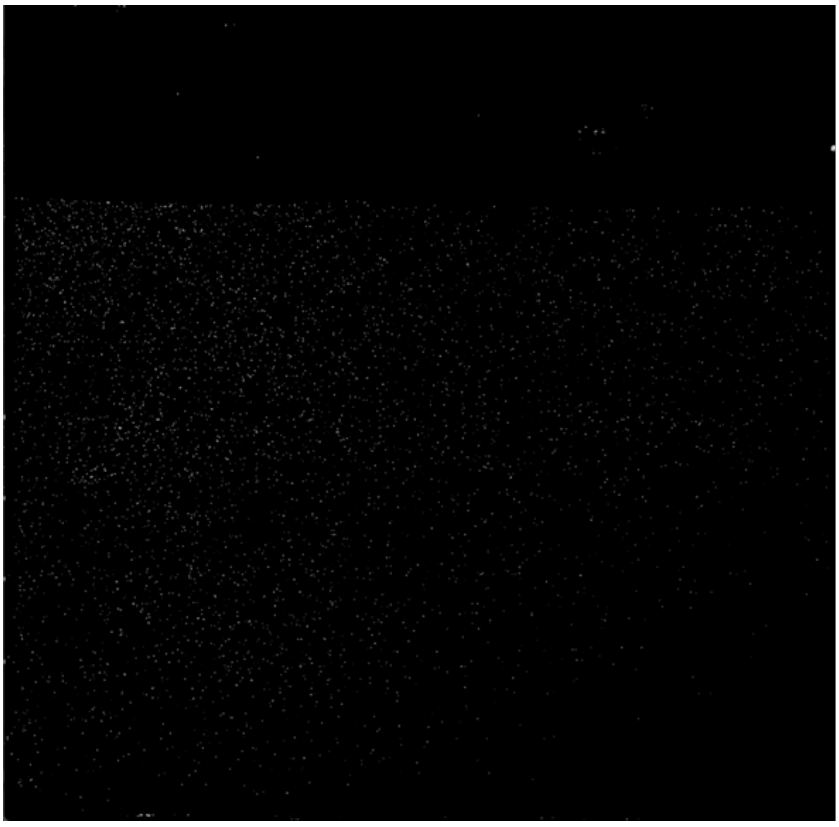

Figure 4.14: Final frame after the create frames function

4.2.3. Image analysis

The image analysis is needed to go from processed frames as output of the image processing to usable results, illustrated in Figure 4.15. This phase starts with the tracking of particles over the frames and the computation of various parameters. Following this phase, the analysis progresses to the calculation of particle velocity. Subsequently, the process continues identifying the maxima, meaning the boundary particles of the defined moving and static zones, which provides insight into the shape of the plug surface. These maxima are then fitted by polynomial functions to reconstruct the plug surface as accurately as possible. The final stage is the calculation of plug surface velocity by using trigonometric identities. These steps are further detailed in the following sections.

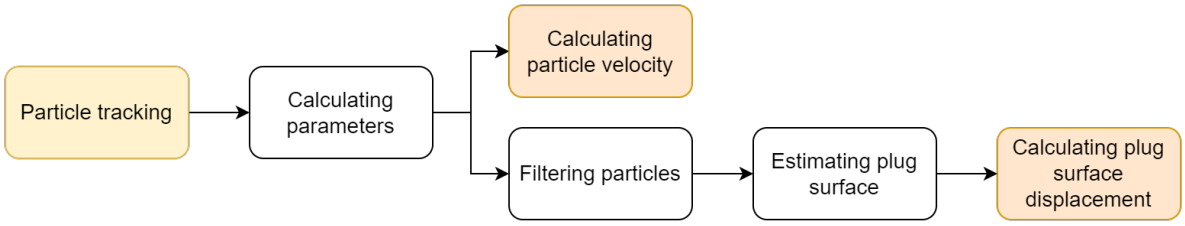

Figure 4.15: Step-by-step image analysis

Tracking particles over multiple frames

For particle tracking two methods were tested: using low shutter speed camera settings and particle tracking using the python module 'Trackpy'. Utilising a low shutter speed captures an image where the particle's movement is recorded over a brief certain duration. This approach allows for the calculation of particle velocity by dividing the length of the particle trail on that single image by the elapsed time. Moreover, this method is substantially quicker than the Trackpy method as it requires only one image to analyse particle velocity. However, there are two significant drawbacks: overlapping particles can skew the velocity measurements, and the particle width in the image varies with the intensity of the UV light, resulting in potential errors in velocity estimation.

It was therefore chosen to use the Python Trackpy module, which facilitates the precise identification and tracking of particles across sequential frames but acquires much a lot more processing power since a high frame rate is needed. This enables the calculation of particle velocities, movement direction, and offers multiple filtering options. The Trackpy module's 'batch' and 'link' functions have been used in this script. 'Batch' identifies and locates particles frame by frame. It filters a frame to identify particles by size and brightness, creating a list with each particle's index and coordinates. 'Link' connects these identified particles across frames to track their trajectories. It takes the lists of detected features for every frame and tracks each particle's journey through the frame sequence. The results are stored in a CSV file used for further analysis which contains around 75.000 particles per second.

The following arguments were set manually (in the administration file where the test ID, markers and other thresholds are also stored) per video in order to get the best result:

- 'min-size' sets the minimum particle size in pixels for 'batch';
- 'min-mass' defines the brightness threshold in 'batch' to filter out minor reflections that are not actual particles;
- 'search-range' sets the maximum distance a particle can move between frames to be considered the same particle for 'link'. Setting this value too high resulted in linking unrelated particles. For example, when a particle goes out of frame and another particle appears, they could be linked together as one particle.
- 'memory' comes into play within 'link' when particles vanish for a few frames, allowing the algorithm to 'remember' and re-link a particle that reappears, thereby maintaining the integrity of the particle's trajectory.

The decision was made to analyse particle movement every thirty frames, equivalent to one second, ensuring comprehensive tracking. This frequency allows the 'link' function sufficient data to accurately connect particle trajectories, enhancing the analysis of flow paths and velocities. Consequently, the results obtained have a one-second frequency, considered sufficient for this study. Figure 4.16 illustrates the trajectories of recognised particles over a one-second interval (30 frames).

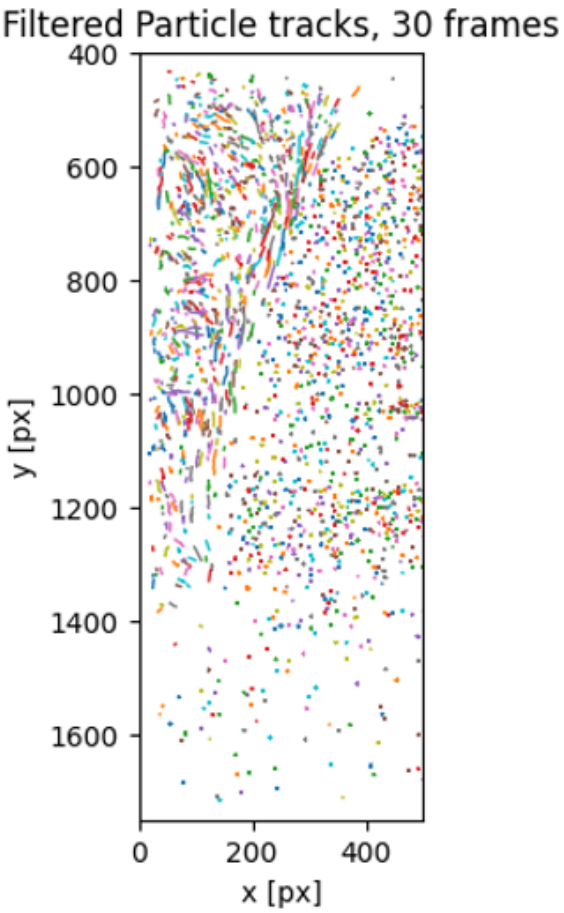

Figure 4.16: Particle tracks during one second with the jet in its lowest position (Test 533)

Calculation of particle parameters

When the CSV file with all tracked particles during the last 30 frames has been made, several parameters are added in order to calculate the velocity of particles and the local maxima. Every particle contains a position of every frames it was tracked. From there, the total displacement was determined using the Pythagorean theorem, and the angle of movement was calculated using the inverse tangent function on the y and x displacement per particle. Additionally, the script evaluates the relative displacement of particles from their initial positions to their current ones, providing insight into the overall movement path throughout the sequence of frames. A counter was also incorporated to keep track of the frame number.

Filter moving and stationary particles

The next steps for calculating the particle interface velocity involve filtering out the stationary and moving particles, calculating the local maxima, and estimating the polynomials.

The process of filtering particles was divided into two parts: filtering the stationary particles and the moving particles. This division was necessary due to several challenges encountered during the development of the visual software. After the fluidisation loop, a layer devoid of UV particles appeared on top of the sand bed. This occurred because the non-UV particles have a wider size range compared to the UV particles, resulting in a fine layer of non-UV sand particles remaining on top of the bed. However, once the particles were fluidised again by the jet, the non-UV and UV particles mixed effectively. As a result, the moving particles were filtered.

The moving particles located below the jet at the bottom of the trench have very high velocities and a lower concentration due to the jet water. These factors make the particles difficult to capture on camera at the bottom of the trench. Moreover, the area between the plug surface and the water is not visible when only the moving particles are filtered out, as this only reveals the interface of the stationary and

fluidised particles. Therefore, to visualise the entire soil plug, it is necessary to filter out the stationary particles.

In conclusion, analysing both the moving and stationary particles generates two lines, providing a basis for comparison and thereby yielding a more accurate result of the plug surface. The results of filtering out the moving and stationary particles are illustrated by the blue and red dots in Figure 4.17.

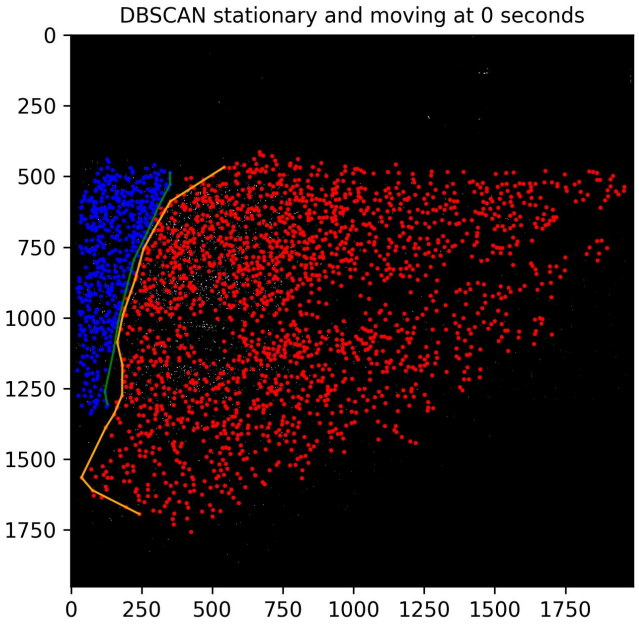

Figure 4.17: Filtered stationary particles and perimeter in blue and moving particles in red with an orange line (Test 533)

The stationary particles were filtered using two criteria:

- No displacement – This criterion filters out all particles that are moving, i.e., the particles with a displacement of 0.
- X consecutive frames – This criterion ensures that the particles are present for at least a certain number of consecutive frames. It helps filter out most small reflections that have not been filtered out during particle tracking. It also filters out particles that appear to be stationary in the fluidised area but are actually between two flow directions or pushed against the glass.

Moving particles were filtered using only the relative displacement criterion:

- Minimum relative displacement – This is the displacement of a particle relative to the first time the particle is spotted. If this displacement does not exceed a certain value, the particle will be deleted.

After the initial filtering, particles are scanned for density using Density-based Spatial Clustering of Applications with Noise (DBSCAN), which filters out particles based on the number of particles in a given range around the particle. This method allows for filtering out the last particles that are not in the correct region. A study by Alahmari et al., 2021 compares several common density-based clustering algorithms and concludes that DBSCAN is the preferred choice for this application. This method introduces two additional criteria for both stationary and moving particles:

- Minimum amount of particles found
- Range around a particle where the amount of particles are counted

The visual code is designed so that all criteria can be modified in an admin file. This allows for the iterative refinement of the filtering process to achieve the best result. Additionally, the analysis can be performed over a few seconds of frames, which reduces the time required for the iteration.

Selection of the points on the plug surface

The methodology for defining the plug surface using stationary particles involves identifying the highest value along the x-axis across various bins. Calculating the highest x value of the moving particles creates an array of points along the border of the fluidised zone. This method was done for both fluidised and stationary particles, and the x and y axis were separated into bins. The decision on the number of bins to divide the axis into was reached through iterative testing. Utilising bigger bins results in fewer points defining the plug surface but ensures a smoother transition between these points, minimising fluctuations. Conversely, smaller bins produces a more detailed interface with numerous points, though this can lead to significant variability in the interface's outline. The method is illustrated in Figure 4.18 where multiple lines are visible, the horizontal green lines are the bins and the orange line was drawn between the maxima of stationary particles of the horizontal bins. The yellow line was drawn between the maxima of the stationary particles of the vertical bins that have not been included in this figure.

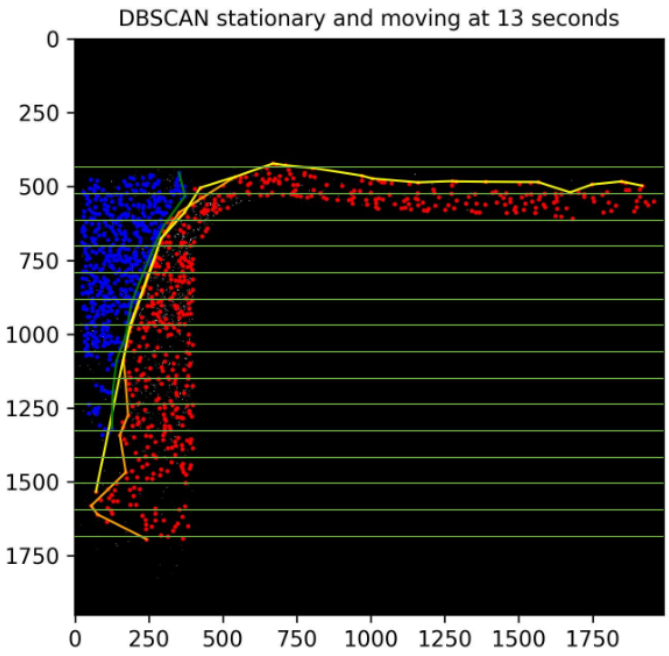

Figure 4.18: Filtered moving (blue) and stationary (red) particles and horizontal green lines representing the bins (Test 532)

As previously discussed in the "Particle Filtering" section, the distinction between stationary and moving particles yields different plug surface representations. Consequently, calculations were performed for both particle filtering methods to account for a full representation of the plug surface. Note that for the stationary particles the minima were calculated instead of the maxima. Also, there is a difference between horizontal bins and vertical bins, since the horizontal bins can more accurately determine the steep slope angle and the vertical bins more accurately represent the gentle slopes.

The vertical bin results of the stationary particles (yellow line) were used to narrow down the area of analysis. Since the right bottom part in soil container contains no useful information, this was blacked out to reduce the software run time. All pixels on the right of x = 400 and not within 100 pixels around the yellow line were blacked out, which can clearly be seen when Figure 4.17 and 4.18 are compared. This reduced the average amount of particles per frame from 2500 to 1000 particles.

Estimation of the plug surface shape using polynomials

Using the point of the particle interface that have been calculated using the maxima in the bins, several order polynomial fits were done to minimise the difference between the estimated curve and the particle interface. Ideally, the selected order of the polynomial minimises the difference between the estimated curve and the actual data points. Unfortunately, this causes defaulting to the highest possible polynomial order, which would in turn not accurately reflect the plug surface, as illustrated in Figure 4.19. The

figure depicts seven degrees of polynomials based on the maxima found in the previous paragraph. To select the most accurate representation of the the plug surface, the polynomials were compared in three different tests to the point calculated in the maxima. This resulted in selecting the forth degree polynomial as the best fit.

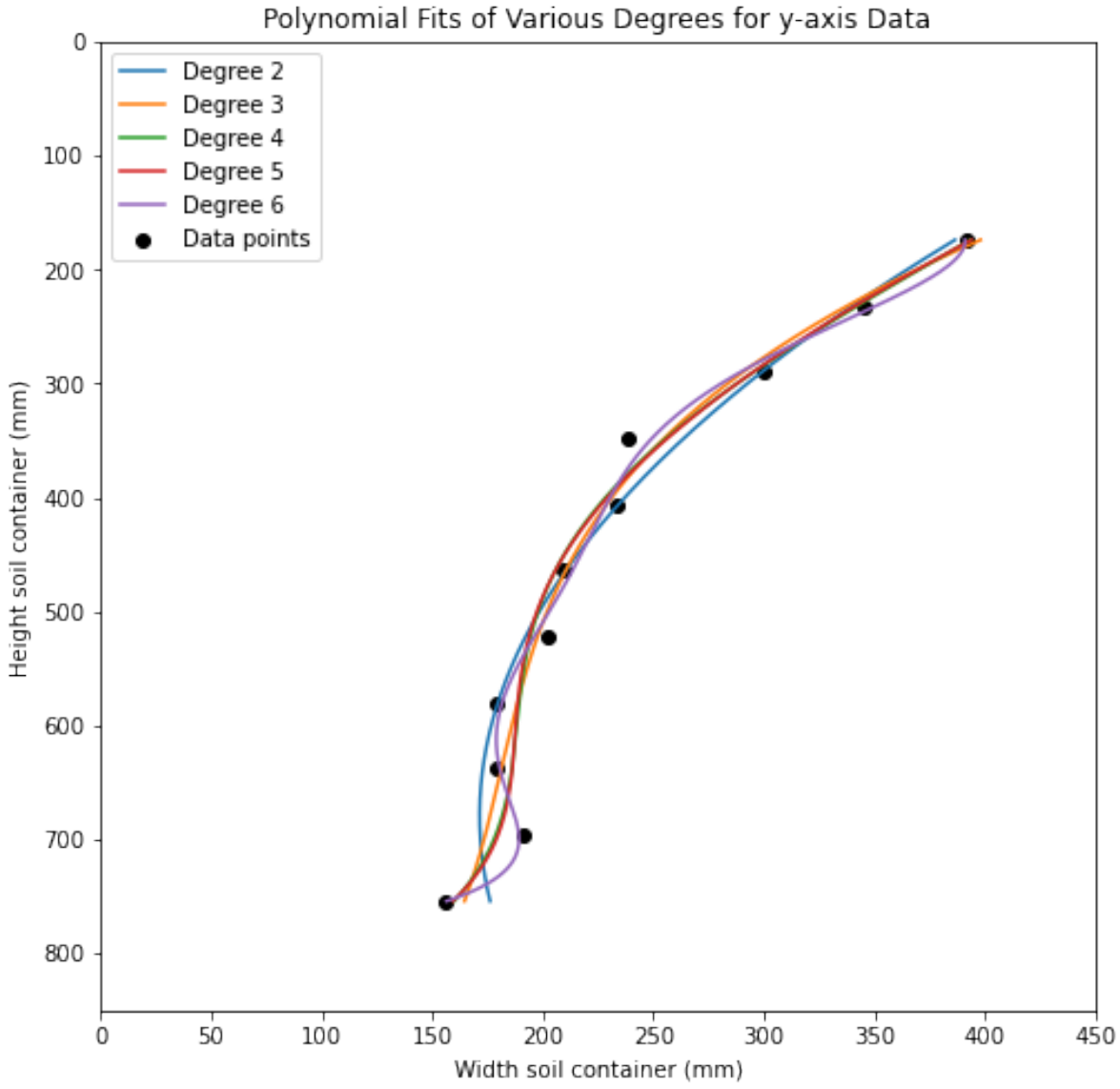

Figure 4.19: Polynomial fits from first to the seventh degree

From this shape, the horizontal position (or trench width), which is the distance from the left side of the soil container to the plug surface at a certain height, can be calculated through interpolation of the resulting polynomial. Similarly, the slope angle of the plug surface can be determined by taking the derivative and performing interpolation thereafter. These results are then used to plot the trench width and horizontal position over time, at one-second intervals, offering insight into the plug development during jetting.

Calculation of the plug surface velocity

The slope's angle was determined through interpolation, which was used as an input for sensitivity analysis and calculations involving perpendicular displacement of the plug surface. The process for calculating the displacement involves calculating the slope of the interface, determining a perpendicular line through a corresponding point on the initial polynomial, and then finding the intersection point

with a second polynomial. The perpendicular plug surface displacement is finally calculated using the Pythagorean theorem to measure the distance between these two points. This process is illustrated in Figure 4.20, showing two polynomials: one representing the initial moment and the other a second later, with a perpendicular line connecting the two polynomials. The figure is rotated ninety degrees counterclockwise due to the method of fitting the polynomials. The vertical axis depicts the trench width (or horizontal position) and the horizontal axis depicts the height in the soil container. Thus, the part under the graph is the fluidised zone during testing and top of the polynomial is increasing in trench width.

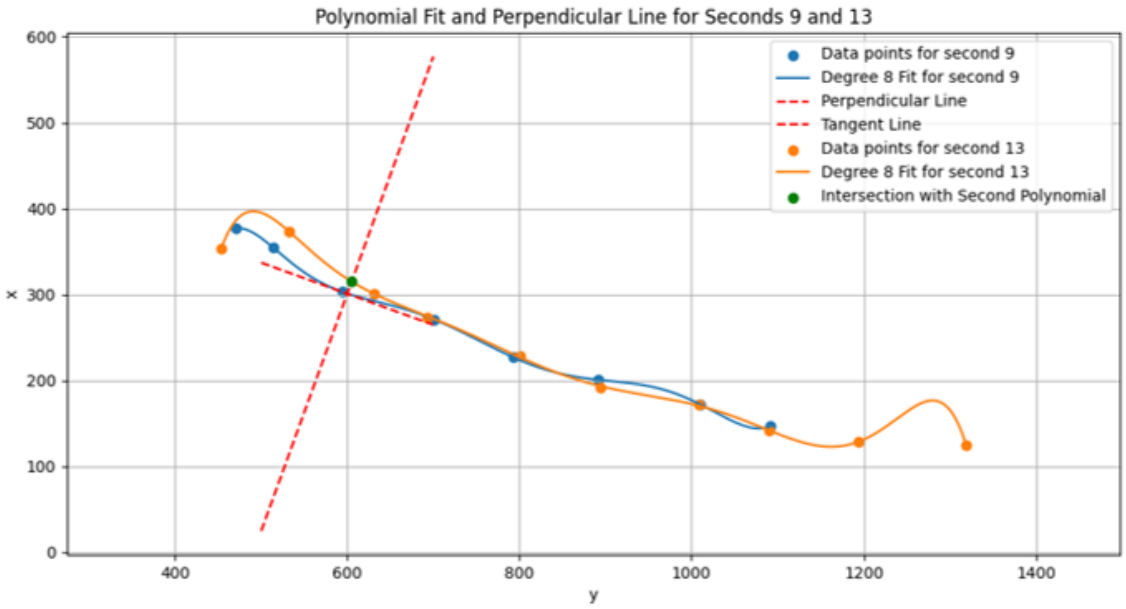

Figure 4.20: Displacement calculation perpendicular to the first line and intercepting the second line (Test 612)

If the polynomial fits are not accurate enough, the method mentioned earlier might result in unstable results. Another method involves using the change in horizontal displacement and the slope angle. This approach plots the trench width over time at a certain height in the soil container to track its movement over time (Δw_t). By using the slope angle and the time that has passed, velocity can be calculated with the equation shown in Figure 4.21. However, this method lacks accuracy because it doesn't take into account the curvature of the plug's surface shape.

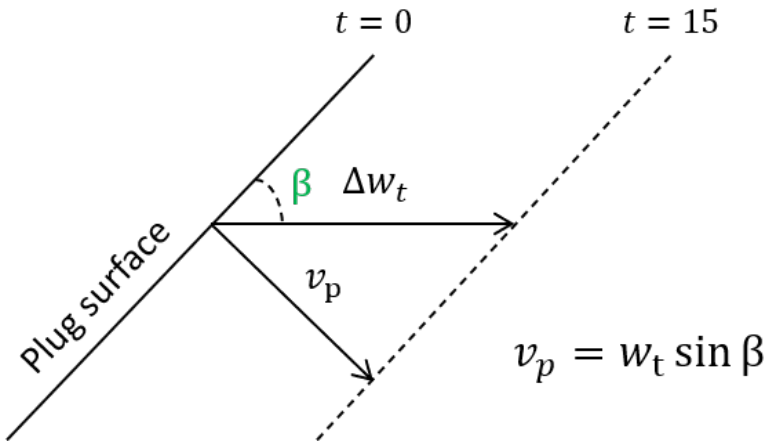

Figure 4.21: Method for calculating the plug surface velocity

Estimation of the flow velocities per area

To analyse flow velocities and directions at various locations within the soil container, the fluidised section was divided into a grid. This division allows for the calculation of average velocity and direction for each cell, facilitating straightforward interpretation. Within each grid cell, velocities of the top 30 percent fastest particles are averaged to account for the possibility of stationary particles in parts of the cell. This resulted in Figure 4.22, which illustrates the velocities of the particles per grid cell measured with the visual software. This image shows a clear distinction between the fluidised zone and the stationary zone on the diagonal between the faster and slowest moving grid sections. The stationary part also seems to show some movement of particles, which is cause by flickering particles and reflections.

The chosen percentage for analysis was determined through a systematic comparison with outcomes from three selected tests moments and three selected test moments. The method involved manually analysing the velocities to the outcomes of the model to ensure accuracy and consistency in the data, see Figure 4.23. Each test moment was chosen to represent different phases during testing, and the comparison was done with particle velocities close by the slope.

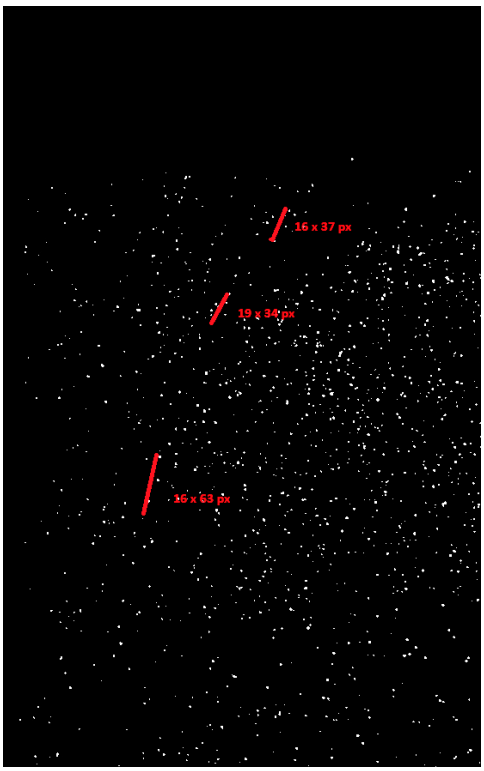

Figure 4.23: Example of visual validation for accurate particle velocity calculations: three particles travelled distance manually checked (Test 532)

To calculate the average flow velocity over the flow layer thickness, $\bar{u}$, across a 15-second interval, velocities were recorded from the first, middle, and last frames within this period. An average of these three velocity measurements was then computed to determine the final $\bar{u}$.

Estimation of the local particle concentration in the fluidised zone

In order to determine the particle concentration adjacent to the plug surface, an initial assessment of UV particle density was conducted. At the onset of each test, the soil container was thoroughly mixed, ensuring a uniform distribution of UV particles. Given the known porosity at the beginning of the test, it was possible to calculate an average density of UV particles per area (UV particle density), serving as a baseline for each experiment. This initial UV particle density allows for comparisons as the soil becomes fluidised by the jet. By measuring changes in UV particle density during soil fluidisation and comparing these to initial conditions, the porosity within the fluidised mixture can be estimated. Which in turn leads to the the local particle concentration c as well.

However, the method encountered limitations due to variations in UV particle density across different areas of the soil container. These discrepancies were attributed to uneven UV light distribution, rendering the data from the script on concentration over flow layer thickness unreliable for further analysis.

4.2.4. Limitations and considerations

In the conducted experiments, the particle movement is configured in a three-dimensional (3D) setup, namely a depth of 0.3 meters. This depth allows particles to travel in the respective direction, which then impacts the velocity measurements. The measured velocity is likely to be understated in comparison to the actual velocity due to the particles' ability to move in the depth direction, which is not accounted for in the two-dimensional (2D) observational measurements. Although, the density current where the plug surface velocity is measured has a flow layer with uniform direction parallel to the Perspex.

Subsequently, following the fluidisation process, the distribution of particle sizes relative to the height of the soil container will change. Typically, smaller particles tend to rise to the top of the sand bed, while larger particles settle towards the bottom of the container, this is due to the dependency of sedimentation speed on particle size, also mentioned in Section 2.1. This stratification effect is a direct consequence of the fluidisation, affecting the overall distribution and potentially influencing subsequent analyses or processes.

The use of UV lights significantly affected the visibility of particles; the concentration of visible UV particles increased with more focused lighting. However, this makes it impossible to calculate particle concentration accurately. Variations in visible particle counts across different tests, influenced by laboratory brightness levels, further complicate the normalisation of particle concentration at the start of a test. Determining the exact concentration of the particles can be an opportunity for further research, by exploring alternative illumination techniques or particle tracking methods in future work. For now the concentration in the soil container was done by estimation, using boundaries of fluidisation porosity mentioned by 2.1.1.

The soil container walls introduce an additional frictional force upon the fluid close to the Perspex, therefore influencing particle movement. This frictional force inherently decelerates the particles as they are near to the sides, thereby potentially skewing the velocity data. The camera only detected particles close to the perspex due to their position at the front of the image, which may affect the data accuracy. Further research in this topic is not in the scope of this study.

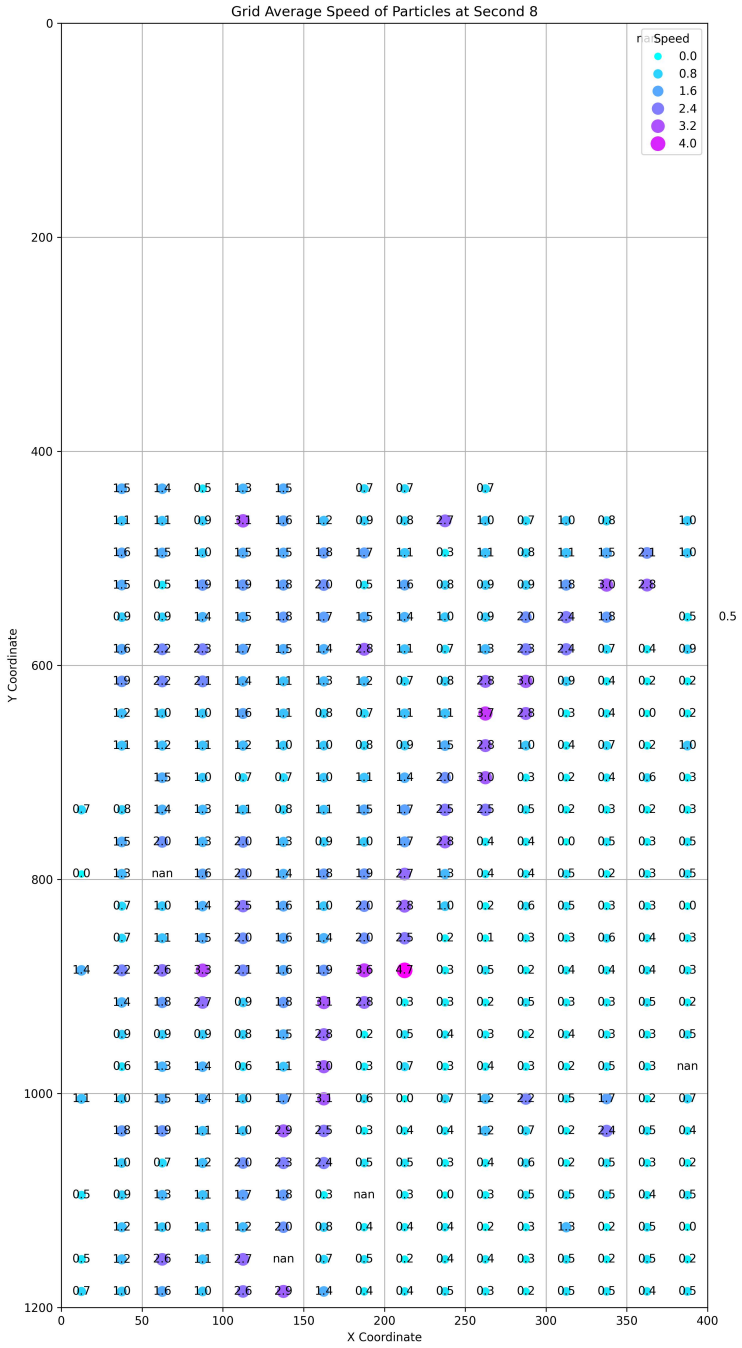

Figure 4.22: Average velocity per grid cell in the upper fluidised zone, showing 30 percent fastest particles (test 532)

5

Results & discussion on the optimisation of Vibrojet® performance

This research aims to optimise Vibrojet® performance during offshore installation by reducing shaft friction as much as possible while minimising jet flow. This approach maximises the installation speed of the monopile and reduces the capacity requirements for all components of the Vibrojet® system.

Previous chapters examined the literature describing processes inside the monopile, established a lab test setup to emulate these processes and investigate soil plug formation, and developed visual software to extract accurate data from the lab tests. This chapter, discusses the results of these lab tests. It delves into the formation and behaviour of the soil plug shape during lab tests, focusing on the accuracy of the plug surface velocity equation and the impact of different installation settings. Finally, the implications of deeper installation depths on plug behaviour are evaluated. By combining general observations and specific test analyses, this chapter attempts to optimise the performance of monopile installation using the Vibrojet®. This leads to the following research questions:

- What is the effect of the installation settings on the formation of the soil plug?
- How can the equation be updated to accurately predict the velocity of the plug surface?

Then, a conceptual model is proposed which will help to answer the main research question:

- How to optimise the performance of the Vibrojet® during offshore installation?

To understand the results presented in this chapter, it is crucial to visualise what these results actually mean. Figure 5.1 shows the output from the visual software, with blue particles representing the SW-mixture (or fluidised zone) and red particles representing the stationary soil plug. The variables $w_{t,650}$ and $w_{t,850}$ illustrate the trench width at heights H = 650 and H = 850, respectively, while $v_{p,650}$ and $v_{p,850}$ represent the plug surface velocities at these heights. These positions were selected because they provide the most accurate estimations of the plug surface shape from the visual software. Moreover, the flow velocity at these heights varies during testing, offering a more comprehensive view of the effects of the testing variables. In all tests, the jet starts at H = 0 and lowers at the selected trench penetration velocity until it reaches H = 1400. Measurements start once the jet reaches this lowest position. Initially, due to the high velocities, the water is turbulent and particles are not detected by the camera. Therefore, the results of this phase are not included in the analysis; only data from the point where the jet reaches its lowest position at H = 1400 until the end of the test are considered.

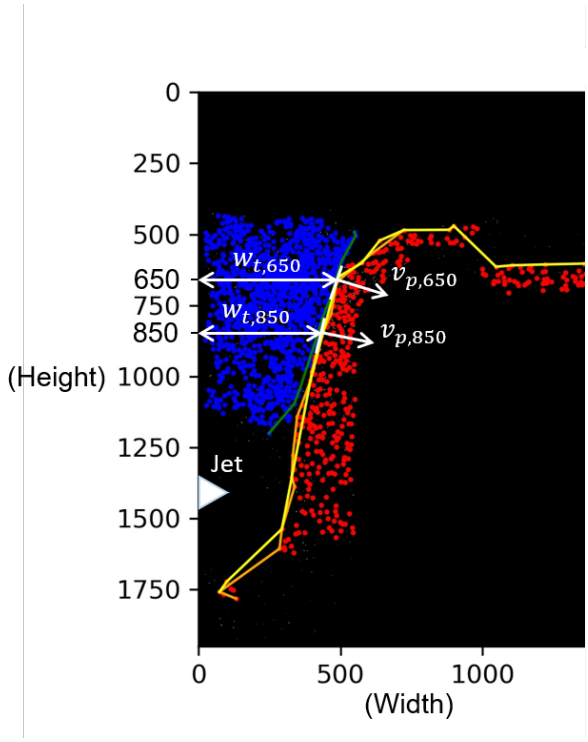

Figure 5.1: Illustration of the trench width w_t and the plug surface velocity v_p measured in the visual software

5.1. Plug surface velocity and impact of installation parameters

5.1.1. Impacts on test outcomes

Top layer does contains no UV particles: Depending on the frequency of the pump during soil preparation the height of the top layer without UV particles increases or decreases – between 4 and 15 cm. The UV sand has a smaller range of diameters and therefore the fine UV particles are less fine than the finest sand particles. The smaller particles have the slowest settling velocity and end up at the top of the soil directly after the fluidisation loop is turned of. Before the jet has stabilised and starts moving down, the jet pit has penetrated the top layer. In the jet pit the particles all mix thorough and therefore it does not cause any problems after the jet has moved downwards.

Fluidised area inside the trench: At the start of the tests, the jet descends from the top of the soil container to a position at height = 1400. During this descent, sand accumulates in the middle of the soil surface, forming a slope. Once the jet has moved down, the fluidised area containing the sand-water mixture remains below the top of the soil plug. As the jet penetrates deeper, the fluidised area stabilises, clearly separating the water from the sand-water mixture.

Test results: During the lab tests at Deltares the brightness in the lab was partially dependent on the weather outside. Due to the influence of brightness on the videos shot by the camera, some test produced better and more stable results than others. Subsequently, the operators in the lab were instructed to let the test run till a stable state was reached, i.e. the plug surface did not move anymore. Apparently, several tests were stopped to soon because the the change of the shape of the plug surface was not clear to the naked eye. This will be shown in the test comparison illustrations.

5.1.2. Estimation of plug surface velocity equation

To estimate the plug shape during monopile installation, it is crucial to be able to predict the displacement of the plug surface. In Chapter 2, an equation for the plug surface velocity was selected. This equation will be divided into two sections and thoroughly analysed to assess its accuracy and determine which parts of the equation need to be updated. The resultant plug surface velocity will be compared with the actual test values calculated using the visual software results to address the following research question:

- How can the equation be updated to accurately predict the velocity of the plug surface?

To answer this question, the equation was split into two aspects: the impact of erosion due to flow and the pure breaching effect (or wall velocity). This split was achieved by setting either the wall velocity to zero or the flow velocity to zero (resulting in $\theta = 0$) in Equation 5.1. Table 5.1 and Table 5.2 provide the values for the parameters used in the tests. The other parameters, such as flow velocity and slope angle, can differ every test and are therefore provided in the results.

$$v_p = u_s \left(\frac{v_{wall}}{2u_s} + \sqrt{\left(\frac{v_{wall}}{2u_s} \right)^2 + 0.018 \left(\theta - \theta_{cr} \right)^{1.5} D_*^{0.3} \frac{\Delta \rho k_l}{\Delta n u_s}} \right) \tag{5.1}$$

Variables	Value	Unit
g	9.81	m/s^2
ν	1.14E-6	m^2/s
rho_w	1000	kg/m^3
rho_s	2500	kg/m^3
d_{50}	337	$m\mu$
d_{15}	250	$m\mu$
n_l	0.47	-
k_l	0.00124	m/s
ϕ	34.54	$^\circ$
f_0	0.02	-

Table 5.1: Parameters used in the calculation of the plug surface velocity for R_d = of 100 percent

R_d [-]	n_i [-]	k_0 [m/s]
50	0.47	0.01242
75	0.42	0.00074
100	0.37	0.00042

Table 5.2: Calculated permeability connected to the changing relative densities

Erosion due to flow

When the slope angle is below the internal angle of friction ϕ, the wall velocity equals zero and the plug displacement is purely flow dependent. In the lab tests, the average flow velocity over the flow layer thickness ranged between 0.03 and 0.10 meter after the jet has passed. In order to have erosion due to flow according to the plug surface displacement equation, the Shields parameter must be higher than the critical Shields parameter. Figure 5.2 shows a plot of the Shields parameter and the critical Shields parameter against the average flow velocity over flow layer thickness at a slope angle (β) of zero. This shows that there is no erosion due to flow during the lab tests according to the v_p equation in the regions of $\bar{u}$ below 0.30 m/s. Figure 5.3 shows the plug surface velocity in mm/s against the average flow velocity over flow layer thickness with a slope angle of zero and a relative density of 100 percent. For the relative density of 50 and 75 percent the threshold for non-zero erosion has the same value.

The result of $\bar{u}$ being too low to start moving particles means that there was no erosion due to flow in any of the lab tests in this study. The equation also suggests that the slope angle does not influence the erosion velocity due to flow, since it is not incorporated in this part of the equation. Additionally, sedimentation in not part of the equation and cannot cause a negative plug surface velocity.

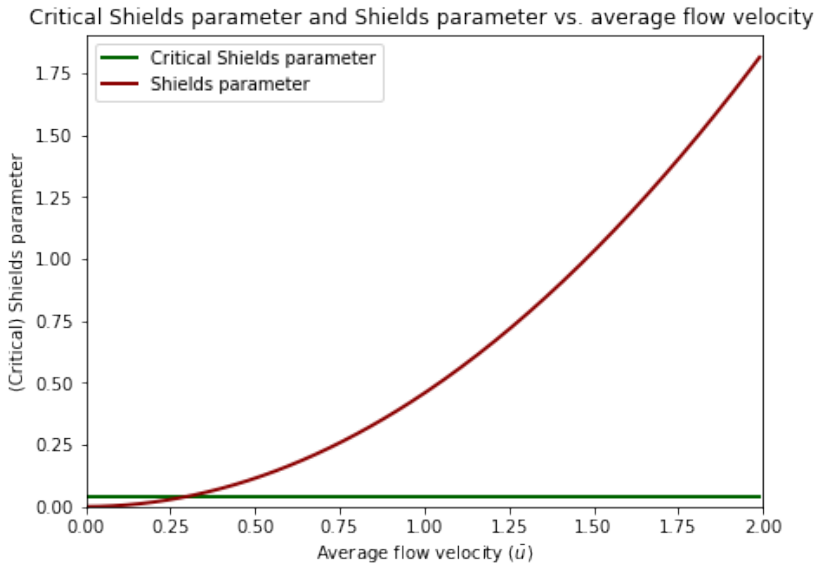

Figure 5.2: Shields parameter and Critical Shields parameter plotted against the average flow velocity over flow layer thickness, with D_r = 100

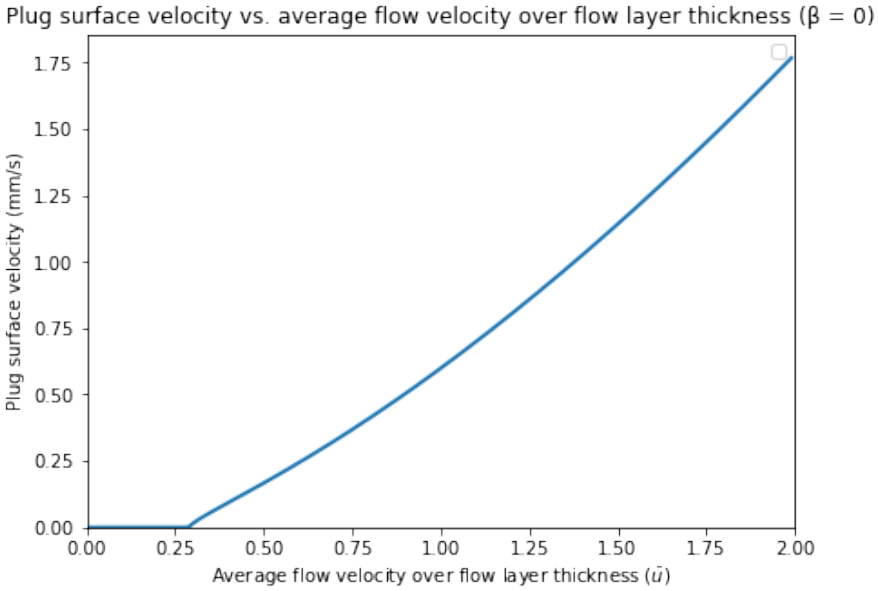

Figure 5.3: Plug surface velocity plotted against the average flow velocity over flow layer thickness, with D_r = 100 and β = 0

Plug surface displacement: breaching

As stated in the previous paragraph, the plug surface velocity due to flow is zero, so only the effect of breaching needs to be considered. To evaluate the plug surface velocity, two consistent heights were chosen in order to enable comparison between different tests and to ensure that variables such as average flow velocity $\bar{u}$ and slope angle could be compared. At the higher location (H = 650), there was generally a lower flow velocity and a gentler slope angle compared to the deeper location (H = 850). Figure 5.1 illustrates the parameters used to analyse the slope in this and the following paragraph.

As mentioned in the lab observations, not all tests provided stable results, so 5 tests with the most reliable data were selected. Table 5.3 summarises of these tests. In the table, three parameters cause changes in the calculated plug surface velocity: relative density D_r, flow velocity $\bar{u}$, and slope angle β. The right two columns show the tested and calculated plug surface velocity. The highest v_p recorded during the tests was selected for analysis after the jet reached its lowest position. Figure 5.4 shows

the extraction of the trench width over time and the slope angle of the plug surface. Equation 4.21 was used to calculate the tested plug surface velocity. The tested v_p was obtained over a period of at least 15 seconds to ensure that it is not sensitive to unstable measurements.

Test ID	**Height**	D_r [-]	$\bar{u}$ [mm/s]	β [degree]	**Tested** v_p [mm/s]	**Calculated** v_p [mm/s]
532	650	57	49	70	0.6	12.90
532	850	57	63	73	1	11.02
534	650	55	43	74	0	11.27
534	850	55	52	65	0.2	7.00
732	650	105	51	70	1.7	8.52
732	850	105	66	75	1.9	13.83
735	650	79	64	68	1.2	12.58
735	850	79	80	75	1.6	14.13
736	650	81	57	80	1.5	7.83
736	850	81	73	89	2.0	10.30

Table 5.3: overview of parameters and plug velocity of the most reliable tests used in the equation

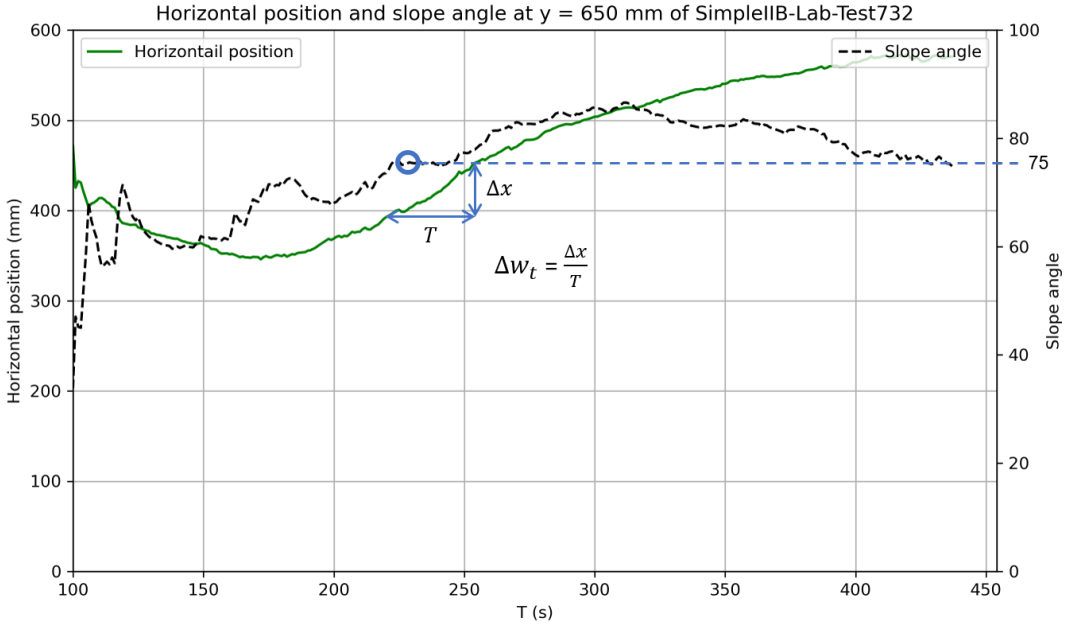

Figure 5.4: Method for extracting the slope angle and the trench width over time

Analysis reveals that the theoretical equation overestimates the observed plug surface velocity by a factor of eight, indicating a significant discrepancy between assumptions and actual experimental outcomes. This means that the equation is not accurate calculating the plug surface velocity, as shown in the results given in Figure 5.5. Here, the tested and calculated plug velocity are plotted for the selected tests. What can be seen is a clear overestimation of the plug velocity in all tests of both heights. The closest results are in test 732, this is because a high relative density decreases the value of the calculated v_p.

Furthermore, test 534 shows a v_p of zero and near zero for heights 650 and 850 respectively, and also the largest difference between the tested and calculated v_p. This indicates that the equation not only overestimates the plug surface velocity but also needs to take into account other factors that could reduce the v_p to zero. In particular, when the slope exceeds the internal friction angle, the equation consistently returns a positive value for the plug surface velocity, which contradicts the test results.

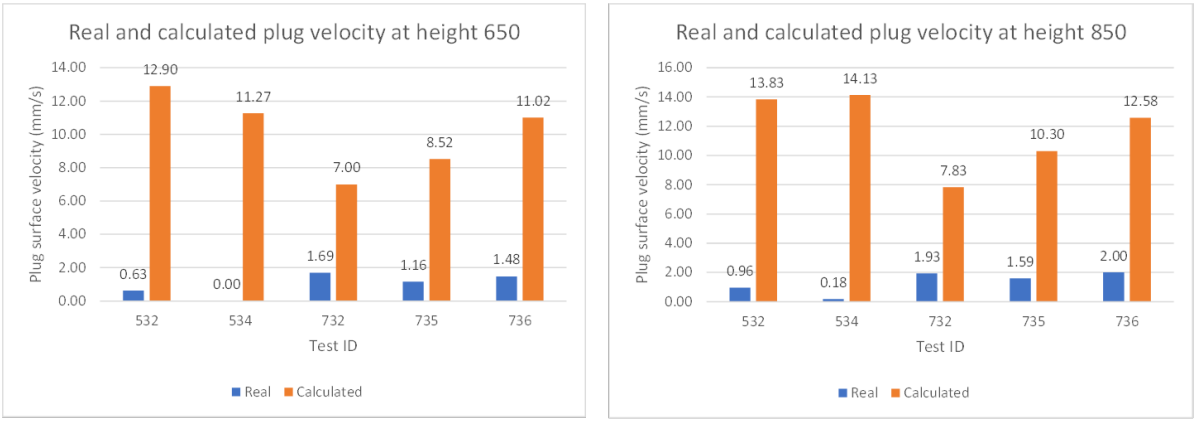

Figure 5.5: The tested and calculated plug surface velocity at heights 650 and 850

Plotting the plug surface velocity against other test variables revealed on distinct relationship: between jet penetration velocity and plug surface velocity, as shown in Figure 5.6. Jet penetration velocity has a positive impact on the v_p, which increases with higher jet penetration velocity. Although, the jet penetration velocity is not a parameter in the equation for calculating the plug surface velocity, it impacts the initial width of the trench and slope angle of the plug surface. This is discussed in the next section.

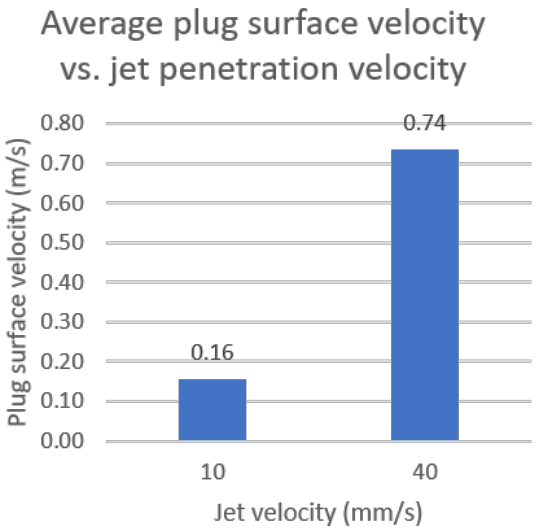

Figure 5.6: The tested plug surface velocity against the jet penetration velocity

5.1.3. The impact of changing installation settings on plug formation

This section presents the results of various installation settings: flow rate, relative density, jet penetration velocity, and seepage. Additionally, the concentration inside the fluidised zone is discussed. The direct results and relationships of these settings on the plug surface shape are discussed separately. These discussions aim to address the following research question:

- How do variations in installation settings influence the resulting soil plug shape?

A table with all different parameters used in this section and figures of all results can be found in Appendix A.3. A total of 12 tests were conducted, of which 10 provided useful results.

The impact of flow rate

The first installation setting to be adapted is the flow rate. Table 5.4 shows the installation setting of three tests with relative density and jet penetration velocity at the lowest setting and the full range of

flow rates from 80 to 120 L/min. Table 5.5 shows the installation settings of the same range of flow rates with a higher relative density and jet penetration velocity.

Figures 5.7 and 5.8 show the horizontal distance from the left side of the soil container to the plug surface over time on H = 850. It is clear that the flow rate has a significant impact on the plug surface shape for both relative density settings set at 50 and 75 percent. Unfortunately, test 742 was stopped to quickly and does not provide useful results. There seams to be a relationship between the stable trench width and the flow rate, as the trench width increases with the flow rate. Additionally, although the trench seems to stabilise at around 250 seconds, the trench width begins to increase again, and all tests stopped at this stage.

Test ID	**Flow rate** [L/min]	**Relative Density** [-]	**Jet penetration velocity** [mm/s]	**Seepage height** [m]
532	80	57	10	2500
533	100	53	10	2500
534	120	55	10	2500

Table 5.4: Installation settings with changing flow rate, $R_d = 50$ and v_{jet} = 10

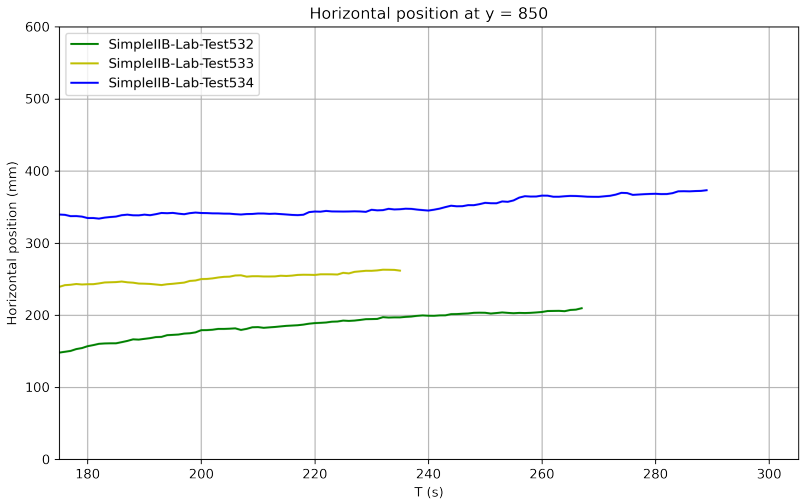

Figure 5.7: Trench width over time of test 532,533 and 534

Test ID	**Flow rate** [L/min]	**Relative Density** [-]	**Jet penetration velocity** [mm/s]	**Seepage height** [m]
742	80	77	40	2500
736	100	81	40	2500
735	120	79	40	2500

Table 5.5: Installation settings for changing flow rate, $R_d = 75$ and v_{jet} = 40

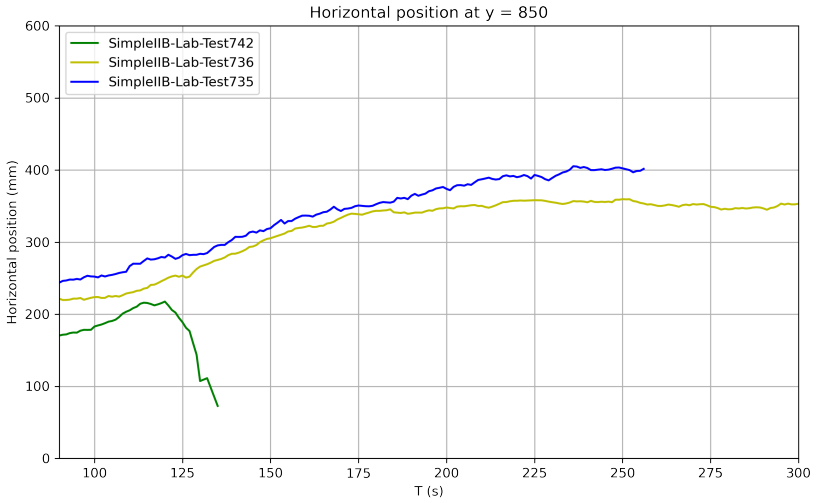

Figure 5.8: Trench width over time for test 742,736 and 735

To establish a relationship between stable trench width and flow velocity, all stable trench widths from this study were analysed. However, widths from tests with different seepage flow were excluded and the remaining data were plotted against flow rates in Figure 5.9. There seems to be an almost linear relation between the flow rates and the stable trench widths. Although the spread of the trench widths is quite wide at all flow rates. Reasons for this could be that lab test were stopped too early and therefore not reaching its stable shape trench width. Or, the influence of the relative density. Although, it is not certain the trench width continues to increase with an early stopped test, a trend-line is plotted between the averages of every flow rate.

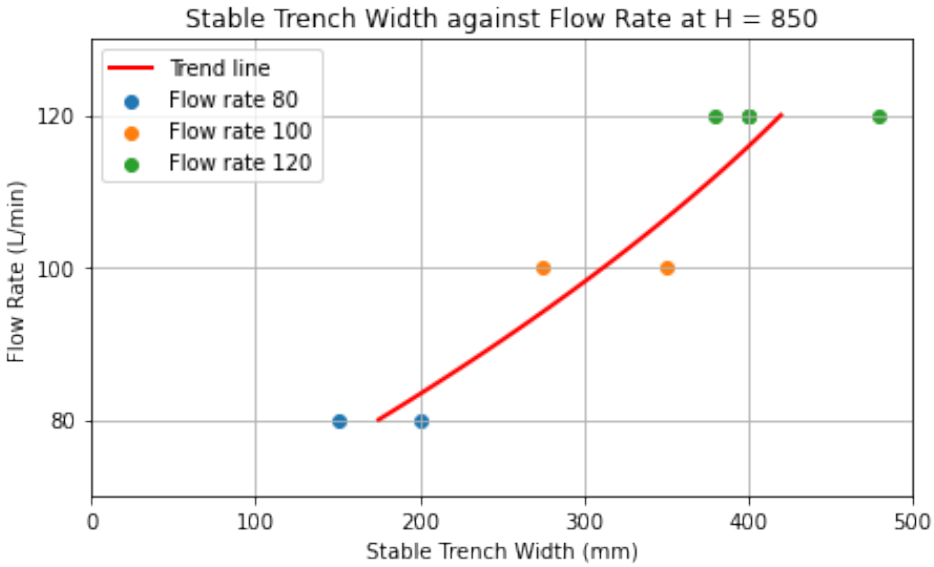

Figure 5.9: Stable trench width sorted per flow rate including trend-line through averages per flow rate

Figure 5.10 shows the stable slope angle at a height of 850 compared to the flow rate. Generally, the flow rate decreases as the slope height increases. However, there is an exception where a test at 120 L/min shows a higher slope angle compared to one of the blue tests. On average, lower flow rates lead to steeper slope angles because less fluidised volume results in a narrower and steeper trench.

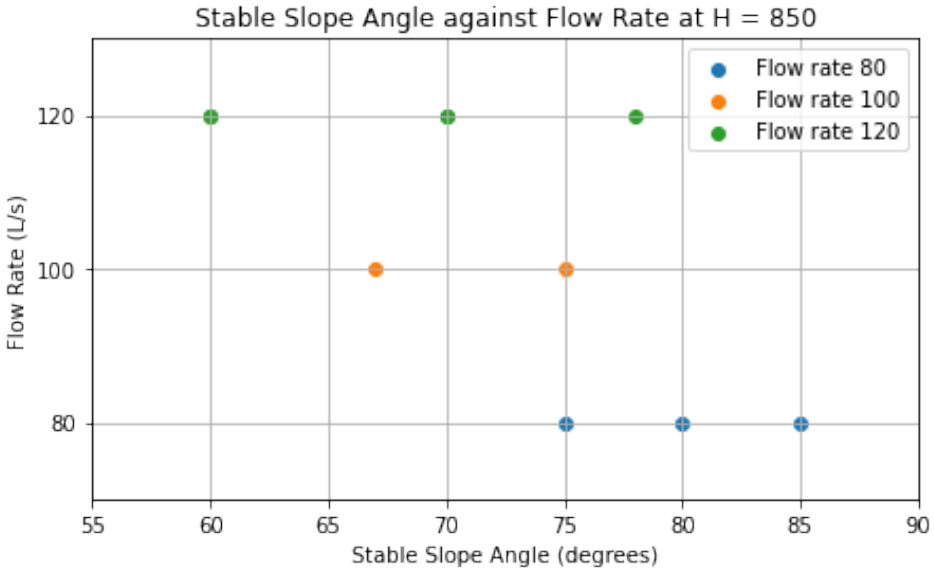

Figure 5.10: Stable slope angle sorted per flow rate

The impact of relative density

The impact of relative density on soil behaviour was assessed using three tests. However, one test (552) did not yield useful results and was excluded from Figure 5.11. The figure shows minimal differences between the tests at 79 percent and 105 percent relative density. Test 735, with a smaller relative density, increased slightly faster than test 732, and converged again after 250 seconds. However, test 735 ended prematurely. With only two valid results, it's challenging to draw firm conclusions about the impact of relative density. A higher R_d means a lower initial height, potentially affecting the trench width and fluidised volume. This should be taken into account when reading the results of the lab tests. What can be seen though is that the difference at the beginning is not significant and that after 220 seconds the highest relative density does not yield the maximum trench width.

As shown in the literature references 2.1 and 2.2.3, higher relative density leads to lower initial porosity, affecting both the permeability of the soil and dilative processes.

- Higher relative density and consequently lower porosity results in reduced permeability, limiting flow through the soil plug. This reduced flow can decrease the seepage force acting on the plug, which can increase erosion rates is be discussed in Paragraph 5.1.3
- Lower permeability also reduces the superficial velocity at the plug surface, slowing down the dilation process. Moreover, a lower initial porosity means a greater potential change in volume from dense to loose soil, in turn reducing the erosion rate.

Test ID	**Flow rate** [L/min]	**Relative Density** [-]	**Jet penetration velocity** [mm/s]	**Seepage height** [m]
552	120	51	40	2500
735	120	79	40	2500
732	120	105	40	2500

Table 5.6: Test settings changing R_d

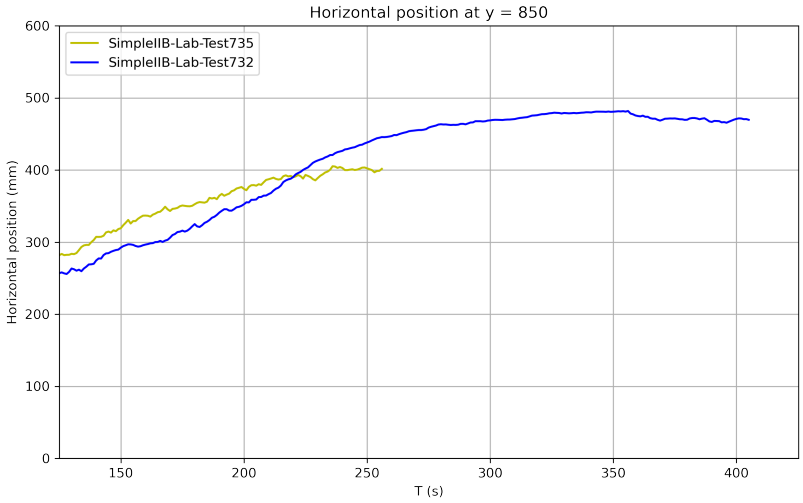

Figure 5.11: Trench width over time for test 735 and 732 with changing R_d

The impact of jet penetration velocity

The jet penetration velocity was tested at velocities 10, 20, and 40 mm/s. This provided the expected insights which are related to the plug surface velocity measurement, given in Figure 5.6. Figure 5.12 illustrates the horizontal position of the trench at H = 850 mm. Tests 1211 and 735 with respectively 20 and 40 mm/s jet penetration velocity do not differ significantly and increase from the same initial trench width of 250 mm to 400 mm width. Though, test 623 with the lowest jet penetration velocity has an initial trench width of 350 which increases to the same trench width as the other two tests.

Therefore, the jet penetration velocity has a significant impact on the plug shape until a stable slope is reached. The slower the jet moves the bigger the width of the trench when the jet reaches its lowest position, and causes less changes in the plug surface shape afterwards. When the jet moves faster, the trench is smaller when the jet reaches its lowest position. Consequently, the plug surface shape will be steeper and the plug surface displacement after reaching the lowest jet position will be greater. As expected, the impact of penetration velocity on the shape of the plug surface decreases over time and does not affect the stable shape of the plug surface.

Test ID	**Flow rate** [L/min]	**Relative Density** [-]	**Jet penetration velocity** [mm/s]	**Seepage height** [m]
623	120	77	10	2500
1211	120	77	20	2500
735	120	79	40	2500

Table 5.7: Test settings changing jet penetration velocity

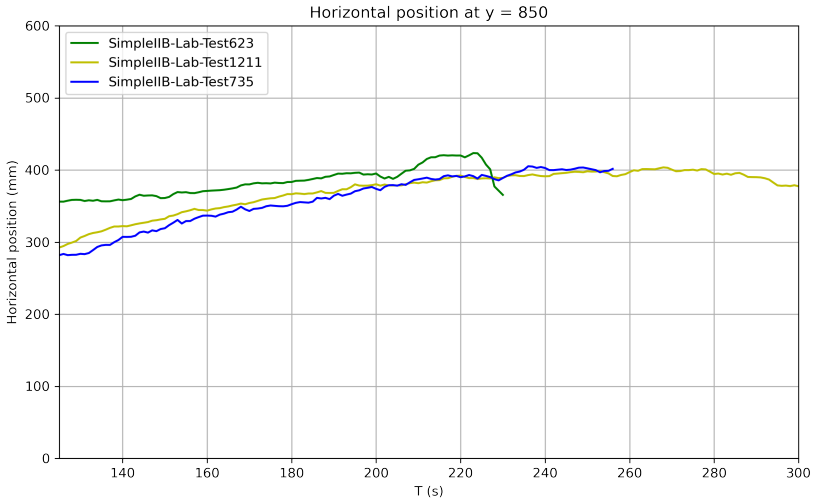

Figure 5.12: Trench width over time of test 623, 1211 and 735

The impact of seepage

The influence of seepage was expected to have an significant affect the stable plug surface shape. Therefore, three tests were conducted with different seepage system heights, which are inversely proportional to the head difference, as given in Table 5.8.

Test ID	**Flow rate** [L/min]	**Relative Density** [-]	**Jet penetration velocity**[mm/s]	**Seepage height** [m]	**Head difference** [m]
654	80	51	10	0	2500
653	80	51	10	1490	1010
532	80	57	10	2500	0

Table 5.8: Installation settings for changing seepage height

Figure 5.13 presents the resulting flow rate in L/min (or dm^3/min) measured by the flow meter in the seepage loop. As observed, a higher head difference leads to an increased seepage flow rate. Figure 5.14 shows the trench width over time for the H = 650 mm, and shows no significant differences between the different amounts of seepage flow rate. The differences are so small that the influence of seepage at this height of the plug surface shape seems to not exist. The comparison for H = 850 mm does yield a difference for test 654 with the highest seepage flow (Figure 5.15), which has only half of the trench height as the test with the lowest seepage. This indicates that the seepage flow does cause a stabilising effect as mentioned in Section 5.1.3 and could be the reason for higher stable slope angles than the angle of repose.

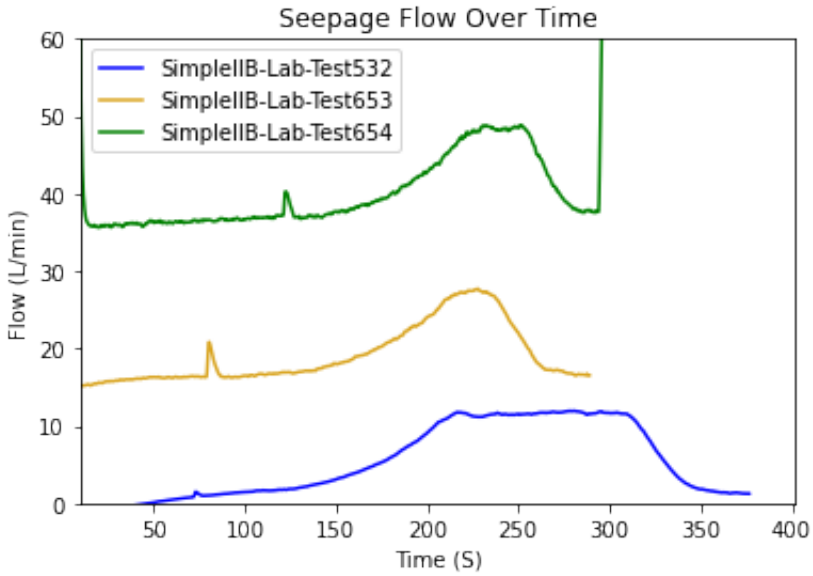

Figure 5.13: Seepage flow test comparison

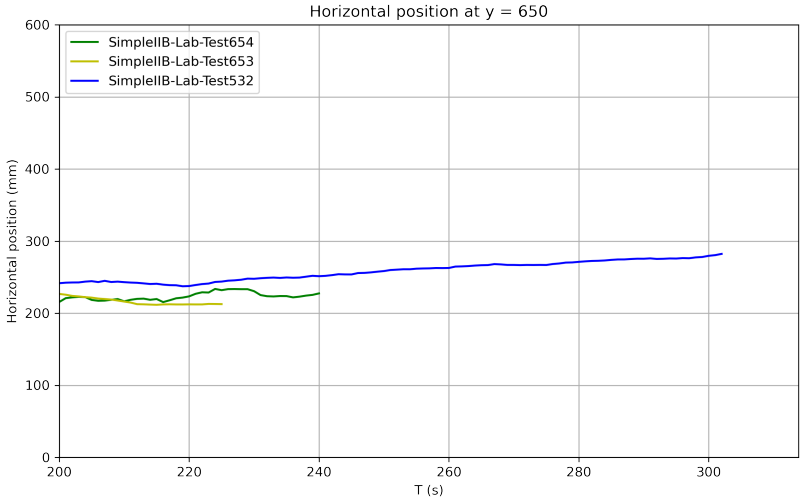

Figure 5.14: Trench width over time for test 654, 653 and 532

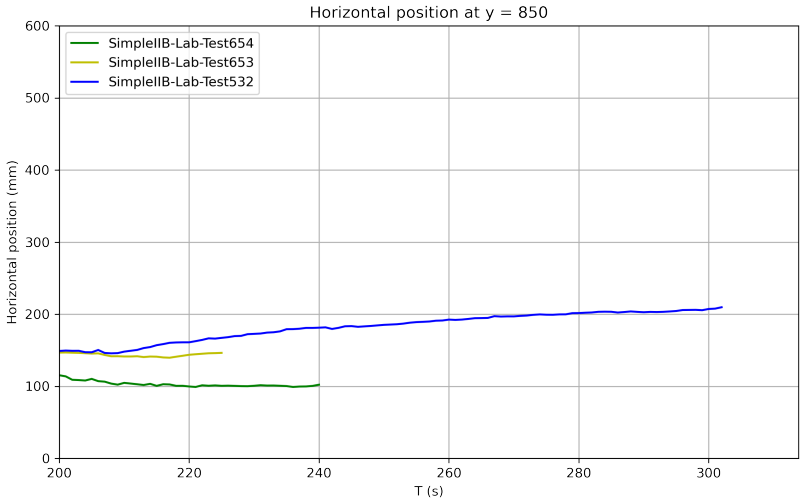

Figure 5.15: Trench width over time for test 654, 653 and, 532

To visualise the path of the seepage flow, a test was done in which red tracer fluid was added to one of the water reservoirs. When the jet reached its lowest position the inlet of the pump was changed from the reservoir without tracer fluid to the reservoir with tracer fluid. This resulted in Figure 5.16, a snapshot of the test with the jet in its lowest position before it moved back up. The red zones in the image indicate areas where the tracer fluid has flowed, signifying active seepage, while the non-red zones show areas where no seepage flow has occurred since the tracer was introduced. It's important to note that only the front of the soil container is visible; there could still be flow occurring in the middle of the soil container that is not visible from this perspective.

The figure explains the minor changes in trench width at the H = 650 were less seepage is present. H = 850 shows a significant difference in trench width of 200 percent, which perfectly aligns with the expected effect of seepage.

Test ID	Flow rate	Relative Density	Jet penetration velocity	Seepage height
1216	120	77	10	0

Table 5.9: Test settings tracer test

Figure 5.16: Tracer fluid test screenshot just before the jet moves up again

Additional effect: high concentration

The concentration is not really an installation parameter, but is an additional effect with in the soil container and a monopile because of the confined space where the fluidised sand has nowhere to go. The concentration within the fluidised zone was determined by measuring the relative pressure between two sensors, with one placed higher in the soil container than the other. To accurately measure the concentration of the mixture, the area between the two sensors must be fully fluidised. Figure 5.17 illustrates all total and pore water pressure sensors next to the jet position in the red dotted line. PWP sensors C1B7 and C1B4 turned out the be the most useful, because they are positioned most to the left, and thus are the first to get fluidised. Moreover, they were right in the middle of the fluidised zone. Figure A.2 in the appendix gives an overview of all sensor locations.

Figures 5.18 and 5.19 show the jet height (measured from the bottom of the soil container) and the calculated concentration between the two sensors. Every test that fluidised the area between the two sensors resulted in a stable concentration of approximately 40 % volumetric concentration. The concentration drop after 70 seconds was attributed to the upper sensor increasing in relative pressure while the lower sensor stays remained. This is the case until the sand around the lower sensor fluidises, thereby causing the relative pressure to increase rapidly until the flow stabilises and the concentration of 40 % is achieved.

Test ID	Flow rate	Relative Density	Jet penetration velocity	Seepage height
	[L/min]	[-]	[mm/s]	[m]
735	120	79	40	2500
736	100	81	40	2500

Table 5.10: Test settings for concentration plots

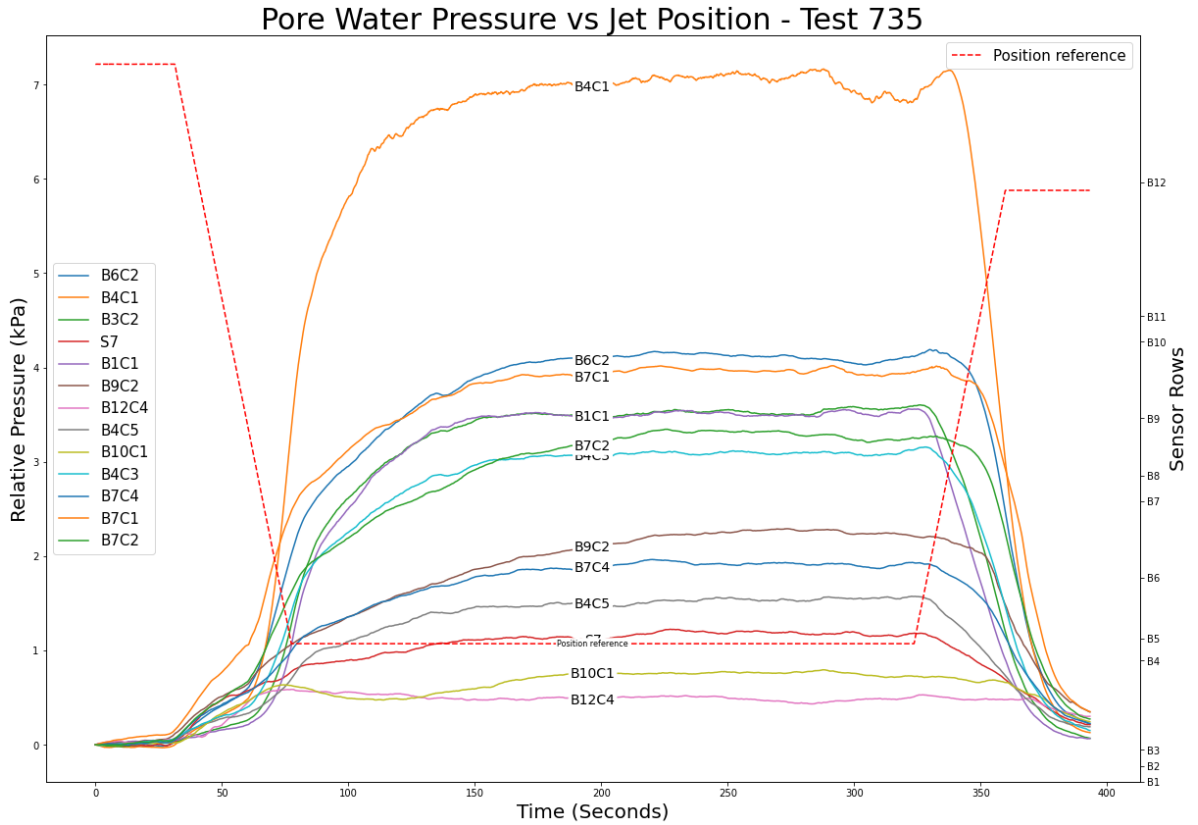

Figure 5.17: Relative pressures of all total and pore water pressures sensors in test 735

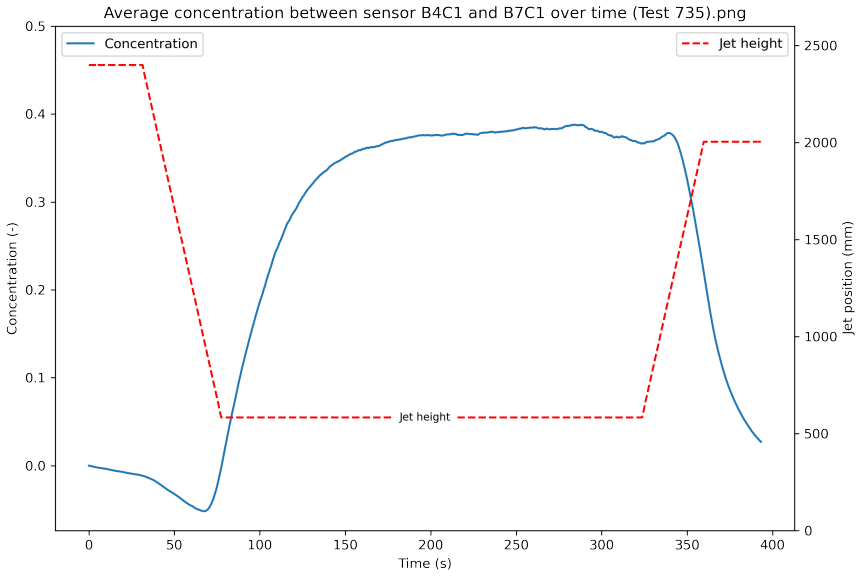

Figure 5.18: Measured concentration over time for test 735

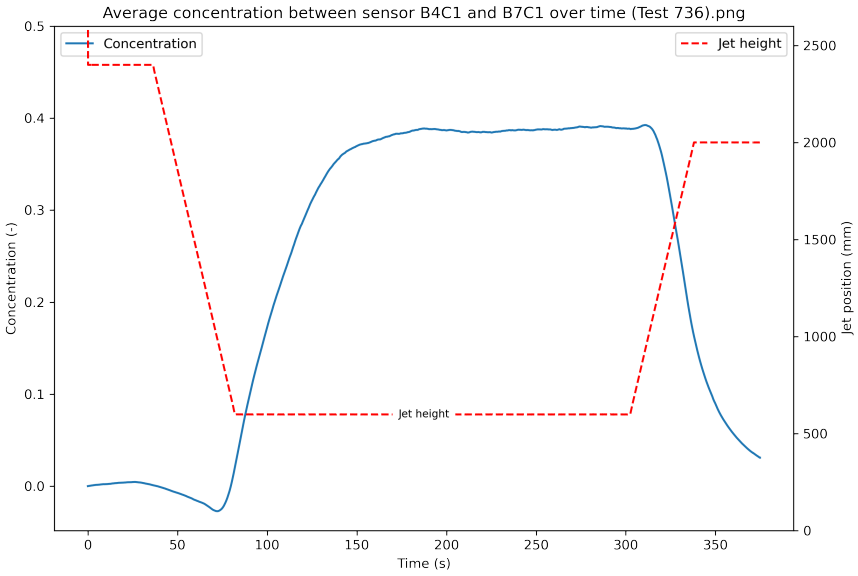

Figure 5.19: Measured concentration over time for test 736

During the test, relatively low flow velocity near the plug surface was measured, lower than normally reported in the literature, mainly due to the high concentration in the environment. This high concentration suppresses turbidity currents, leading to reduced flow velocities near the slope. Turbidity or density currents usually form from density differences between the mixture near the slope and the surrounding water (Alhaddad et al., 2020). The higher concentration of the fluidised area reduces the density difference and thus the action of gravity, which decreases the velocity of the turbidity current. Additionally, the confined space of the soil container causes the flow from the jet to be mostly directed upwards to the overflow of the soil container. The upward flow in the fluidised area does not directly change the slope of the plug surface because there is still a downward flow layer next to the surface. However, this upward flow reduces the speed of the downward flow layer, which in turn affects the shape of the plug surface.

5.1.4. Discussion on the plug formation process

Plug surface formation

The equation for plug surface velocity does not accurately predict the velocity in the current setup. To better understand the formation of the plug surface, Figure 5.20 was created, depicting two plug shapes within the soil container: the initial shape and stable shape. The initial shape occurs when the jet reaches its lowest setting (H = 1400), and the stable shape is observed after a period when the plug no longer moves. The impact of installation settings and model parameters on the plug surface velocity is analysed based on the evolution of these shapes during testing. If the trench is small (underdeveloped) compaired to the stable trench width, the velocity will be relatively high. Conversely, if the trench is large (developed) relative to the stable trench, the velocity will be lower.

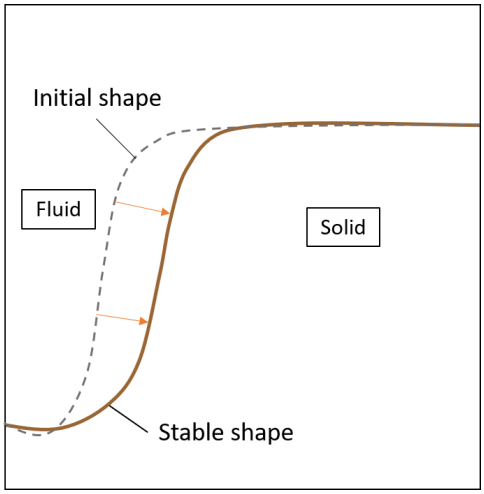

Figure 5.20: Drawing of the initial shape and the stable shape of the plug surface

The influence of the installation settings on the initial shape and stable shape is as follows:

- The jet penetration velocity has a substantial impact on the plug surface velocity. A higher penetration velocity gives the jet stream less time to erode a wide trench, and a lower penetration velocity results into a relatively wider trench. Therefore, a high jet penetration velocity will results in a relatively underdeveloped trench and a lower jet penetration velocity will lead to a relatively developed trench. The jet penetration velocity shows no difference in the stable plug surface shape.
- The relative density should have a significant impact on the plug shape formation, according to its influence on the permeability and dilative processes. Unfortunately, the test results are inconclusive because one test was not useful. Though, there is not a significant difference between the 75 and 100 percent test because it both negatively and positively effects the erosion rate.
- The flow rate impacts both the initial shape and stable shape of the soil plug, and therefore has little to no impact on the plug surface velocity. A lower flow rate at the start will cause less erosion at the start of the test and a less wide stable shape. A higher flow velocity will cause more erosion during the downward movement of the jet and a wider trench when the stable plug surface shape is reached.
- The seepage flow plots show a difference in stable trench width, especially at H = 850 mm for setting maximum head difference. A tracer test was done to see the flow directions in the sand. This test indicates that more seepage is occurs in deeper parts of the trench, which is in line with the stabilising effect.

The updated equation for the plug surface velocity

As shown in Section 5.1.2, the equation from previous studies used to estimate the plug surface velocity does not yield accurate results. The calculated values for v_p are significantly overestimated, even when the slope is stable. This is probably because the equation fails to account for factors such as increased concentration, upward flow in the fluidised zone, and seepage into the soil plug. The equation is primarily based on conditions typical of a clear water environment and simplifies certain effects. To develop an equation suitable for the lab tests in this study and potentially for offshore monopile installations, it is essential to include the previously discussed effects in the equation for plug surface velocity.

- *Seepage force:* The difference in pore water pressure between the sensors in the fluidised area and those within the soil plug is significant. The PWP difference causes a suction effect that pushed the water from the fluidised zone into the pores of the soil plug particle and to the underside of the monopile, called seepage flow. To account for this seepage flow in the equation for the plug surface velocity, the effects of dilatancy and superficial flow must be taken into account (see Paragraph 2.2.3).

It is suggested that the increase in pore volume that causes dilation, is compensated by the specific inflow of water into the plug q_s. Similar to the superficial flow velocity v_s, the plug surface velocity due to the specific inflow of water can be calculated using the relative change in porosity. This leads to the following equation that should be added to the plug surface velocity equation:

$$v_p = -q_s/\Delta n \tag{5.2}$$

- *Added sedimentation:* The effect of sedimentation was integrated inside the equation, but due to the relatively high concentrations inside the monopile during installation, the effect should be emphasised. In van Rhee, 2015 the sedimentation velocity is a separate part of the erosion equation (Equation 2.31). It is proposed that the same should be done for the plug surface velocity equation.
- *Return flow containing particles:* The concentration during testing reaches forty percent in the fluidised area, and potentially higher in the density current near the slope. A study by Van Rhee suggested that, due to the principle of continuity, an eddy transporting a volume of water and sediment away from the bed necessitates the return of an equivalent volume of water to the bed surface (van Rhee and Talmon, 2010). With a high concentration, the likelihood of this return flow containing particles is greater, which in turn leads to reduced erosion. Adding a damping factor that depends on the concentration mixture near the soil plug could improve the accuracy of the equation.
- *Influence slope angle:* The equation for the plug surface velocity that accounts for the erosion due to flow does not include the effect of an increased slope angle. This seems incorrect, since the slope angle generates increased particle instability, as shown in literature Figure 2.10. Although the equation in van Rhee, 2010 incorporates slope angle using an adapted critical Shields parameter to enhance erosion prediction accuracy (Equation 2.28), it tends to overestimate erosion velocity. With newly fitted parameters, this model could more accurately represent the dynamics of a slope under the influence of fluid flow.

Relation between flow rate and fluidised area

Previous research showed that the porosity of a fully fluidised certain mass of sand in a confined space is dependent on the flow rate of water that is pumped underneath it (GBMWorks, 2020). This follows fluidisation theory, which explains that sand gets fluidised when the drag force of the upward flow together with the buoyancy force can exceed the gravitational force acting on the particles. When this flow rate and thus the drag force increases the porosity of the fluidised sand increases as well.

During this research, the pore water pressure measurements were utilised to calculate the average concentration in the soil container between sensors C1B7 and C1B4. It revealed that the SW-mixture concentration stabilises at 40 percent for different flow rates. This means that as the flow rate increases, more sand is pulled into the fluidised zone, leading to an increase in the fluidised volume. This is also in line with the linear relation found between the trench width and the flow rate in Figure 5.9.

This relationship suggests that the optimal flow rate for Vibrojet® installations can be determined by the total volume of sand that needs to be fluidised. If the ideal shape of the plug is known, then the flow rate can be adjusted accordingly to achieve this shape.

5.2. The effects of increased installation depth

The overlaying goal of GBM Works is to know how to operate the jet in offshore campaigns, were installation depths can reach until 30 meters deep underneath the soil surface. During these tests other phenomena like vibrations, mixed soil densities, and even rocks could play a role. These phenomena are out of the scope of this research. However, the height of the soil plug is something that will be taken into account.

Due to the greater depths of installation, the height of the plug will increase as the monopile goes further into the soil. At a certain depth, the gravitational forces due to the height of the soil plug may become significant. As the axial load from the soil plug increases, the stresses within the plug will also increase. The ratio of axial to radial stresses becomes a critical factor in maintaining stability. According to the Mohr-Coulomb failure criterion, as this ratio increases, the likelihood of reaching the failure envelope also increases, bringing the soil plug closer to a slope failure. This failure would not

look like the plug surface displacement where the top layer displaces over time, but like a crack inside the soil plug where multiple layers slide down together.

When using the Vibrojet®, multiple interrelated effects come into play that influence the stability of the soil plug. Phenomena such as flow, seepage and increased particle concentration could impact the plug stability. The increased concentration, creates a difference in pore water pressure inside and outside the plug. Due to the higher mixture density the pressure of the fluidised sand increases over depth. When the pore water pressure inside the plug is lower than outside the plug, it increases the shear strength of the soil, potentially making the plug more stable. Also, the outflow of water from beneath the pile (seepage) can lead to a decrease in pore water pressure inside the soil plug. A lower pore water pressure typically results in an increase in effective stress, which can enhance the shear strength of the soil and potentially make the plug more stable.

It's important to note that the effects of jet flow, seepage, and increased particle concentration on the plug's stability are not entirely clear and depend on the installation settings and penetration depth of the pile. For example, the differential pressure between the inside and outside of the pile is increased due to a high pressure because of the weight of the mixture. Therefore, while lab test results can provide useful insights, they need to be carefully applied to real-world conditions, especially considering the potential for slope failure at greater depths. This means taking into account all factors that could affect stability when moving from smaller-scale lab tests to full-size applications.

5.3. Method for optimising Vibrojet® performance

Combining models

Sections Discussion on the plug formation process 5.1.4 and The effects of increased installation depth 5.2 have been used to come up with a conceptual model that can be used to optimise the Vibrojet® performance during offshore installations. As mentioned in the introduction, alongside the equation for plug surface displacement, several models have been developed to simulate all mechanisms inside the monopile during Vibrojet® installation. These models allow for calculating the trench width at various depths and determining the optimal flow rate. This optimal rate is the lowest possible that still ensures a stable plug formation. To better understand the method for optimising Vibrojet® performance, the input and output of the models will first be explained combined with Figure 5.21. Following this, the principle by which these models interact and function together will be demonstrated.

1. *Jet erosion model:* This module outlines the stand-off distance below the jet, the width of the fluidised zone, and the slope of the eroding soil surface at the level of the jet ring. These parameters are defined as functions of the jet and soil characteristics, as well as the penetration velocity of the monopile.
2. *Hydrodynamic model:* This model simulates the SW-mixture flow inside the fluidised zone in the fluidised area. The velocities and concentrations of the mixture flowing over the surface of the eroding soil column are predicted. They are affected by the fluidised material during installation both from the jet erosion module and from the plug displacement model.
3. *Seepage flow model:* This model describes the amount of water flowing into and through the soil plug (groundwater flow) past the underside of the pile (pile tip) during the installation process. This is affected by the pressures inside the fluidised zone, the shape of the soil plug and the soil characteristics.
4. *Plug displacement model:* This model calculates the displacement of the soil plug during erosion by using the plug surface velocity equation that was studied in this research. It describes the trench width and slope angle of the soil plug at every zone during the installation process. It uses the trench width and angle next to the jet form the jet erosion model, the flow velocities and concentration from the hydrodynamic model, and seepage flow rate inside the plug from the seepage flow model.

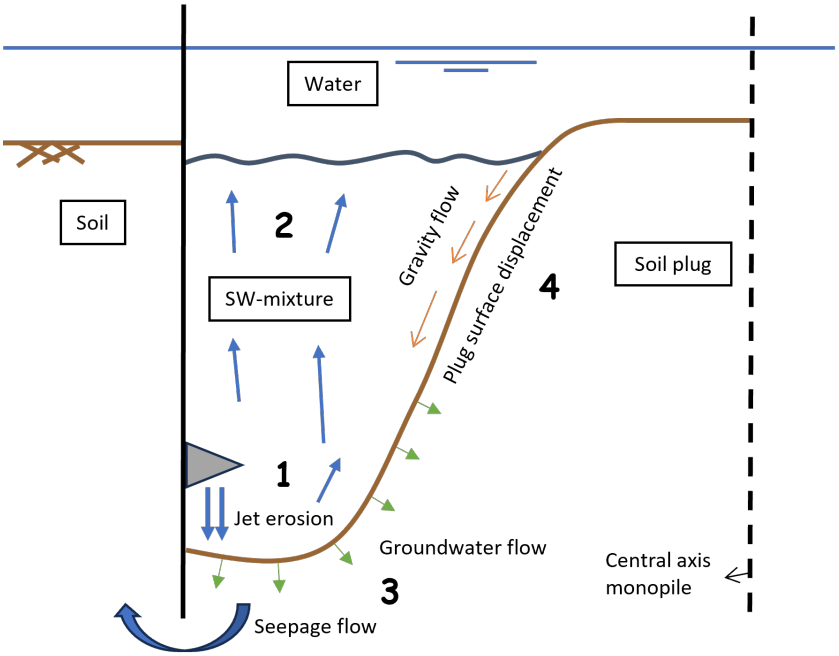

Figure 5.21: Drawing of the models and relevant mechanisms inside the monopile

Working principle

The representation of the plug shape is illustrated in Figure 5.22. The full length of the monopile is divided into segments by nodes placed at a specific interval, such as every half meter. These nodes represent the shape of the plug surface inside the monopile. The tests begin at t = 0, where each node is positioned on the left side, which corresponds to the outer part of the monopile, as no sand has been fluidised yet. With each time step, the position of each node is calculated using the previously mentioned models. As the sand fluidises, the characteristic shape of the plug surface begins to form. The formation process for one time step is explained as follows:

Before the monopile installation with the Vibrojet® begins, a cone penetration test (CPT) and soil sampling is done to collect information about the soil at the location the monopile is placed. This data will be used as an input for the models and to perform a driveability analysis from where the monopile penetration velocity is calculated.

The width of the initial trench is calculated by using the jet erosion model, which is dependent on the penetration velocity, jet flow, and the soil characteristics. While the monopile moves deeper into the ground, the fluidised area emerges on the left side of the monopile. The hydrodynamic model simulates the flow inside the fluidised area and predicts the pressures, flow velocities, and concentrations near the surface of the soil plug. Subsequently, the pressures are used for the seepage flow model to predict the groundwater flow and seepage flow underneath the pile tip. The information from the fluidisation model and the seepage model combined with the updated equation for the plug surface velocity are used to calculate the exact velocity at which this trench widens. This results into the fluidised volume which can be related to the optimal flow rate.

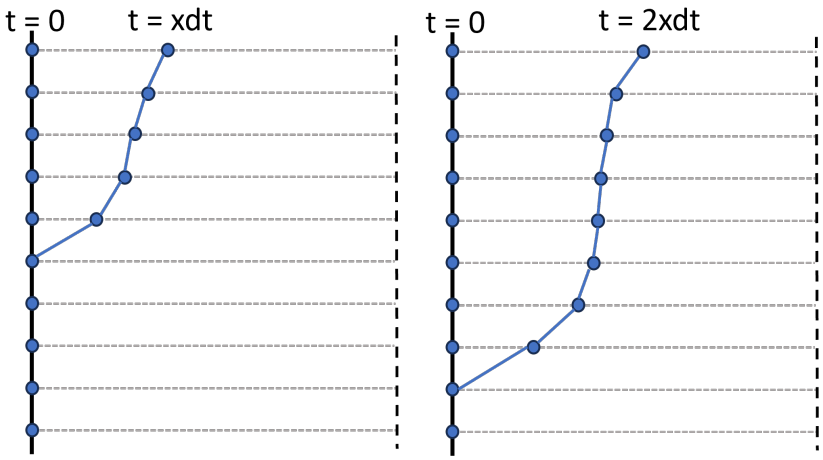

Figure 5.22: Representation of the erosion shape using layers and timestamps

6

Conclusion & recommendation on the optimisation of Vibrojet® performance

6.1. Advancements in understanding the plug surface shape formation

This research aims to optimise the Vibrojet® performance during offshore installation by reducing shaft friction as much as possible while having the least amount of jet flow. Thus the main research question:

- How to optimise the performance of the Vibrojet® during offshore installation?

To optimise the performance, an equation for estimating the plug surface displacement inside the monopile was selected and updated. The final goal is to predict the shape of the soil plug in collaboration with three other models.

A experimental setup was designed and constructed at Deltares to asses and update the plug surface velocity equation from previous studies. The test setup consisted of a soil container which allow testing of a soil layer of 2 meter width, 0.3 meter depth, and 1.5 meter height. 0.3 percent of the sand particles inside the container were covered with a UV layer to allow tracking of these particles with a camera. Visual software was written to estimate the plug surface shape and flow velocities over time. It was able to accurately estimate the trench width for most tests at the upper half of the soil plug.

This research found that the current equation for the estimation of the plug surface velocity significantly overestimates measured velocities observed in lab tests. Updates for the equation were suggested by using the results of the lab tests of the different installation settings: flow velocity, penetration velocity, relative density, and seepage. The discrepancies in the equation were found to be due to the differences in the testing environment. The following suggestions were made adapt the adapt the equation to the testing environment:

- Addition of a seepage force term to the equation.
- Introduction of a separate term for sedimentation effects.
- Inclusion of a factor for the return flow of particles.
- Consideration of the slope angle's influence on flow erosion.

Furthermore, all tests stabilised at a concentration of 40% in the middle of the fluidised zone, which revealed a relation between the flow rate and the trench width. This relationship suggests that the optimal flow rate for Vibrojet® installations can be determined by the total volume of sand that needs to be fluidised.

Alongside the equation for the plug surface velocity, three other models have been made parallel to this research. Together with the three other models, the equation can be used to calculate the optimal

soil plug shape during installation. This leads to the total volume of the fluidised zone. The optimal performance of the Vibrojet® can be calculated by using the relation between the flow rate and the volume of the fluidised zone.

The exploration into the effects of increased installation depths on the stability of soil plugs during offshore monopile installations highlights the significance of considering gravitational forces, soil plug height, and axial to radial stress ratios. The interplay of jet flow, seepage, and particle concentration introduces complex variables that can influence plug stability, acknowledging that scaling the relations found in this research should take into account the plug stability at greater depths.

6.2. Recommendation for further investigation of Vibrojet® installation

Based on knowledge that was gathered during this study, there are several recommendations which would lead to a better understanding of the plug surface shape formation.

- *The optimisation of the lab test setup:* The problems came up during the tests with the UV particles and camera were non-uniform brightness, reflections of surroundings, and influence of brightness. A recommendation would be to cover the whole installation in a black tent and to use one uniform UV light could be used to cover the soil container completely. This should improve the accuracy of the estimated variables and allow the calculation of concentration.
- *Update visual software:* By using the moving particles to estimate the plug surface shape it was unable to detect the underside of the trench, because the particles were moving too fast there. When the stationary particles are used, for most tests the full plug surface shape can be estimated. This allows for the calculation of the total fluidised area over time, which should give insight on the relation between the flow rate and the fluidised area. Also, the impact of energy loss when the jet is moving down could be related to the fluidised area.
- *More thorough testing:* Unfortunately, part of the tests were cut off to quickly, which impacted the results of the stable plug surface. When done correctly, definitive relations in flow rate, relative density, jet penetration velocity and seepage flow can be found. These relations can be used to update the current plug surface velocity equation accurately, allowing the combining with the jet erosion model and the hydrodynamic model. Subsequently, analysis of the tests with different sand particle sizes allows for the replication of North Sea soil conditions.
- *Increased depth testing:* The unknown factor for scaling up the installation depth of the monopile is the impact of the increasing height of the soil plug. There are several options to investigate this further:

    1. Performing very low flow tests may be a way to find out the consequence of plug instability.
    2. Executing pressurised tests at the Deltaris institute, thereby simulating the increased weight on the soil plug.
    3. Performing in the field tests with pressure sensors on the inside of the monopile to measure the timing and impact of the plug slope failing.

References

Akiyama, J., & Stefan, H. (1985). Turbidity current with erosion and deposition. *Journal of Hydraulic Engineering*, *111*(12), 1473–1496. https://doi.org/10.1061/(ASCE)0733-9429(1985)111:12(1473)

Alahmari, A., Jamal, A., & Elazhary, H. (2021). Comparative study of common density-based clustering algorithms, 1–6. https://doi.org/10.1109/NCCC49330.2021.9428832

Alhaddad, S., Labeur, R. J., & Uijttewaal, W. (2020). Breaching flow slides and the associated turbidity current. *Journal of Marine Science and Engineering*, *8*(2). https://doi.org/10.3390/jmse8020067

Alhaddad, S., Labeur, R., & Uijttewaal, W. (2021). Preliminary evaluation of existing breaching erosion models. In J. Rice, X. Liu, I. Sasanakul, M. McIlroy, & M. Xiao (Eds.), *Proceedings of the 10th international conference on scour and erosion (icse-10)* (pp. 619–627). International Society for Soil Mechanics; Geotechnical Engineering.

Bath, A. (2023, October). Global Offshore Wind Report 2023. https://gwec.net/gwecs-global-offshore-wind-report-2023/

Biryaltseva, T., Moerz, S. T. K., & Lunne, T. L. (2016). Relative density prediction based on in-situ and laboratory measurements of shear wave velocity. In
bibinitperiod K. Lehane Acosta-Martinez (Ed.). Australian Geomechanics Society.

Bisschop, F. (2018). Erosion of sand at high flow velocities. *Erosion of sand at high flow velocities : An experimental study*. https://doi.org/10.4233/uuid:1d6b0b9f-65e0-44d8-87d1-a21016c88653

Blankers, L. (2024, April). IQIP's latest and largest innovation in noise mitigation well on its way. https://iqip.com/iqips-latest-and-largest-innovation-in-noise-mitigation-well-on-its-way/

Brownlie, W. R. (1981). Prediction of flow depth and sediment discharge in open channels.

Brownlie, W. R. (1983). Flow depth in sand-bed channels. *Journal of Hydraulic Engineering*, *109*(7), 959–990. https://doi.org/10.1061/(ASCE)0733-9429(1983)109:7(959)

EC. (2023).

Eijkens, R. (2023, July). Pve giant 2000 upending vibro.

Einstein, H. A. (1950, September). *The Bed-Load Function for Sediment Transportation in Open Channel Flows* (Technical Bulletins No. 156389). United States Department of Agriculture, Economic Research Service. https://doi.org/10.22004/ag.econ.156389

Evolution of offshore wind resources in northern europe under climate change. (2023). *Energy*, *269*, 126655. https://doi.org/https://doi.org/10.1016/j.energy.2023.126655

Ferguson, R., & Church, M. (2004). A simple universal equation for grain settling velocity. *Journal of Sedimentary Research - J SEDIMENT RES*, *74*, 933–937. https://doi.org/10.1306/051204740933

GBMWorks. (2020). "gbm works internal information".

GWEC. (2023).

He, W., Hayatdavoudi, A., Chen, K., Sawant, K., Zhang, Q., & Zhang, C. (2019). Enhancement of Plastering Effect on Strengthening Wellbore by Optimizing Particle Size Distribution of Wellbore Strengthening Materials. *Journal of Energy Resources Technology*, *141*(12), 122905. https://doi.org/10.1115/1.4043785

Hill, D. (2022, July). Orion completes first project installing largest ever xxl monopiles. https://www.heavyliftnews.com/deme-offshores-orion-completes-first-project-installing-largest-ever-xxl-monopiles/

iea. (2023). Executive summary – World Energy Outlook 2023 – Analysis - IEA. https://www.iea.org/reports/world-energy-outlook-2023/executive-summary

Lotysh, V., Gumeniuk, L., & Humeniuk, P. (2023). Comparson of the effectiveness of time series analysis methods: Sma, wma, ema, ewma, and kalman filter for data analysis. *Informatyka, Automatyka, Pomiary w Gospodarce i Ochronie Środowiska*, *13*(3), 71–74. https://doi.org/10.35784/iapgos.3652

Mastbergen, D., & Berg, J. H. (2003). Breaching in fine sands and the generation of sustained turbidity currents in submarine canyons. *Sedimentology*, *50*. https://doi.org/10.1046/j.1365-3091.2003.00554.x

McGurk, K., Owen, B., Watson, W., Nethononda, R., Cordell, H., Farrall, M., Rider, O., Watkins, H., Revell, A., & Keavney, B. (2020). Heritability of haemodynamics in the ascending aorta. *Scientific Reports*, *2020*, 14356. https://doi.org/10.1038/s41598-020-71354-7

Mehmet Bilgili, H. A., & Ilhan, A. (2023). Potential visibility, growth, and technological innovation in offshore wind turbines installed in europe. *Environmental Science and Pollution Research*. https://doi.org/10.1007/s11356-022-24142-x

Niven, R. K., & Khalili, N. (1998). In situ fluidisation by a single internal vertical jet. *Journal of Hydraulic Research*, *36*(2), 199–228. https://doi.org/10.1080/00221689809498633

Noordzeeloket. (2023). Kader ecologie en cumulatie.

O'Sullivan, R. (2024, January). The eu built a record 17 gw of new wind energy in 2023 - wind now 19% of electricity production. https://windeurope.org/newsroom/press-releases/the-eu-built-a-record-17-gw-of-new-wind-energy-in-2023-wind-now-19-percent-of-electricity-production/

Parker, G., Fukushima, Y., & Pantin, H. M. (1986). Self-accelerating turbidity currents. *Journal of Fluid Mechanics*, *171*, 145–181. https://doi.org/10.1017/S0022112086001404

Reuters. (2024, March). Eneco drops out of tender for massive dutch offshore wind farm. https://www.reuters.com/business/energy/eneco-drops-out-tender-massive-dutch-offshore-wind-farm-2024-03-28/

Richardson, J., & Zaki, W. (1954). The sedimentation of a suspension of uniform spheres under conditions of viscous flow. *Chemical Engineering Science*, *3*(2), 65–73. https://doi.org/https://doi.org/10.1016/0009-2509(54)85015-9

Roberts, J., Jepsen, R., Gotthard, D., & Lick, W. (1998). Effects of particle size and bulk density on erosion of quartz particles. *Journal of Hydraulic Engineering*, *124*(12), 1261. https://doi.org/10.1061/(ASCE)0733-9429(1998)124:12(1261)

Rott, N. (1990). Note on the history of the reynolds number. *Annual review of fluid mechanics*, *22*(1), 1–12.

Rowe, P. (1987). A convenient empirical equation for estimation of the richardson-zaki exponent. *Chemical Engineering Science*, *42*(11), 2795–2796. https://doi.org/https://doi.org/10.1016/0009-2509(87)87035-5

Shields, A. (1936). Anwendung der ähnlichkeitsmechanik und der turbulenzforschung auf die geschiebebewegung.

Terzaghi, K. (1943). *Theoretical soil mechanics*. John Wiley; Sons, INC.

van Rhee, C., & Bezuijen, A. (1992). Influence of seepage on stability of sandy slope. *Journal of Geotechnical Engineering*, *118*(8), 1236–1240. https://doi.org/10.1061/(ASCE)0733-9410(1992)118:8(1236)

van Rhee, C. (2010). Sediment entrainment at high flow velocity. *Journal of Hydraulic Engineering*, *136*(9), 572–582. https://doi.org/10.1061/(ASCE)HY.1943-7900.0000214

van Rhee, C. (2015). Slope failure by unstable breaching. *Proceedings of the 21st World Dredging Congress & Exhibition 2016 WODCON XXI*, *1*, 716–729.

van Rhee, C., & Talmon, A. (2010). Sedimentation and erosion of sediment at high solids concentration.

van Rijn, L. C. (1984). Sediment pick-up functions. *Journal of Hydraulic Engineering*, *110*(10), 1494–1502. https://doi.org/10.1061/(ASCE)0733-9429(1984)110:10(1494)

van Rijn, L. C. (1986). Applications of sediment pick-up function. *Journal of Hydraulic Engineering*, *112*(9), 867–874. https://doi.org/10.1061/(ASCE)0733-9429(1986)112:9(867)

Vázquez, A., Izquierdo, U., Enevoldsen, P., Andersen, F.-H., & Blanco, J. M. (2022). A macroscale optimal substructure selection for europe's offshore wind farms. *Sustainable Energy Technologies and Assessments*, *53*, 102768. https://doi.org/https://doi.org/10.1016/j.seta.2022.102768

Winterwerp, J. C., Bakker, W. T., Mastbergen, D. R., & van Rossum, H. (1992). Hyperconcentrated sand water mixture flows over erodible bed. *Journal of Hydraulic Engineering*, *118*(11), 1508–1525. https://doi.org/10.1061/(ASCE)0733-9429(1992)118:11(1508)

Zhang, J., Shen, K., Wang, B., Wen, G., & Li, S. (2023). Study of a method for drivability of monopile in complex stratified soil. *Journal of Marine Science and Engineering*, *11*(3). https://www.mdpi.com/2077-1312/11/3/603

A

Appendix

A.1. Literature

Shields parameter restrictions

Restrictions on Input Data

Parameter	Symbol	Restriction	Reason
Median grain size, mm	D_{50}	$0.062 \leq D_{50} \leq 2.0$	Sand only
Geometric standard deviation of bed particles	σ_g	$\sigma_g < 5$	Eliminate bimodal distributions
Width to depth ratio	w/d	$w/d > 4$ $\left(\begin{smallmatrix}\text{Lab}\\ \text{Data}\end{smallmatrix}\right)$	Reduce sidewall effects
Relative roughness	r/D_{50}	$r/D_{50} > 100$	Eliminate shallow water effects
Concentration, ppm	C	C>10	Accuracy problems associated with low concentration

Figure A.1: Shields parameter restrictions by Brownlie, 1981 (table 4)

Derivation of erosion formula by Mastbergen and Berg, 2003

Mastbergen and Berg, 2003 start with a general formula for the pick-up function:

$$\Phi = A\,(\theta - \theta_{cr})^m\, D_*^n \tag{A.1}$$

The influence of breaching was added to the formula by the multiplication of the pick-up function by a function with the slope angle and the internal friction angle of the soil.

$$\Phi \left\{ 1 - \frac{\tan(\beta)}{\tan(\phi)} \right\} = c_a\,(\theta - \theta_{cr})^m\, D_*^n \tag{A.2}$$

Multiplication of the pick-up function with the relative erosion velocity factor, this accounts for the effect of a reduced erosion due to the negative pore pressures that are created.

$$\Phi(\frac{\sin(\phi - \alpha)}{\sin(\phi)})(1 - \frac{v_p}{v_{wal}}) = c_a(\theta - \theta_{cr})D_*^m \tag{A.3}$$

The pick-up function gets replaced by the erosion velocity using the following equation:

$$v_p = \frac{E}{\rho_s(1-n_0)} = \frac{\Phi}{1-n_d} u_s \cos\alpha \tag{A.4}$$

$$\frac{v_p}{u_s}\left(1-\frac{v_p}{v_{wall}}\right) = \frac{c_a(\theta-\theta_{cr})D_*^m}{(1-n_0)\frac{\sin(\phi-\alpha)}{\sin(\phi)}} \tag{A.5}$$

$$v_p\left(1-\frac{v_p}{v_{wall}}\right) = \frac{A(\theta-\theta_{cr})D_*^m}{(1-n_0)\frac{\sin(\phi-\alpha)}{\sin(\phi)}} u_s \tag{A.6}$$

This finally yields the formula used in the sensitivity analysis with the wall velocity calculate by van Rhee, 2010. The ABC-method was needed to express v_p in u_s and v_{wall}. After elusive testing the factors were empirically determined were c_a = 0.018, m = 1.5, and n = 0.3.

$$v_{wall} = \frac{\sin(\phi-\beta)}{\sin\phi}\frac{\Delta\rho(1-n_0)k_l}{\delta n} \tag{A.7}$$

$$v_p = u_s\left(\frac{v_{wall}}{2u_s} + \sqrt{\left(\frac{v_{wall}}{2u_s}\right)^2 + 0.018\,(\theta-\theta_{cr})^{1.5} D_*^{0.3}\frac{\Delta\rho k_l}{\delta n u_s}}\right) \tag{A.8}$$

Large scale experiments Alhaddad et al., 2020

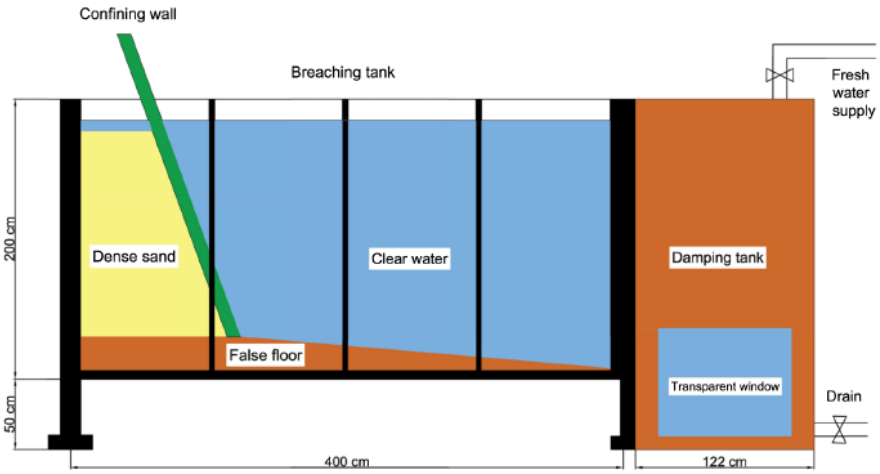

Figure A.2: Side view of the experimental setup illustrating the components; the sedimentation tank is not shown in the figure. The confining wall gets removed and the degradation speed of the dense sand was measured.

A.2. Methodology

Sensor locations

Figure A.3 shows the locations of the sensors that are installed in the tank. The type of sensor and the colours are given below.

- Pore pressure sensors 13x - blue
- Total pressure sensors 4x - yellow
- Absolute pressure sensor - purple
- Temperature sensor - red

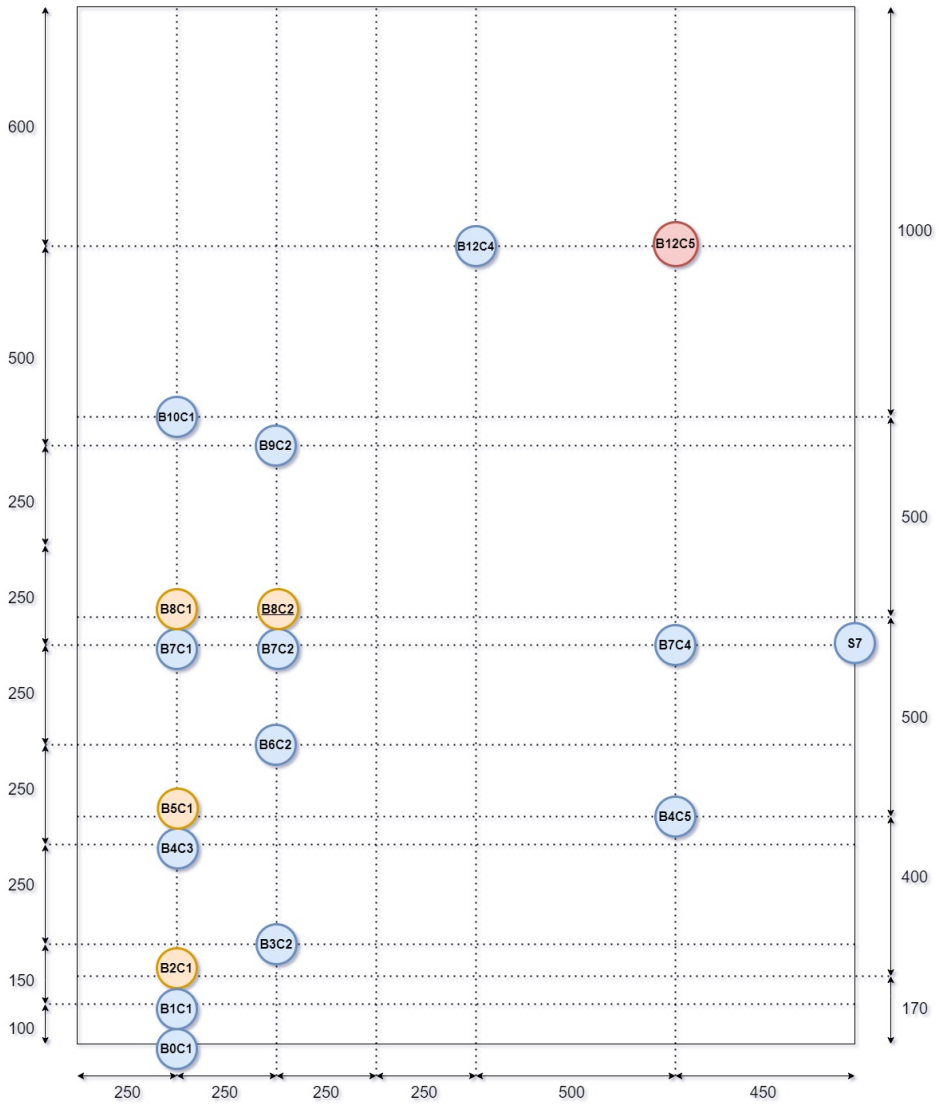

Figure A.3: Locations of working sensors in the tank

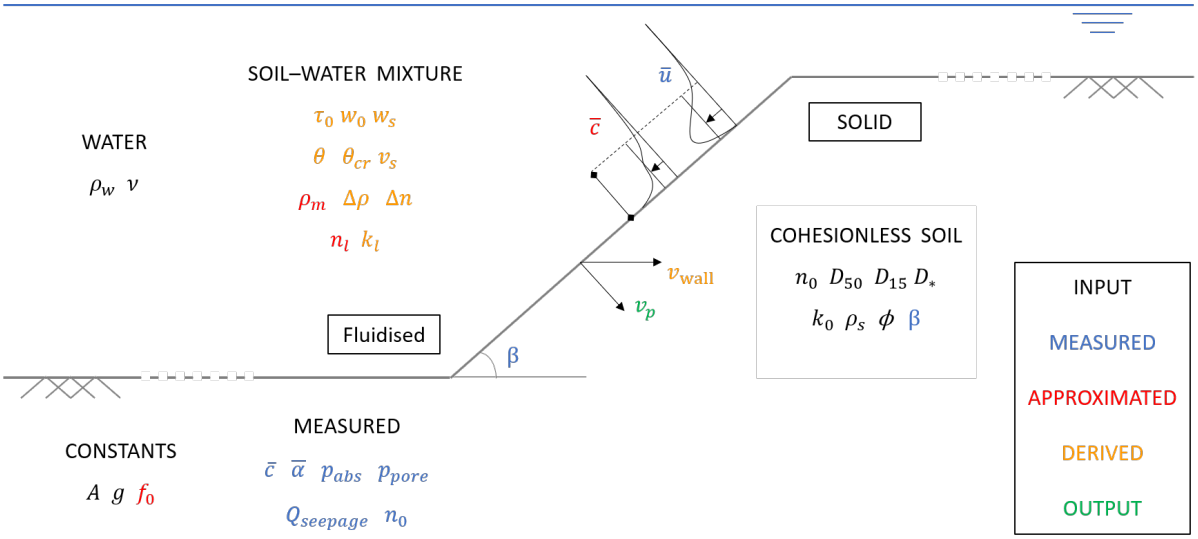

Figure A.4: Schematic of front of the tank

EMA smoothing of PWP sensors

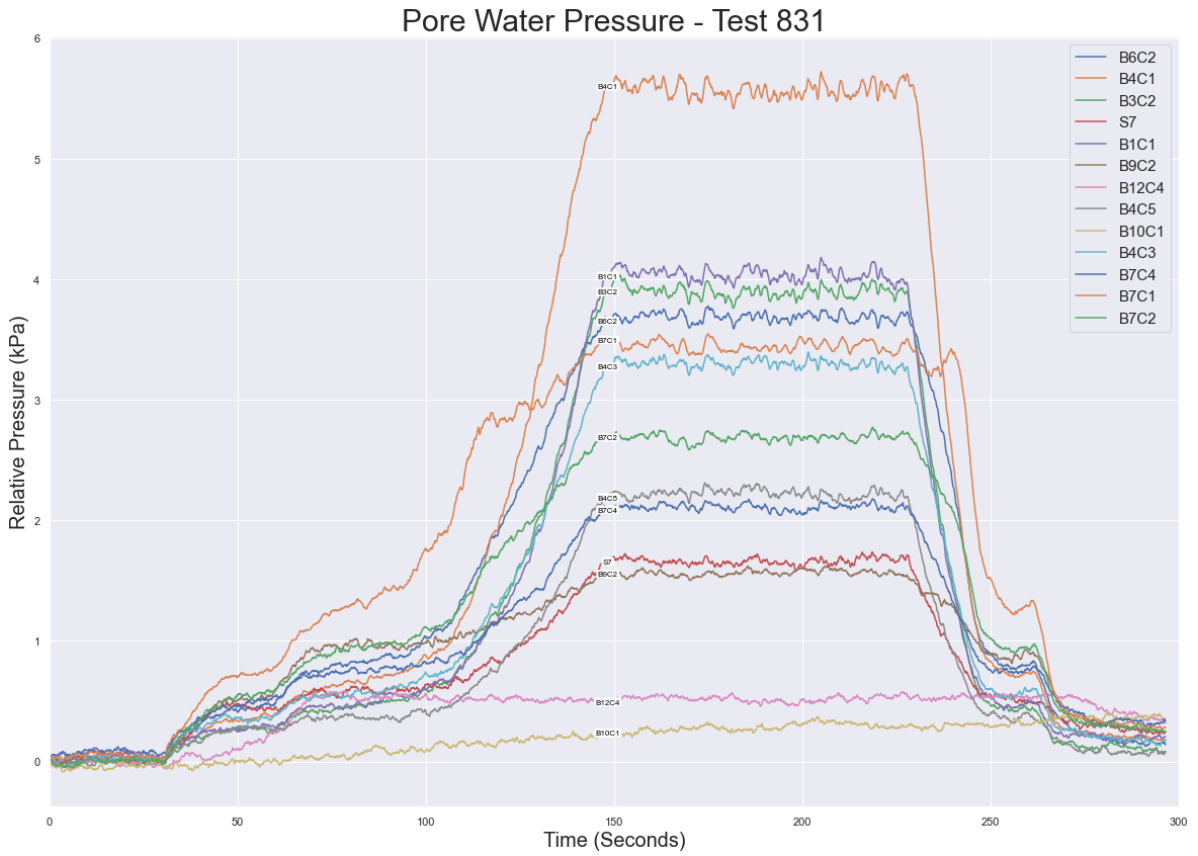

Figure A.5: PWP sensors alongside jet position after EMA applied with span set to 10 (test 831)

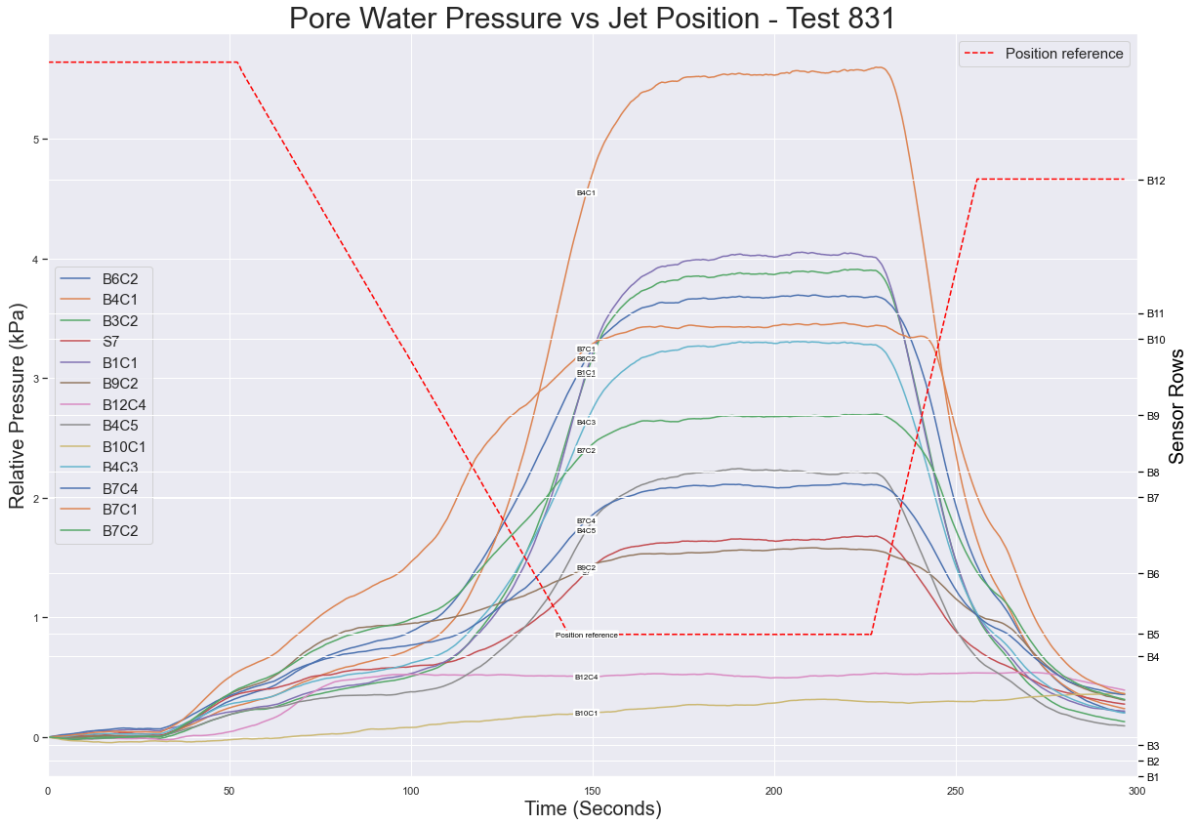

Figure A.6: PWP sensors alongside jet position after EMA applied with span set to 100 (test 831)

Temperature validation

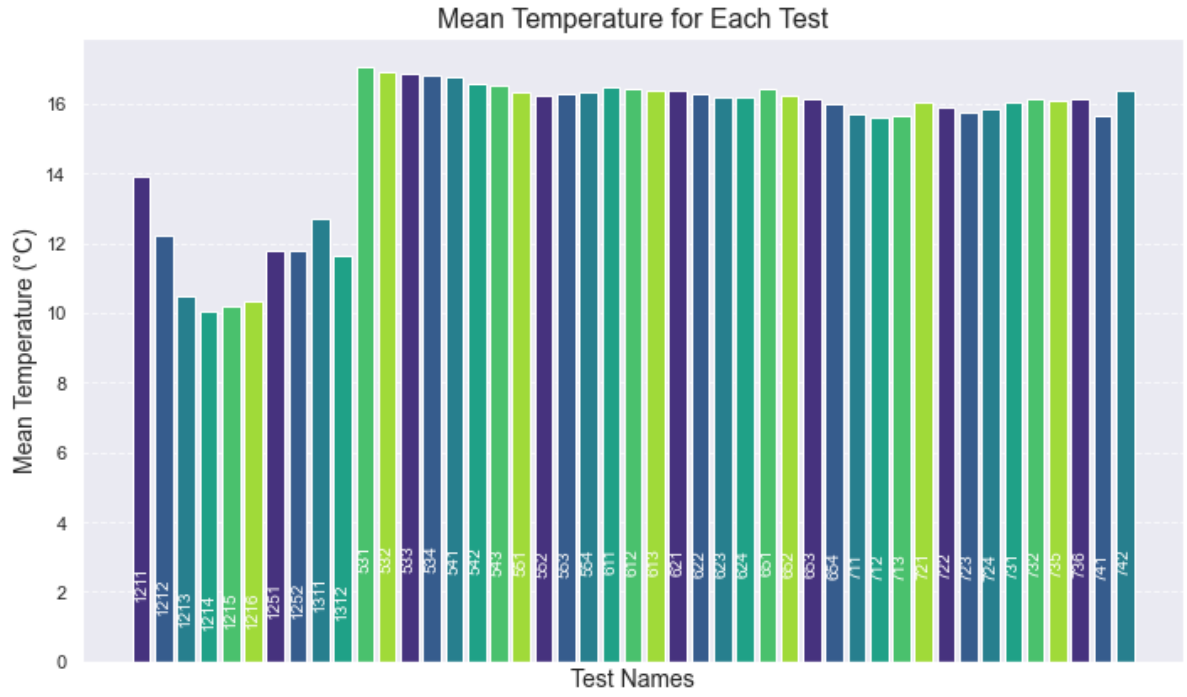

Figure A.7: Water temperature in soil container during testing sequence

Visual software

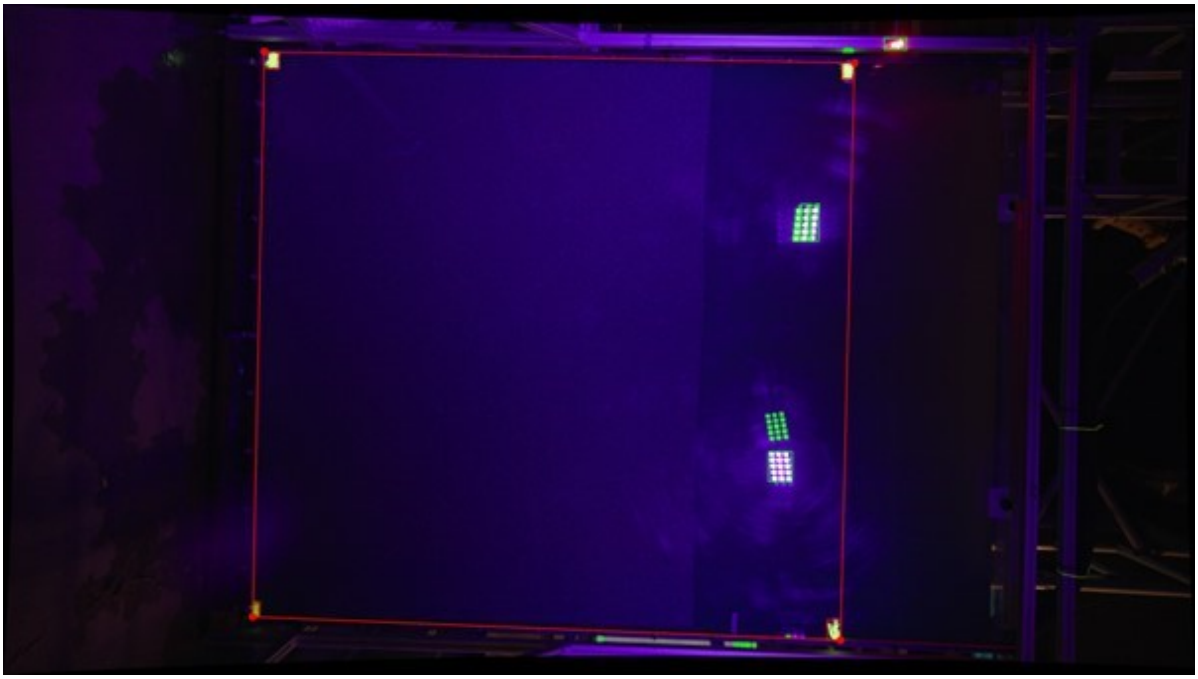

Figure A.8: System for finding the markers on the soil container, which was repeated every test

Density soil given by external party

Density solids

Sample	Density [Mg/m^3]
M31	2.650
S90	2.662
DS0.2-1	2.659
UVsand	2.619

Min/Max density normal sand

Sample	Min density [Mg/m^3]	Max density [Mg/m^3]
M31	1.508	1.776
S90	1.379	1.619
DS0.2-1	1.532	1.759

Min/Max density UV sand

Sample	Min density [Mg/m^3]	Max density [Mg/m^3]
M31	1.522	1.739
S90	1.381	1.578
DS0.2-1	1.558	1.748

Figure A.9: Minimum and maximum relative density of the dry soil

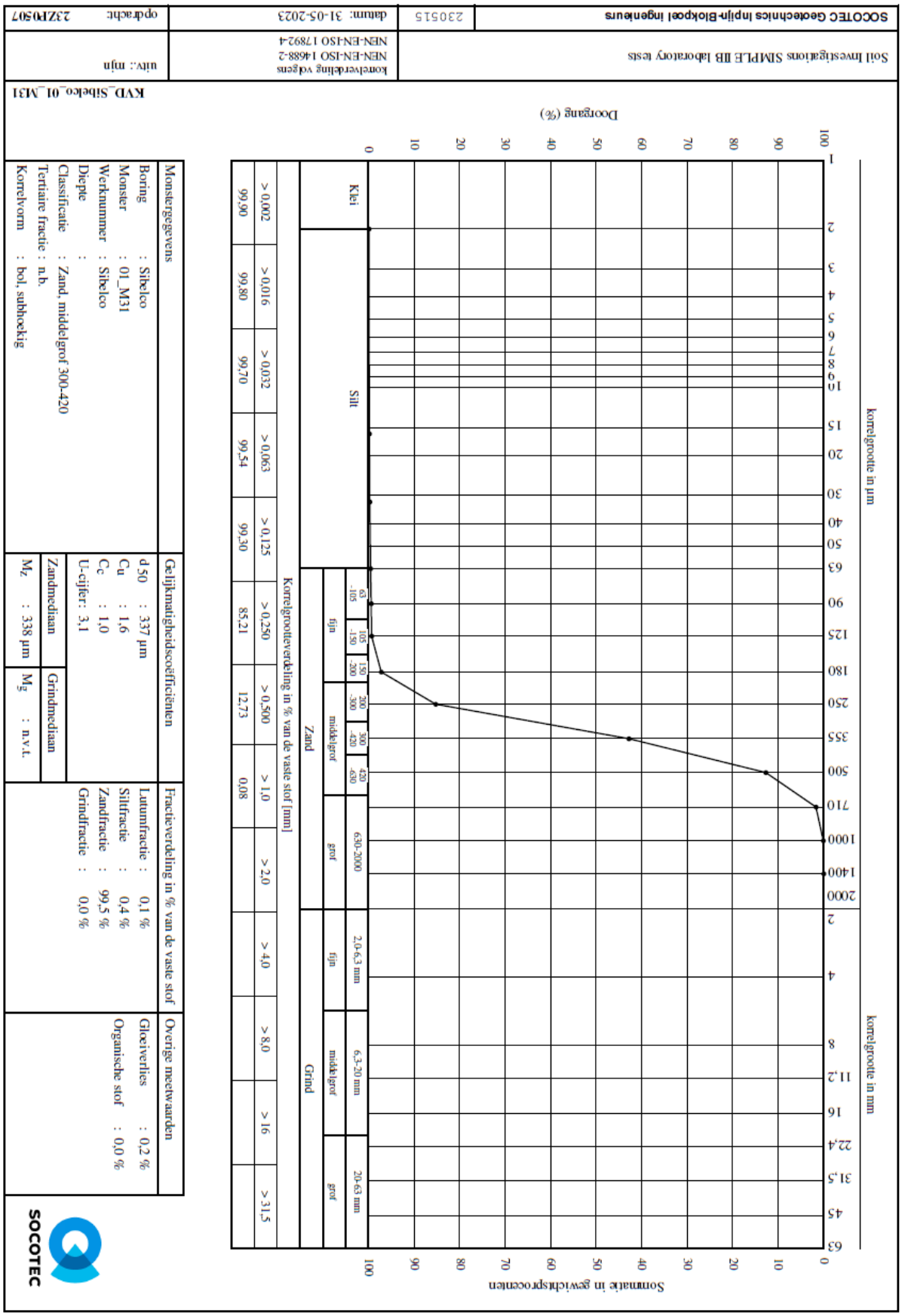

Figure A.10: Particle density spectrum of medium sand size

A.3. Results & discussion

Test ID	Second	Height	Flow rate	RD	Jet velocity	Seepage	Final trench width	Final β	β at plug velocity	Perp velocity	Real plug velocity	Calculated plug velocity
532	275	650	80	50	10	2500	300	70	70	0.67	0.63	12.90
532	275	850	80	50	10	2500	200	75	73	1.00	0.96	13.83
533	280	650	100	50	10	2500	350	67	67	0.00	0.00	11.93
533	280	850	100	50	10	2500	275	67	67	0.00	0.00	11.93
534	300	650	120	50	10	2500	450	65	65	0.00	0.00	11.27
534	300	850	120	50	10	2500	380	70	70	0.20	0.18	14.13
623	300	650	120	75	10	2500	450	75	75	0.30	0.29	10.03
623	300	850	120	75	10	2500	400	70	67	0.50	0.46	8.30
653	200	650	80	50	10	1490	210	63	63	0.00	0.00	10.59
653	200	850	80	50	10	1490	150	80	80	0.00	0.00	15.84
654	220	650	80	50	10	0	220	40	40	0.00	0.00	2.11
654	220	850	80	50	10	0	100	85	90	0.00	0.00	18.31
732	250	650	120	100	40	2500	580	77	70	1.80	1.69	7.00
732	250	850	120	100	40	2500	480	60	75	2.00	1.93	7.83
735	160	650	120	75	40	2500	500	70	68	1.25	1.16	8.52
735	160	850	120	75	40	2500	400	60	75	1.65	1.59	10.30
736	175	650	100	75	40	2500	400	70	80	1.50	1.48	11.02
736	175	850	100	75	40	2500	350	75	89	2.00	2.00	12.58
1211	150	650	120	75	20	2500	400	95	85	1.30	1.30	11.92
1211	150	850	120	75	20	2500	400	78	83	1.60	1.59	11.57

Figure A.11: Results lab tests. Including slope angels, plug surface velocity and the calculated plug surface velocity